Collinear Laser Spectroscopy of Manganese Isotopes using the Radio Frequency Quadrupole Cooler and Buncher at ISOLDE

Thesis submitted in accordance with the requirements of the University of Liverpool

for the degree of

Doctor of Philosophy

by

Carla Babcock

October, 2015

Abstract

The hyperfine structure of the odd-even $^{51-63}$Mn isotopes ($N = 26 - 38$) were measured using bunched beam collinear laser spectroscopy with the COLLAPS experimental setup at ISOLDE, CERN. The properties of these nuclei were investigated over the course of two experiments. During the first experiment, nuclear spins and magnetic dipole moments were extacted from spectroscopy on manganese atoms. These nuclear properties were then compared to the predictions of two large-scale shell model effective interactions (GXPF1A [1, 2] and LNPS [3]) which use different model spaces. In the case of ^{61,63}Mn, these results show the increasing importance of neutron excitations across the proposed $N = 40$ subshell closure, and of proton excitations across the $Z = 28$ shell gap. These measurements provide the first direct proof that proton and neutron excitations across shell gaps are playing an important role in the ground state wave functions of the neutron-rich Mn isotopes.

The electric quadrupole moment provides complementary information to the magnetic dipole moment, since it is able to directly probe the degree of collectivity and deformation in a nucleus, however sensitivity limitations during the first experiment prevented the quadrupole moments from being accurately determined. To overcome these limitations, it was necessary to find an electronic transition with sensitivity to the quadrupole interaction. A suitable transition was found in the ion from a metastable state and optical pumping in ISOLDE's cooler and buncher, ISCOOL, was used to populate this state for the second manganese experiment. This is the first use of the in-cooler optical pumping technique at ISOLDE, and required an overhaul of ISCOOL.

During the second experiment, the spectroscopic quadrupole moments of the isotopes were extracted from the measured hyperfine spectra of manganese ions. The sensitivity and spectroscopic efficiency were increased as compared to the atomic experiment. The extracted quadrupole moments were again compared to predictions from the GXPF1A and LNPS effective interactions. The inclusion of the $1\,\nu g_{9/2}$ and $2\,\nu d_{5/2}$ orbitals in the model space were shown to be necessary to reproduce the experimentally observed onset of quadrupole deformation.

Acknowledgments

I would like to thank my PhD supervisor, Bradley Cheal, for all his encouragement and patience with me over the past years, and for all the sound advice he has given me during this time. I am very grateful to have found such a conscientious person to guide me through this.

I would also like to thank my CERN supervisor, Tim Giles, for giving me the freedom to make mistakes, and the support to fix them afterwards. I have always appreciated his confidence in me and his championship of my interests in difficult situations.

Gratitude is also due to the members of COLLAPS, without whom there would have been no experiments, and to the ISOLDE Technical Group, without whom there would be no ISOLDE.

Many thanks to Hanne and Gerda for so many fruitful conversations and so much guidance. And of course, many thanks to my parents for being *the best*.

Contents

List of Tables

List of Figures

Chapter 1

Introduction

The appearance and disappearance of magic numbers [4] across the nuclear landscape has provided a challenge to nuclear models, which must be prepared to account for the sometimes rapidly changing nature of nuclear structure, especially as experimentalists investigate ever more exotic isotopes. The comparison of observables predicted by nuclear models to experimental data is a powerful tool to understand nuclear structure evolution and improve its description within the shell model. The ingredients necessary to make model predictions match experimental results informs us on a fundamental level about the role of different forces in different nuclei. In this work, the technique of collinear laser spectroscopy has been applied to manganese isotopes in order to extract nuclear parameters from the hyperfine spectra, which are a result of the interplay between the nucleus and the magnetic and electric fields generated by the electrons. The hyperfine spectrum allows the magnetic dipole moment and electric quadrupole moment of a nucleus to be derived, as well as a model-independent determination of the nuclear spin [5, 6]. The electromagnetic moments are useful indicators of ground state properties such as wave function composition, collectivity

and deformation. Here, the spins and moments of the odd-even isotopes in the range $^{51-63}$Mn will be reported and their interpretation within the framework of the shell model will be discussed.

1.1 Motivation for this work

Neutron-rich manganese isotopes ($Z = 25$) provide an opportunity for studying shell structure evolution towards the suspected subshell closure at $N = 40$ [7, 8]. This appears as a possible subshell closure for ^{68}Ni, observed through a low quadrupole transition probability ($0_1^+ \rightarrow 2_1^+$) and a high lying 2_1^+ state [9], however mass measurements of neutron-rich Ni indicate that the closure is weak [10]. Furthermore, both the $B(E2)$ transition rate and high lying 2_1^+ state can be explained by the parity change across the $N = 40$ gap [11, 12]. For elements above $Z = 28$, such as Cu and Ga, no magicity is suggested for $N = 40$ from mass measurements [13]. Though the measured nuclear moments of Cu could be interpreted as having a shell gap at $N = 40$, the parity change between the pf and g orbitals could also explain this behaviour [14]. In Ga isotopes, strong shape changes have been observed from $N = 40$ to $N = 50$ [15]. For elements with $Z < 28$, an increase in collectivity and deformation measured for Fe and Cr [16, 17], as well as a lack of significant discontinuities in the 2-neutron separation energies for Fe [18] and Mn [19] also imply that $N = 40$ is a very weak subshell gap, which decreases quickly as protons are removed from the $1f_{7/2}$ shell.

Theory suggests that the weakening of the $N = 40$ subshell gap results from the reduction of the proton-neutron interaction as protons are removed from the $1f_{7/2}$ orbital [20, 17]. This can be explained by the tensor force acting between nucleons in different orbitals, which modifies the effective single particle energies.

In this case, we consider the monopole part of the tensor force between proton and neutron orbitals, since we are interested in the changing energies of the neutron orbitals for different proton numbers. Since the tensor potential for the nucleon-nucleon interaction is thought to be the result of meson exchange, it depends on the relative momentum between the particles, and on their relative position with respect to their spin orientation [20]. In the case where we have one nucleon with $j = \ell + 1/2$ and another with $j' = \ell' - 1/2$, these two nucleons have high relative momentum and this results in the spatial overlap of their wavefunction being spread in the direction of their spins, and not in the direction of their orbital motion. This mimicks the situation found in the deuteron, and thus implies that the interaction of these two orbitals will result in increased binding energy. The case of two nucleons both having $j = \ell + 1/2$ and $j' = \ell' + 1/2$ (similarly for the case of two nucleons both having $j = \ell - 1/2$) presents the opposite situation, and the state will be less bound as a result of the nucleon-nucleon interaction [20, 21]. This qualitative explanation allows us to interpret the reduced binding of the $\nu 1f_{5/2}$ level, and the increased binding of the $\nu 1g_{9/2}$ and $\nu 2d_{5/2}$ levels, as the results of the removal of protons from the $\pi 1f_{7/2}$ when going from Ni to Mn. The changes to the single particle energy levels of these orbitals thus result in a reduction of the $N = 40$ gap [20, 17]. This is supported by the results of deep-inelastic reaction studies which show that the excited states in heavier odd Mn isotopes occur at energies similar to those of the intruder $\nu 1g_{9/2}$ isomers in the even Fe isotones [22].

As a result of the weakened subshell gap, quadrupole correlations are enhanced by the excitation of neutrons from the $2p_{1/2}$ and $1f_{5/2}$ orbitals into the $1g_{9/2}$ and $2d_{5/2}$ orbitals, making collectivity energetically favourable in the pf shell nuclei in which the

orbitals past $N = 40$ are occupied [7]. The promotion of neutrons to the $g_{9/2}$ orbital has been proposed as a driver of deformation [23], the evidence for which comes from the low-lying positive parity bands in $^{59}Fe_{33}$ [24], and $^{55,57,59}Cr_{31,33,35}$ [25, 26] which have a rotational nature and are known to involve excitations to $\nu g_{9/2}$. Similarly, the role of the $\nu d_{5/2}$ orbital in quadrupole collectivity for nuclei in which both proton and neutron excitations are involved cannot be underestimated [27]. For instance, the inclusion of this orbital is found to be necessary to reproduce the low-lying 2_1^+ state in ^{62}Cr [16]. The development of quadrupole collectivity also favours the excitation of protons across the $Z = 28$ gap and the position of these isotopes in the mid-pf shell means that these proton excitations play a role in determining structure, since the p-n interactions are more pronounced when protons and neutrons occupy the same major shell. This highlights the fact that the development of collectivity is correlated not only to the excitation of neutrons past the $N = 40$ subshell gap, but to the dimensions of the total proton-neutron valence space of a particular isotope, and so isotopes with similar valence spaces are found to follow similar trends in collectivity [28].

The electromagnetic transition probabilities, decay chains and level structures for the neighbouring isotopic chains of Cr and Fe have been studied in several works and evidence has been found for deformation in their neutron-rich isotopes. In Fe, the onset of collectivity is found between ^{62,64}Fe [7] and this collectivity persists in more neutron-rich isotopes, as demonstrated by $B(E2)$ values [28] and the decreased energy of the 2_1^+ state in ^{66}Fe [29]. From the measured $B(E2)$ values, a deformation parameter of $\beta \approx 0.28$ is found for ^{64,66}Fe [28]. ^{67}Fe also shows evidence of deformation extending past $N = 40$ [30].

In Cr, the isotopes between ^{56}Cr and ^{60}Cr begin to show an enhancement in collectivity, demonstrated by an energy level structure characteristic of the transition from vibrational excitation to rotational collectivity [31]. In ^{62}Cr, the $E(4^+)/E(2^+)$ ratio suggests a more rotational character, providing evidence for static prolate deformation in the heavier isotopes [31], and a deformation parameter of $\beta \approx 0.35$ has been reported [7]. More recently however, theoretical calculations have suggested that the low-lying states of neutron-rich Cr cannot in fact be characterized as strictly prolate rigid-rotor and are actually dominated by large amplitude shape fluctuations [32]. The enhacement in collectivity observed for Cr isotopes near $N = 40$, as for Fe isotopes in the same region, has been attributed to the occupation of the $\nu g_{9/2}$ and $\nu d_{5/2}$ orbitals and to the strong p-n correlations for nuclei in this region [3]. The observations of Fe and Cr suggest that we may expect to see a similar increase in collectivity in the Mn isotopes towards $N = 40$.

There have been theoretical attempts to describe this region of the nuclear chart using a variety of effective shell-model interactions, one of the most used being the GXPF1A interaction, which models the full pf space [1, 2]. This interaction has been very successful in describing nuclei with particles in the mid-pf shell, however for isotopes approaching $N = 40$, the exclusion of the $\nu 1g_{9/2}$ orbital from the model space limits its effectiveness [33, 8]. The model space has therefore been extended to the $pfg_{9/2}$ orbitals and the isotopes $^{57-63}$Mn have been investigated with various interactions [34, 8]. Good agreement with published excitation energy data has been found for most of the isotopes, but information on the electromagnetic properties is required to fully test the interactions. In order to reproduce the observed quadrupole collectivity, it has been argued that it is also necessary to take into account the

$\nu 2d_{5/2}$ level [3]. This has been incorporated into the LNPS interaction [3], using a ^{48}Ca core and allowing excitations to $\nu 1g_{9/2}$ and $\nu 2d_{5/2}$. It greatly expands the computational domain as compared to the previously discussed models, and has been used successfully to describe energies and transition probabilities in the elements Fe [7, 28], Cr [17, 35], Co [36] and Cu [37].

This work will cover a theoretical developement of the relevant background material (Ch. 2), an overview of the ISOLDE facility (Ch. 3), the first experiment performed on atomic manganese, which yielded the spins and magnetic moments of the isotopes of interest (Ch. 4), the improvements to the radio frequency quadrupole cooler and buncher to allow for in-cooler optical pumping, plus the proof-of-concept at ISOLDE (Ch. 5), the subsequent experiment using optical pumping on manganese ions, which yielded the quadrupole moments (Ch. 6), a summary of the physics results (Ch. 7) and finally a summary of possible future work on these topics (Ch. 8).

Chapter 2

Theoretical Background

In order to probe the limits of the standard model and the dynamics of interactions within the nucleus, a concurrence of nuclear theory and nuclear experiments is necessary. The interplay between theory and experiment allows the refinement of proposed nuclear interactions, improving our understanding of nuclear phenomena. The shell model [38], one among several descriptions of the nucleus, has been very successful in offering accurate predictions of many nuclear observables. Nucleons are assumed to fill successive shells, the energies of which are determined in a first approximation by a central potential [39]. More accurate descriptions are achieved by including more complex forces, for instance the spin-orbit coupling [40, 41], which splits each level associated with a particular value of the orbital angular momentum (ℓ) into two levels based on the projection of the spin. In this formulation, the properties of nuclei can theoretically be determined by single particle effects, however it quickly becomes obvious that this approach is complicated and neglects the important effects of interactions among the nucleons. A solution to this problem is to use a core-valence particle model [42, 43]. The core can be taken as a spherical, self-contained object

for which there are minimal interactions with the valence particles and no excitations. Usually a doubly-magic nucleus is chosen for this. The valence particles are the remaining nucleons outside this core, for which nucleon-nucleon interactions are considered and excitations are allowed, up to a certain point (the model space must be truncated at some point for practical reasons). An interaction between the core and the valence particles can also be included [44, 45]. The number of particles considered as valence depends on the nucleus under consideration and the balance between accuracy desired and computational power available. If we acknowledge the evidence (for instance the odd-even staggering in binding energies [46]) that nucleons tend to pair up with one another through a pairing interaction, then we can assume that all protons and neutrons in a nucleus should form spin zero pairs. Thus the properties of the nucleus can determined by the last unpaired nucleon; this is the extreme single particle model. This approach provides a good basis from which to begin, however the complexity of the interactions among nucleons means that it cannot be relied on to predict observables for nuclei other than those with a single nucleon outside a magic core. Often we must consider an ensemble of nucleons outside a spherical, well-bound core, which must be chosen carefully for each nucleus such that it does not limit any excitations which are necessary to reproduce experimental observables. This is the basis on which the properties of nuclei and the theoretical interactions used to model our observables will be described in the following sections [47, 48].

2.1 Properties of Nuclei

There are an abundance of nuclear properties that can be measured for any specific nucleus, such as mass, radius, decay modes, spin, half life, and electromagnetic moments. All properties contribute to our knowledge of nuclear structure and dynamics, and to our formulation of a coherent theory to describe basic interactions. The experiments described in this work were designed to measure the spins and electromagnetic moments of nuclei because these nuclear properties provide information about such wide-ranging topics as the wave functions, single particle properties and collectivity.

2.1.1 Spins

The spin of a particle is defined as its intrinsic angular momentum [49] and can be treated with the same formalism as orbital angular momentum. For fermions, spin = 1/2, and the total angular momentum of a nucleon is its orbital angular momentum plus its intrinsic (spin) angular momentum [48],

$$\boldsymbol{j} = \boldsymbol{\ell} + \boldsymbol{s}. \tag{2.1}$$

Observable properties of a nucleus can be explained by treating it as a single entity with total angular momentum I. This is the nuclear spin, which can be written as the sum of the total angular momenta of all the A nucleons in a nucleus. For medium or large nuclei, the angular momentum coupling to produce I is too complicated to be practical, but we can use the shell model to simplify the situation. As a first approximation, the extreme single particle model mentioned above can be used to determine the spin. Then we can say that the spin of an odd-A nucleus will be equal to the total angular momentum of the last unpaired nucleon. However, it will be

shown in Ch. 4 that this picture is only rudimentary and cannot account for the spins of all the manganese nuclei studied here. Taking the more realistic approach and considering a set of valence nucleons, the angular momentum contributions can be split into the particle contribution and the core contribution. In either case, we can say that odd-A nuclei will have half-integral nuclear spins and even-A nuclei will have integral nuclear spins [48].

2.1.2 Moments

Measurements of electromagnetic moments are important components in our understanding of nuclear structure and directly observable using the techniques of collinear laser spectroscopy [6], described in Ch. 3. The electric moments result from the distribution of charge in the nucleus and thus tell us something about the shape of the nucleus. The magnetic moments result from the movement of charge inside the nucleus and thus tell us something about the structure of the nucleus via angular momentum considerations. The mathematical form of the moments can be derived by using a multipole expansion to describe the electric and magnetic fields around a nucleus. Each term in the expansion will have a different r dependence, and each term will be the mathematical form of a moment. We take only the first term in each expansion because higher order terms are not significant enough to be observable at our levels of accuracy [50].

For the magnetic moments, which arise from the movement of charges in the nuclear potential, the first term in the expansion of the field is the dipole $1/r^3$ term. The monopole term ($1/r$ in the potential expansion, $1/r^2$ in the field expansion) disappears because the line integral around a current loop is zero. For the electric

moments arising from the distribution of charge in the nucleus, the first term is the quadrupole $1/r^3$ term. Whether or not a multipole moment will be measurable in an isotope depends on the parity of the moment's operator and the two states involved in the transition, because of parity conservation. The expectation value of an operator O can be written as,

$$\langle O \rangle = \langle \psi \,|\, O \,|\, \psi \rangle \tag{2.2}$$

where ψ is the wavefunction. Thus, the parity of the state ψ is irrelevant because it cancels out, and the parity of the operator O is all that matters. If O is an odd function, its expectation value from $-\infty$ to $+\infty$ will vanish. The parity rules for the electromagnetic moment operators are [51],

$$\text{Electric Parity} = (-1)^L \tag{2.3}$$

$$\text{Magnetic Parity} = (-1)^{L+1}. \tag{2.4}$$

Thus for transitions between states of the same parity, electric moments of odd L angular momentum vanish to conserve parity, and similarly for magnetic moments of even L. Therefore the electric dipole moment and the magnetic quadrupole moment are not observed. In the rest of this work, we will focus on the magnetic dipole moments and electric quadrupole moments of the odd-A manganese isotopes [50].

The Magnetic Dipole Moment

The magnetic dipole moment is a measure of the motion of charges within the nucleus and is a direct measure of the composition of the nuclear wave function. This is written as [52],

$$\mu = g_\ell \ell \mu_{\text{N}}. \tag{2.5}$$

Here g_ℓ is the g-factor associated with the orbital angular momentum, which is used to account for cases in which the charge and mass do not coincide. In this case we refer to the free g-factor, derived for a nucleon in free space, with the assumption that the derivations in free space hold inside the nucleus as well. Later we will have reason to introduce an effective g-factor, which is modified to be more accurate for bound nucleons.

We can now use the same formalism to write the equation for the magnetic moment of a nucleus considering both the orbital angular momentum and the spin [50],

$$\mu = (g_\ell \ell + g_s s)\, \mu_{\mathrm{N}}. \tag{2.6}$$

The values assigned to g_ℓ and g_s can be adjusted, in which case they are the effective g-factors mentioned above, and the magnetic moment for the whole nucleus could in theory be obtained by summing over all nucleons. Since this is too complex a task for almost all nuclei, the shell model can again be used to simplify the procedure. The nucleus can be modelled as a core of nucleons which are paired to spin zero and do not contribute to the magnetic moment, and thus the magnetic moment is determined by the spin state of the last unpaired nucleon, or the valence nucleons, as has been suggested in the previous sections.

Assuming only one unpaired nucleon outside the core, we must then write the result of the one-body operator μ acting on the unpaired nucleon with total angular momentum $\boldsymbol{j}$. In a system in which j is well defined, the quantum numbers ℓ_z and s_z are not, and so we cannot compute the magnetic moment directly from Eq. 2.6. We can, however, rewrite this equation, using the fact that $\boldsymbol{j} = \boldsymbol{\ell} + \boldsymbol{s}$, in such a way that it depends on the expectation value of s, $\langle s \rangle$. This is helpful because the components of $\boldsymbol{s}$ not in the direction of $\boldsymbol{j}$ will cancel out, leaving only the component

in the direction of $\boldsymbol{j}$, which remains constant. After some mathematical manipulations (found in [48] and [52]), two values are obtained for the magnetic moment, depending on the projection of the spin of the unpaired nucleon,

$$j + \frac{1}{2} \rightarrow \langle \mu \rangle = \left(g_\ell (j - 1/2) + \frac{1}{2} g_s \right) \mu_{\mathrm{N}} \tag{2.7}$$

$$j - \frac{1}{2} \rightarrow \langle \mu \rangle = \left(g_\ell \frac{j(j+3/2)}{j+1} - \frac{1}{2} \frac{j}{j+1} g_s \right) \mu_{\mathrm{N}}. \tag{2.8}$$

These are called the Schmidt values [53] and they provide basic guidelines to the experimental value of the magnetic moment, however as can be seen in Fig. 2.1, the measured values often deviate significantly from the predictions of the Schmidt values. This is because the Schmidt formulation does not account for interactions between particles, for instance through the meson exchange current, or the interactions between the single valence nucleon and the core [52]. To compensate for these valence-core effects, effective g-factors can be used in calculations. While these considerations make the computation of magnetic moments difficult, this sensitivity to the configuration of the nucleons can be used as a probe for the nuclear wavefunction [52].

The Electric Quadrupole Moment

The electric quadrupole moment is a measure of the charge distribution within a nucleus and thus can provide direct information about the shape of the nucleus and the degree of collectivity at work between the nucleons. We can begin to derive its form by considering the classical quadrupole moment of a proton [52],

$$eQ = e(3z^2 - r^2) \tag{2.9}$$

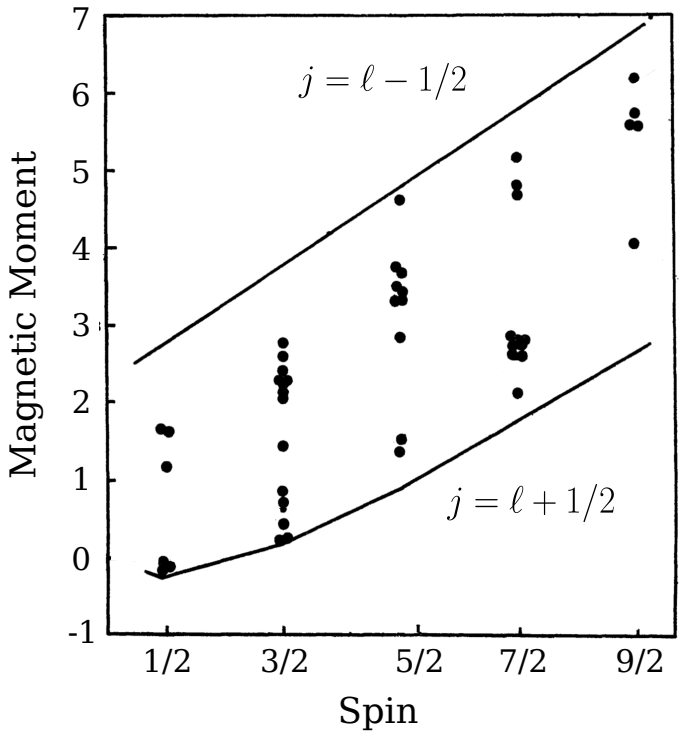

Figure 2.1: Schmidt lines for odd-proton magnetic dipole moments (in μ_N), and measured values for those moments in different isotopes. Figure adapted from [53].

where e is the electric charge, Q is the quadrupole moment and z and r are the usual position coordinates. As with the magnetic dipole moment, this can be applied to a nucleus by summing the contributions of all the nucleons. Since the quadrupole moment is determined by the position of the charges in the nucleus, it is an indicator of deformation and provides a probe for collective interactions among the nucleons. Thus a spherical charge distribution always has a zero quadrupole moment. We also find that nuclei with $j = 1/2$ have a vanishing spectroscopic quadrupole moment, though they may possess an intrinsic quadrupole moment that is not observable. In the limit of strong-coupling, the spectroscopic quadrupole moment observed in the lab frame and the intrinsic quadrupole moment along the axis of deformation of the nucleus are related by [52],

$$Q_s = \frac{3K^2 - I(I+1)}{(I+1)(2I+3)} Q_0 \tag{2.10}$$

where K is the projection of the nuclear spin onto the symmetry axis, Q_0 is the intrinsic moment and Q_s is the spectroscopic moment. This can be related to deformation via the static deformation parameter, $\langle \beta_2 \rangle$, using the formula [5],

$$Q_0 \approx \frac{5Z \left\langle r^2 \right\rangle_{\text{spher.}}}{\sqrt{5\pi}} \langle \beta_2 \rangle \left(1 + 0.36 \langle \beta_2 \rangle\right) \tag{2.11}$$

where $\left\langle r^2 \right\rangle_{\text{spher.}}$ is the radius of an equivalent spherical nucleus of the same volume.

If we again consider the shell model, then we should be able to determine the quadrupole moment by investigating the properties of the valence nucleons. However, the same problems arise here as mentioned for the dipole moments, namely that residual nucleon-nucleon interactions, and interactions with the nucleons in the core, are neglected and must be accounted for by using effective charges. Indeed, in nuclei where the last unpaired nucleon is a neutron, quadrupole moments are measured to be non-zero despite the vanishing quadrupole moment of the neutron itself. This implies

the need to account for other effects when using this formulation of the quadrupole moment [52].

2.2 Hyperfine Interactions

In order to profit from the insights into nuclear structure that the electromagnetic moments can provide, we must first determine how to measure them. This can be done most directly by measuring the hyperfine spectrum of a nucleus. The hyperfine structure, in analogy with the fine structure, is a result of the coupling of angular momenta, and is manifested as small shifts in atomic energy levels.

The non-relativistic kinetic and potential energies in an atom dictate the gross structure of the energy levels, with the difference between adjacent levels on the order of 1-10 eV. On top of this, there are the effects of spin-orbit coupling (as well as relativistic effects) that produce an additional splitting of the energy levels on the order of $10^{-4} - 10^{-5}$ eV. This observed splitting is the fine structure, resulting from the interaction between the magnetic moments of the electrons and the magnetic field produced by the orbits of those electrons around the nucleus. At even finer scales, on the order of $10^{-7} - 10^{-8}$ eV, the hyperfine splitting of the energy levels results from the interaction of the nuclear electromagnetic moments with the electric and magnetic fields produced by the electrons at the position of the nucleus [54]. These measurements require that the nucleus under study have at least $J > 0$ and $I > 0$ [5]. The splitting of atomic energy levels is shown as part of Fig. 2.2.

2.2.1 Energy Components

The hyperfine splitting can be decomposed into two contributions, that from the magnetic dipole moment of the nucleus and that from the electric quadrupole moment. The magnetic dipole contribution results from the coupling of the dipole moment of the nucleus to the magnetic field produced by the orbiting electrons. Classically this is analogous to the alignment of a dipole moment with the surrounding field. In the case of the nucleus, we can write the energy of the interaction as [48],

$$E_\mu = \frac{\mu B_\mathrm{e}(0)}{\hbar^2 I J}(\boldsymbol{I}\cdot\boldsymbol{J}) = \frac{A}{\hbar^2}(\boldsymbol{I}\cdot\boldsymbol{J}) \tag{2.12}$$

where $B_\mathrm{e}(0)$ is the magnetic field produced by the electrons at the position of the nucleus. The factor A is one of the hyperfine coefficients, and is one of the quantities normally measured in an experiment.

In order to evaluate the quantity $\boldsymbol{I}\cdot\boldsymbol{J}$ in Eq. 2.12, we can define a new quantum number $\boldsymbol{F} = \boldsymbol{I} + \boldsymbol{J}$, in analogy to the coupling of $\boldsymbol{L}$ and $\boldsymbol{S}$ to make $\boldsymbol{J}$. F can now range from $|I-J|$ to $I+J$ and follows the same rules as the other quantum numbers. Then we have,

$$\boldsymbol{F}^2 = \boldsymbol{I}^2 + 2(\boldsymbol{I}\cdot\boldsymbol{J}) + \boldsymbol{J}^2 \tag{2.13}$$

which leads to,

$$\boldsymbol{I}\cdot\boldsymbol{J} = \frac{1}{2}\left(\boldsymbol{F}^2 - \boldsymbol{I}^2 - \boldsymbol{J}^2\right) \tag{2.14}$$

$$\langle\boldsymbol{I}\cdot\boldsymbol{J}\rangle = \frac{\hbar^2}{2}\left(F(F+1) - I(I+1) - J(J+1)\right). \tag{2.15}$$

Therefore the energy contribution for the dipole moment is,

$$E_\mu = \frac{1}{2}A\,K \tag{2.16}$$

where $K = F(F+1) - I(I+1) - J(J+1)$ [5].

The energy contribution from the electric quadrupole is a result of the nuclear quadrupole moment interacting with the electric field produced by the electrons at the nucleus. However, the quadrupole moment energy depends not on the field strength, but on the gradient of the electric field at the position of the nucleus. The energy of this interaction can be written as [48],

$$E_{\mathrm{Q}} = eQ\,\frac{\partial^2 V}{\partial z^2}\,\frac{\left[3\left\langle \boldsymbol{I}\cdot\boldsymbol{J}\right\rangle^2\hbar^{-4} + \frac{3}{2}\left\langle \boldsymbol{I}\cdot\boldsymbol{J}\right\rangle\hbar^{-2} - I(I+1)J(J+1)\right]}{2I(2I-1)J(2J-1)}$$

$$= B\,\frac{\left[3\left\langle \boldsymbol{I}\cdot\boldsymbol{J}\right\rangle^2\hbar^{-4} + \frac{3}{2}\left\langle \boldsymbol{I}\cdot\boldsymbol{J}\right\rangle\hbar^{-2} - I(I+1)J(J+1)\right]}{2I(2I-1)J(2J-1)} \tag{2.17}$$

where $\frac{\partial^2 V}{\partial z^2}$ is the gradient of the electric field produced by the electrons at the position of the nucleus. The factor B is another hyperfine coefficient that can be determined from spectroscopy. Higher order hyperfine coefficients exist, but in this case are not relevant [55]. In order to observe the quadrupole splitting, a nucleus must have $I > 1/2$ and $J > 1/2$, as can be seen from Eq. 2.17. Using the relation of Eq. 2.14, and the variable K, the total perturbation to the energy levels of a nucleus is [5],

$$\Delta E = \frac{1}{2}K\,A + \frac{3K(K+1) - 4I(I+1)J(J+1)}{8I(2I-1)J(2J-1)}B\,. \tag{2.18}$$

2.2.2 Measurements of the Hyperfine Structure

The hyperfine structure is measured via a hyperfine spectrum from which the A and B parameters can be extracted, as shown in Fig. 2.2. The spectrum, normally displayed in the frequency domain, is the result of a transition between two states of different J and the frequency of each peak in this spectrum (corresponding to transitions between

F states) can be written as [5],

$$\gamma = \nu + \alpha_{\mathrm{u}} A_{\mathrm{u}} + \beta_{\mathrm{u}} B_{\mathrm{u}} - \alpha_{\mathrm{l}} A_{\mathrm{l}} - \beta_{\mathrm{l}} B_{\mathrm{l}} \tag{2.19}$$

$$\alpha = h\frac{K}{2} \tag{2.20}$$

$$\beta = h\frac{3K(K+1) - 4I(I+1)J(J+1)}{8I(2I-1)J(2J-1)} \tag{2.21}$$

where ν is the centroid of the spectrum and A and B are the hyperfine parameters. In this case, u refers to the upper state, l refers to the lower state and the values used to calculate α and β should be appropriate to either the upper or lower state.

As with transitions between J-states, selection rules apply to transitions between F states and arise from the electric dipole transitions. Thus transitions of $\Delta F = 0, \pm 1$ are allowed, though the transition $F_{\mathrm{l}} = 0 \rightarrow F_{\mathrm{u}} = 0$ is not allowed [5].

The purpose of measuring the values of A and B from the spectrum was to calculate the electromagnetic moments. As shown in Eq. 2.12 and Eq. 2.17, determination of the dipole moment requires knowledge of the magnetic field produced by the electrons at the nucleus ($B_{\mathrm{e}}(0)$) and determination of the quadrupole moment requires knowledge of the electric field gradient produced by the electrons at the nucleus ($\frac{\partial^2 V}{\partial z^2}$). Because these are difficult to calculate, it is simpler to find the moments via a ratio of hyperfine coefficients [5],

$$\mu = \mu_{\mathrm{ref}} \frac{IA}{I_{\mathrm{ref}} A_{\mathrm{ref}}} \tag{2.22}$$

$$Q_{\mathrm{s}} = Q_{\mathrm{s,ref}} \frac{B}{B_{\mathrm{ref}}} \tag{2.23}$$

where the reference values are quantities known for at least one isotope, determined with other experimental methods, and can be for the upper or lower state of the

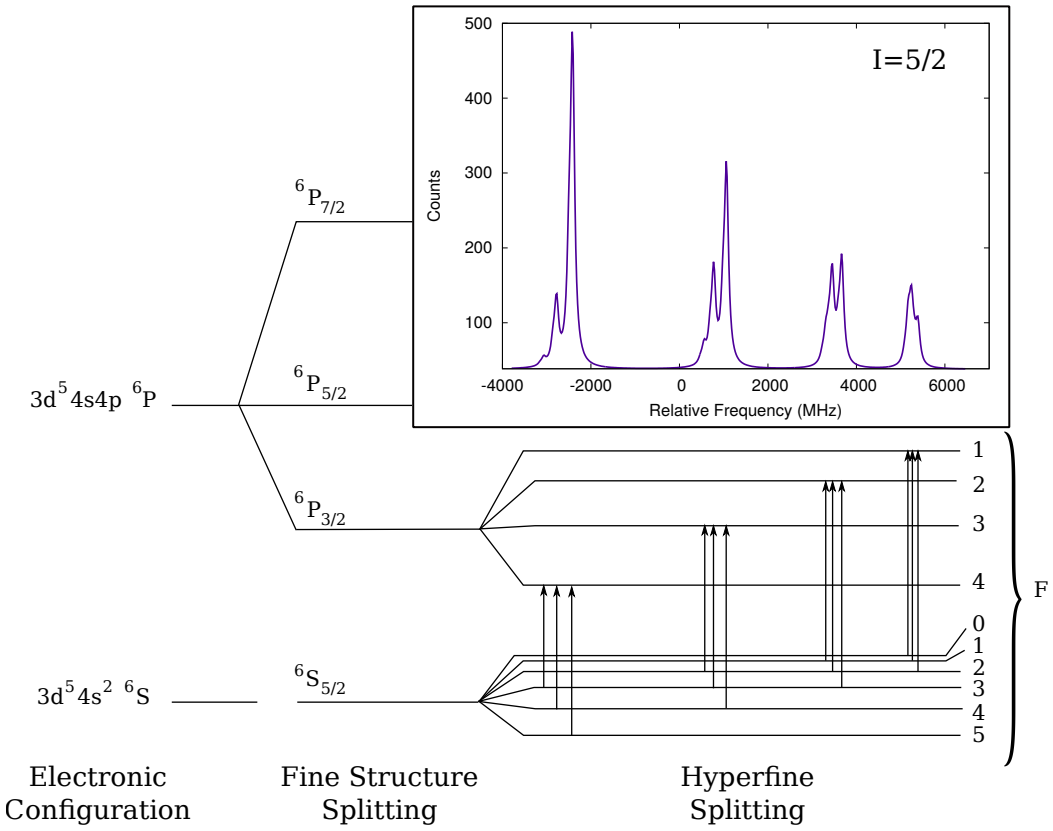

Figure 2.2: The basic atomic structure of Mn for the ground state (lower branch) and excited state (upper branch), split into fine structure energy levels and hyperfine energy levels for the transition used in the atomic manganese experiment. A spectrum fit for ^{55}Mn illustrates how the transitions between F states correspond to spectral peaks.

transition. This makes use of the invariance of the ratio $A_{\mathrm{u}}/A_{\mathrm{l}}$ and $B_{\mathrm{u}}/B_{\mathrm{l}}$ across an isotopic chain to provide an isotope independent method for determining the electromagnetic moments [6].

2.2.3 Isotope Shifts

Another important piece of information available from the hyperfine spectrum is the shift of the hyperfine centroid along the isotopic chain, called the isotope shift. This results from the changing mass and charge distribution inside the nucleus as neutrons are added or removed, and it can be expressed as [56],

$$\delta\nu^{AA'} = \nu^{A'} - \nu^{A} \tag{2.24}$$

where A and A' are two different isotopes. This effect can be further broken down into two components, the mass shift and the field shift [56],

$$\delta\nu^{AA'} = \delta\nu^{AA'}_{\mathrm{MS}} + \delta\nu^{AA'}_{\mathrm{FS}} \,. \tag{2.25}$$

The mass shift results from the change in centre of mass motion between different isotopes, modifying the kinetic energy term of the Hamiltonian. It can be calculated as,

$$\delta\nu^{AA'}_{\mathrm{MS}} = M\left(\frac{A'-A}{AA'}\right) \tag{2.26}$$

where M, the mass factor, comprises several quantities relating to the kinetic energy and is dependent on the transition under study [5].

The field shift is the quantity of interest to nuclear physicists, as it provides information on the nuclear mean square charge radius. As the neutron number in a nucleus changes, the extent and distribution of nuclear charge will also change, not only because the volume has changed but because the proton-neutron interaction

modifies the Coulomb potential. The electronic energy levels shift and the resulting field shift provides sensitive information on the mean-square charge radius. It can be written as [5],

$$\delta\nu_{\mathrm{FS}}^{AA'} = \frac{\pi a_0^3}{Z}\Delta|\Psi(0)|^2 f(Z)\delta\left\langle r^2\right\rangle^{AA'} \tag{2.27}$$

where a_0 is the Bohr radius, Z is the proton number, $\Delta|\Psi(0)|^2$ is the difference in the electron probability density functions for the two states of the transition at the location of the nucleus, $f(Z)$ is a correction factor accounting for relativistic effects due to the proximity of the electrons to the nucleus, and $\delta\left\langle r^2\right\rangle^{AA'}$ is the change in the mean-square charge radius between isotopes A and A'. The atomic factors in these equations can be determined using a King plot, which compares the isotope of interest to isotopes for which the mean-square charge radii is already known. With some corrections, data from different transitions can be compared and charge radii extracted [6]. However, the isotope shift will not be discussed further in this work.

2.3 Shell Model Calculations

The shell model has been very successful to date in predicting the behaviour of nuclei in different regions of the nuclear chart [4]. In order to make use of the shell model, an effective interaction has to be defined which specifies the strengths and types of interactions among the nucleons, and the potential in which they move. There are many such effective interactions for nuclei in different areas of the nuclear chart. We will examine a few that relate to manganese.

Normal filling of the orbitals for manganese would give a configuration of 3 proton holes in the $1f_{7/2}$ shell ($Z = 25$ for manganese) and somewhere between two

neutron holes in the $1f_{7/2}$ shell and a fully filled $\nu\, 1f_{5/2}$ shell, depending on the isotope ($N = 26 - 38$ studied in this work). Thus we should only be interested in the pf shell for both protons and neutrons, however there is evidence that excitations of neutrons past $N = 40$ to the low-lying $g_{9/2}d_{5/2}$ orbitals are also influencing the ground state wave functions (see Ch. 1 and references therein). Level migration, such as the lowering of the single particle energies of the neutron $g_{9/2}d_{5/2}$ orbitals, is an important component in nuclear structure theories (see for instance [3]), and spectroscopy of these nuclei will shed light on the ability of various shell model interactions to predict the occupation numbers of the $g_{9/2}d_{5/2}$ orbitals and how early in the isotopic chain these excitations become important. In addition, for the case of manganese, the position of the protons and neutrons in the same major shell increases the strength of the proton-neutron interaction, giving rise to collective effects, while single particle effects remain significant.

Due to the energy difference of the $f_{7/2}$ orbital from the other pf orbitals, there is a two-shell effect within the pf shell, and mixing across this gap has to be included in any model that expects to describe these nuclei, necessitating consideration of at least the entire pf shell for protons. However, computations such as this are at the edge of our technical abilities, making this a challenging region to study. We will consider two shell model effective interactions here that will later be compared to the results of experiments in order to deduce information on the structure of the studied nuclei.

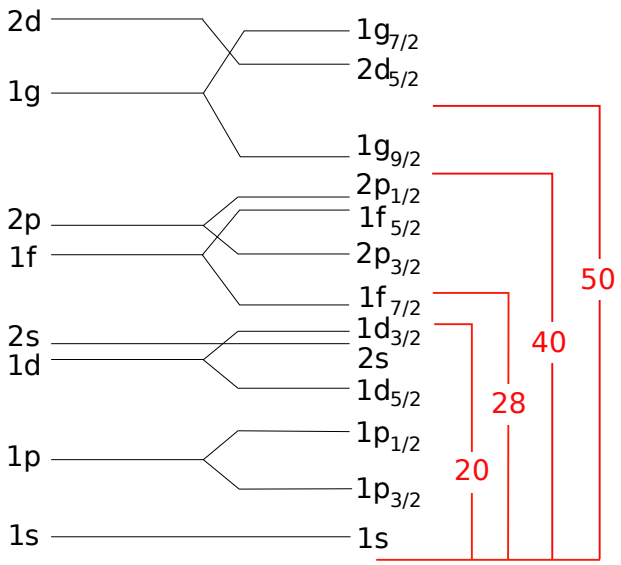

Figure 2.3: Nuclear levels diagram showing, among others, the levels used in the described effective interactions.

2.3.1 GXPF1A

The GXPF1A effective interaction [2], based on a modification to five of the matrix elements in the GXPF1 interaction [1], has been used to effectively describe many properties of nuclei is the pf shell. The monopole part of the GXPF1 interaction was developed by taking microscopic nucleon-nucleon interactions and modifying them such that the results of calculations conform to a large data set of energy levels for isotopes in the range $A = 47 - 66$. The challenge was to describe the excitations across $N = Z = 28$. This was accomplished by replacing the original core of ^{56}Ni with a more realistic ^{40}Ca core. This allowed the necessary "cross-shell" mixing. The interaction has been successful in describing properties such as the electromagnetic moments of ^{53}Mn, ^{54}Fe, ^{55}Co and ^{56,57,58,59}Ni [1]. Different truncations, indicating the maximum number of particles allowed to be excited past $N = Z = 28$, were

needed for different isotopes. For Ca, Sc, Ti, V, and Cr no truncation was necessary, however for Mn the calculations required a truncation to 6 or fewer nucleons for computational reasons. A limitation which becomes clear, and is identified by the creators of the GXPF1 interaction [1], is the exclusion of the orbitals above $N = 40$ in the model space, which makes this interaction unsuitable to describe the more neutron-rich isotopes, though it is very effective at lower masses. Thus to describe manganese isotopes towards $N = 40$ an interaction is required that will include the gd orbitals.

2.3.2 LNPS

The LNPS effective interaction [3] was created as a way to extend the possible computations of pf shell nuclei to more neutron-rich isotopes. LNPS is a reaction to the inability of interactions in the fpg space (the pf shell, plus the $g_{9/2}$ orbital) to reproduce the 2_1^+ state of ^{66}Fe. Thus LNPS includes the full pf space for protons and the $pf_{5/2}$ space plus $g_{9/2}$ and $d_{5/2}$ orbitals for neutrons.

The interaction was developed as a hybrid of several two-body interaction matrices with monopole corrections. It uses a ^{48}Ca core, though some calculations have also been done using the less robust ^{40}Ca core in order to extend the LNPS applicability towards lower masses. In the creation of LNPS, the $Z = 28$ gap was fixed to reproduce the $B(E2)$ values in ^{80}Zn, and it allows 14 particle-14 hole excitations across $Z = 28$ and $N = 40$ [3]. In Ch. 4 and Ch. 6, we assess the ability of the two described interactions to predict the electromagnetic moments of the neutron-rich, odd-even Mn isotopes. The model space necessary to reproduce the observables indicates the importance of excitations across $N = 40$ and $Z = 28$.

Chapter 3

The ISOLDE Facility

The ISOLDE facility [57], where this work was carried out, is located at the European Organization for Nuclear Research (CERN) and specializes in the production of radioactive ion beams for studies ranging from biology to nuclear structure. Beams of exotic isotopes far from stability can be provided to low-energy experiments at energies up to 60 keV, or can be post-accelerated up to 3 MeV/u [58] (10 MeV/u after the installation of the superconducting linac for HIE-ISOLDE [59]). A layout of the facility is shown in Fig. 3.1. ISOLDE has two target stations which receive the pulsed primary beam of 1.4 GeV protons produced by the Proton Synchrotron Booster (PSB). For the purposes of the experiments described here, only the target station attached to the High-Resolution Separator (HRS) beamline is necessary.

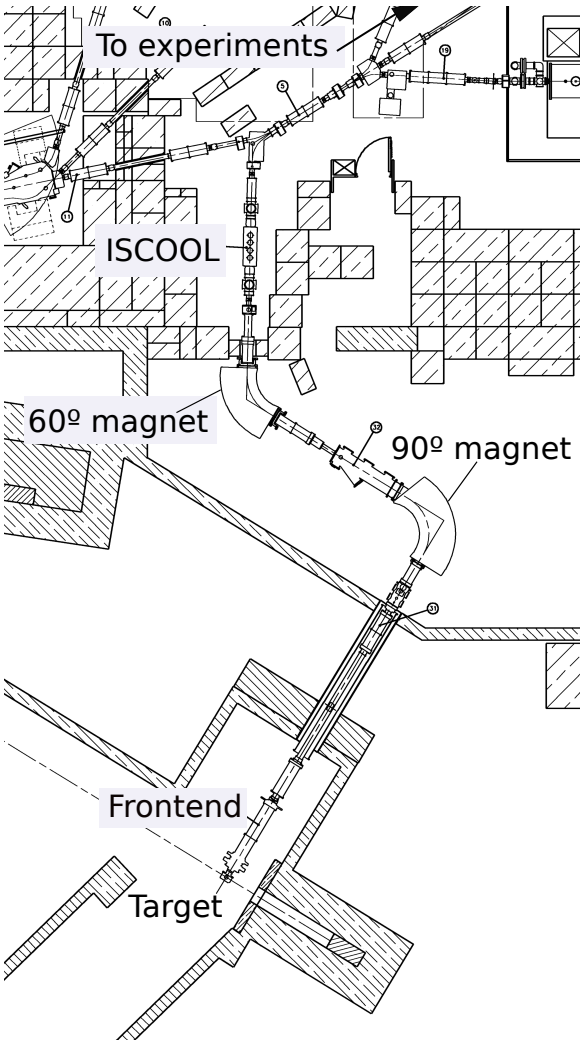

Figure 3.1: Layout of the HRS line at ISOLDE, showing the ion production in the target, extraction through the frontend, mass separation in the two dipole magnets, cooling and bunching in ISCOOL and final delivery to the experiments.

3.1 Isotope Production

Isotopes are produced at ISOLDE by bombarding a thick target with bunches of protons. Radioactive nuclei are produced in the target material either through spallation, fragmentation or fission, and then diffuse out of the target material and effuse through a hot or cold transfer line to the ion source. A good target must be able to produce the isotope of interest in sufficient quantities (defined by each experiment) and it must be possible to extract these isotopes as ions before a significant portion of the beam is lost to radioactive decay. As a result of these requirements, the choice of target material and design depends on the production isotopes in a complex way. The production of a certain element and in what quantity, is, to a large extent, a function of the target material - ISOLDE targets are made from materials such as uranium carbide, calcium oxide and thorium carbide. The design of the target also influences the production of isotopes, as well as the diffusion time of the elements throughout the target system. A more porous target allows a faster diffusion time which is advantageous for short-lived species, however a more dense target increases the number of reactions obtained in a specific volume and thus the overall isotope production. The target is heated to around 2000° C in order to reduce the probability of particles sticking to the surfaces and to decrease the diffusion time. Targets can be made of solids, powders or liquids and the design of high-performance targets is an area of ongoing development [60].

Once the isotope has been produced in the target, it must be ionized. The primary ion sources at ISOLDE are surface sources, plasma sources and laser sources. Surface sources ionize atoms through contact with a hot surface of high work function, which readily accepts electrons if the ionization potential of the element is less than the

work function of the ion source material.

In a plasma source, atoms are ionized by interaction with a plasma, which is created by accelerating electrons into a gas. A magnetic field surrounds the ion source, which helps confine the plasma, thus increasing its density and the efficiency of the source. The magnetic field also increases the energy of the electrons, making the plasma creation process more efficient.

Laser ion sources excite an electron in the atomic shell stepwise towards the ionization potential using a combination of lasers specifically designed to match the energy fingerprint of each element.

3.2 Beam Production

Once ionized, the particles are extracted from the ion source as a beam, the energy of which is determined by the potential of the target and ion source system. At ISOLDE, the target unit (see Fig. 3.2) houses all the elements of the target system discussed in Sec. 3.1 and is floated on high voltage up to a maximum of 60 kV. When the singly ionized particles leave the target unit to be transported through the rest of the ground-potential beamline, they leave with an energy defined by the value of the high voltage. As will be discussed later (Ch. 5), other elements in the beamline can be floated on high voltage to decelerate the incoming beam or to modulate its energy (see Sec. 3.5). The transport through the rest of the beamline is accomplished using almost exclusively electrostatic elements. Electrostatic systems are mass-independent, and are used to steer and focus the beam.

The produced beam is monitored by beam diagnostic devices, a term which encompasses all the devices used to measure beam position, divergence, shape, intensity

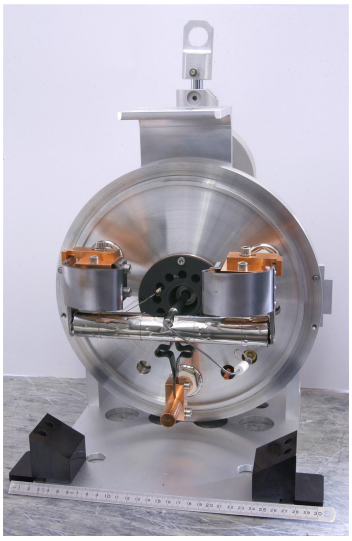

Figure 3.2: Target system used at ISOLDE, shown without its protective housing. The long silver tube holds the target material [61].

and structure. The most common are faraday cups and wire scanners, which are used to monitor the total beam current and the transverse beam profile, respectively.

The first major element the beam encounters after extraction from the ion source is the HRS [62], which consists of a 90° bending magnet and a 60° bending magnet. Passage through the dipole fields of these magnets sends particles of different charge-to-mass ratio on different paths. Since each particle is singly charged, a particle of a certain mass can be selected by tuning the magnetic field. Selection of one mass, however, does not preclude contaminants in the beam coming from isobars which may be produced and ionized along with the intended beam.

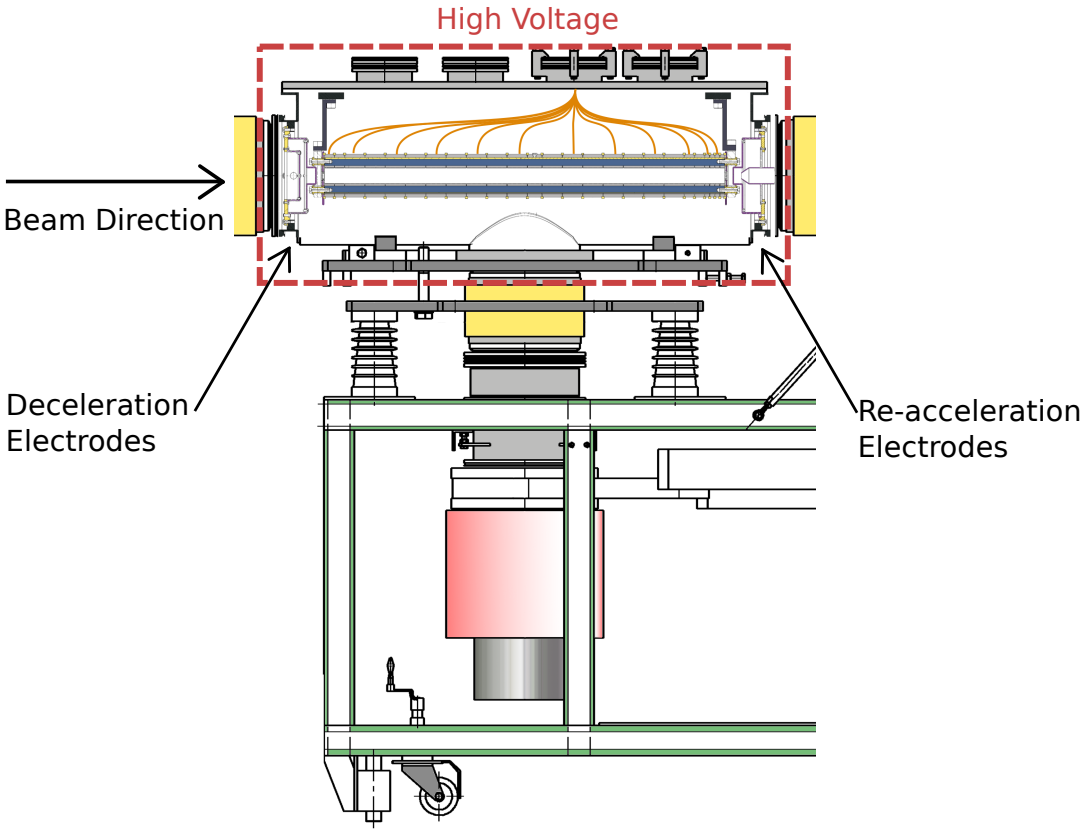

Figure 3.3: Schematic view of ISCOOL showing the area which is on high voltage, as well as the injection deceleration electrodes and extraction re-acceleration electrodes. The cylinder that connects these areas is the helium-filled Paul trap.

3.3 Cooling and Bunching

After separation in the HRS, the ion beam is then passed through the radio frequency quadrupole cooler and buncher (ISCOOL, [63]), shown schematically in Fig. 3.3.

ISCOOL is a helium-filled Paul trap, the purpose of which is to reduce the transverse and longitudinal emittance of the beam via elastic collisions with the He atoms, and to provide a bunched beam if necessary. The machine is located on a high voltage

platform and the voltage of the platform approximately matches the voltage of the target. Thus the ions travelling on ground-potential with an energy corresponding to the target high voltage encounter a positive voltage of the same magnitude and, through a series of electrodes, are decelerated to a low energy (around 100 eV) for injection into ISCOOL. At the exit of ISCOOL, the process is reversed and the ions are re-accelerated up to their incoming energy as they leave the high voltage platform.

ISCOOL can be operated in either continuous mode (the beam passes straight through) or bunching mode (the beam is trapped for a time at the extraction end of the machine before being released in bunches). The bunching is achieved by creating a potential well on the axis of the machine with a potential barrier at one end that can be raised and lowered to bunch and release the beam. All beams coming from the HRS must pass through ISCOOL in one of these two modes and thus all HRS beams benefit from the reduced emittance it provides. The bunching feature is especially important to the experiments described here, where it is used to significantly reduce the signal to noise ratio (see Sect. 3.5). The operation of ISCOOL, and the improvements made as part of this work, are described in more detail in Ch. 5.

Once the beam leaves ISCOOL, it can be directed to an experimental setup through the many beamlines available at ISOLDE, or it can be post-accelerated using the REX beamline. Here we discuss only the use of the beam at the low-energy experiment COLLAPS.

3.4 Collinear Laser Spectroscopy

Collinear laser spectroscopy is a method used in nuclear physics to probe the spin, electromagnetic moments and mean-square charge radius of an isotope. The spectral signatures of these quantities can easily be obscured by the effects of Doppler broadening due to the velocity spread induced by a hot cavity ion source (or pressure broadening in a gas cell) which can increase the line width to several GHz. The main advantage of collinear laser spectroscopy is the reduction of this broadening in order to resolve the structure of the spectrum. It is accomplished by overlapping a fast atom (or ion) beam with a co-propagating laser whose frequency can be scanned in the rest frame of the beam. The laser excites the atoms and the photons released during their subsequent decay can be registered with photomultiplier tubes or other photo-detection systems. In this way, the resonant frequency of the transition in the atomic shell can be found [5]. Here we will focus on the use of this technique for measuring the hyperfine structure of a nucleus by scanning the laser frequency seen by the beam over the range of the hyperfine splitting.

The reduction of the Doppler broadened linewidths is achieved through the acceleration of the beam. This is because the electrostatic elements used to accelerate the beam change the energy equally for all ions, conserving the initial energy spread of the ensemble. Thus the product of velocity and velocity spread remains constant. This can be seen in the equation,

$$\begin{aligned} \delta E &= \delta\left(\frac{1}{2}mv^2\right) \\ &= mv\delta v \end{aligned} \tag{3.1}$$

where E is the beam energy, m the mass, and v the velocity. As the velocity increases,

the velocity spread decreases and thus longitudinal acceleration results in a reduction of the effects of broadening from the source [64].

Collinear laser spectroscopy provides additional advantages over other forms of optical spectroscopy. The use of the collinear geometry means that in principle the entirety of the atom beam can be probed by the laser, and that the interaction time is much longer than it would be in the case of perpendicular laser/atom beams, making this a high-sensitivity technique. In comparison to the perpendicular case, the collinear geometry also means a reduction of the observed linewidth of the transition. If the laser and atom beams are at 90° to one another, the linewidth of the transition is dominated by the time each particle spends traversing the laser beam, which is generally much shorter than that associated with the natural lifetime of the transition. This results in a broadening of the line, since [65],

$$\Delta\nu \sim \frac{\Delta E}{h} \sim \frac{1}{2\pi\Delta t} \tag{3.2}$$

where E is the energy, t is the time and the Uncertainty Principle $\Delta E\Delta t \sim \hbar$ has been used. In the collinear geometry, the transit time of the atoms through the laser beam is much longer, and so high-resolution measurements are possible [66].

Finally, collinear laser spectroscopy takes advantage of the ability to relatively easily control the velocity of the radioactive beam. Instead of scanning the frequency of the laser over the hyperfine splitting, which can cause instabilities, the velocity of the ions can be scanned such that the frequency, as seen by the atoms in their rest frame, matches the range of interest. The total accelerating voltage applied to the ions is related to the measured frequency by the equations,

$$\nu = \nu_{\text{laser}} \left(1 + \alpha - \sqrt{2\alpha + \alpha^2}\right) \tag{3.3}$$
$$\alpha = \frac{eV}{mc^2}$$

where ν is the observed frequency, ν_{laser} is the laser frequency, m is the mass of the isotope, e is the electric charge, V is the total accelerating voltage, which can be tuned by the post-acceleration electrodes, and c is the speed of light [5].

3.5 COLLAPS Experimental Setup

COLLAPS is ISOLDE's permanent collinear laser spectroscopy experiment. Here, the ion beam from ISCOOL is converted into an atom beam via a charge-exchange cell (if atoms are being studied, as is usually the case), then the neutral beam is overlapped with a co-propagating laser in order to excite the electrons to a higher level in the atomic shell. When the excited electrons decay back to their original energy level, photons are released which correspond to the energy difference between two levels. As the frequency seen by the atoms is cycled, these photons are recorded by a photo-detection system and a spectrum is constructed from which the parameters of interest can be extracted. A schematic view of the setup is shown in Fig. 3.4 and supplementary information is given in [67].

The ion beam is produced as described in Sec. 3.1, 3.2 and 3.3 before being delivered to the COLLAPS setup. The ions are deflected into the COLLAPS beamline, then pass a series of injection electrodes designed to maintain the beam focus upon entry into the charge-exchange cell (CEC), which is floating on the Doppler tuning potential. The injection electrodes increase the potential incrementally, as shown in

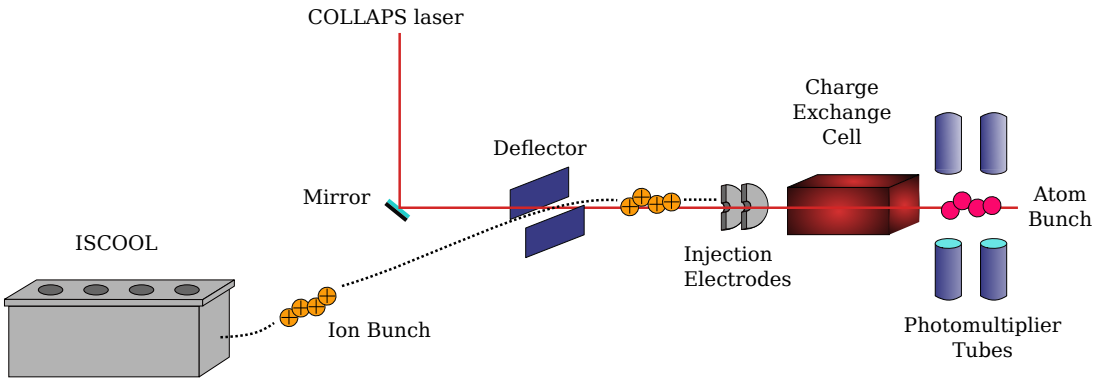

Figure 3.4: Layout of the COLLAPS experiment.

Fig. 3.5, up to the full Doppler tuning potential which is adjusted in order to scan the laser frequency as seen by the ions in their rest frame (see description in Sec. 3.4). The total acceleration voltage of the ions (which determines the measured frequency) is a combination of four factors,

$$V_{\text{total}} = V_{\text{ISCOOL}} - V_{\text{post accel.}} \tag{3.4}$$

$$V_{\text{post accel.}} = V_{\text{DAQ}} \times k_{\text{ampl.}} + V_{\text{offset}}. \tag{3.5}$$

The post acceleration voltage, $V_{\text{post accel.}}$, is a combination of all the voltages that make up the Doppler tuning potential which is applied to the charge-exchange cell. The first component is the DAQ voltage, $V_{\text{DAQ}} = \pm 10\text{V}$, output from the computer by an 18-bit DAC and responsible for scanning the velocity of the ions. This voltage is amplified by a linear-voltage amplifier with a factor $k_{\text{ampl.}} \approx 50.0$, which is calibrated throughout each experiment for accuracy. In order to have more versatility in terms of beam energy and laser frequencies, an offset voltage of $V_{\text{offset}} = \pm 10\text{kV}$ is floated on the $V_{\text{DAQ}} \times k_{\text{ampl.}}$ potential. Finally, the incoming energy of the beam is determined by the energy with which it exits ISCOOL, regulated by the value of the high voltage

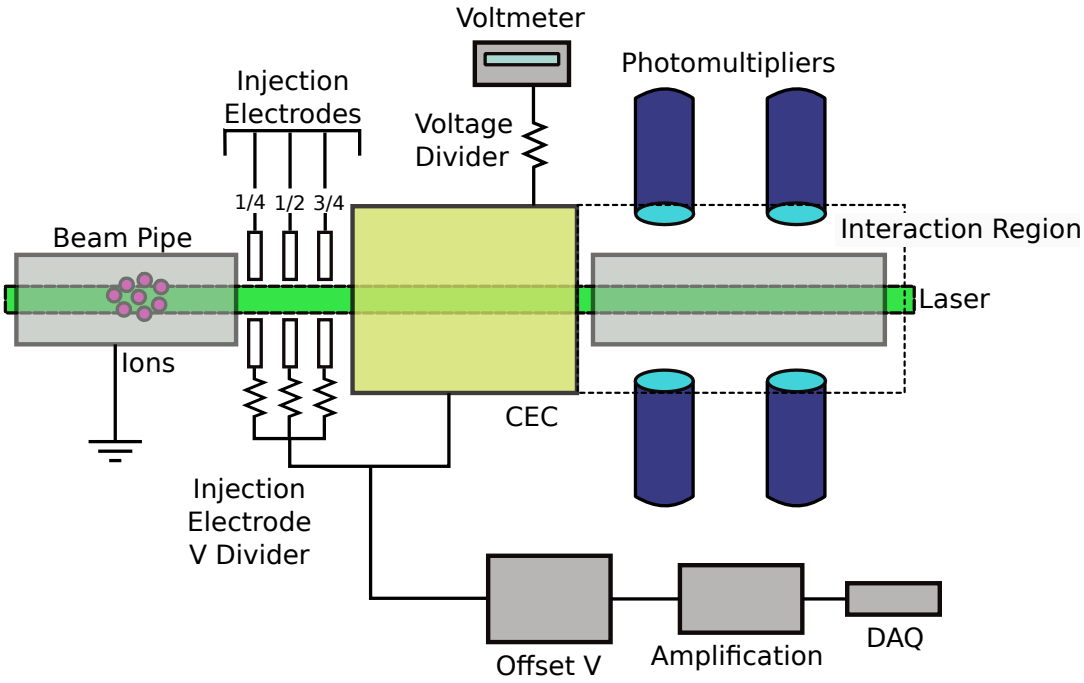

Figure 3.5: Application of voltages at COLLAPS for atomic beams.

platform (V_{ISCOOL}, see Sec. 3.3). Fig. 3.5 shows how these voltages are applied to the beamline. Knowledge of the precisely-regulated velocity of the ions allows the voltage spectrum to be converted into a frequency spectrum using Eq. 3.3.

3.5.1 Charge-Exchange

The charge-exchange cell serves the purpose of neutralizing the ion beam in-flight using an alkali metal vapour. Alkali metals are ideal for this purpose because they have one electron in the outer shell, a large cross section for resonant charge-exchange and a large energy difference between the ground state and the first excited state [68].

The charge-exchange vapour is created by heating a solid (for instance a piece of

sodium) incrementally until the desired internal pressure is achieved, and recondensing this vapour near the exits of the vacuum chamber to prevent contamination of the beamline. The ideal pressure is usually determined in real time or chosen based on previous experience. If the pressure is too low, the efficiency of the CEC will also be low, resulting in significant beam losses due to non-neutralized ions. If the pressure is too high, the probability of inelastic interactions in the CEC will increase. These processes can change the longitudinal energy of the exiting atoms, producing a shift in frequency observed in the spectrum [68], and may adversely affect the emittance of the beam. Though atoms are often chosen for spectroscopy, ions can also be used and in this case the charge-exchange cell is not needed.

Once the atom beam emerges from the CEC, it passes through the interaction region, which is surrounded by photomultiplier tubes positioned at 90° to the direction of the beam. Here the atom beam interacts with the laser and is excited to a higher energy state, provided it is on resonance. The atoms decay back to a lower-lying state by emitting a photon, which is detected by the photomultiplier tubes in order to construct a spectrum. Sources of background here are dark counts and non-resonant scattered laser light.

3.5.2 Data Collection

The data collection is controlled by a multi-channel scalar (MCS) and a custom-designed data acquisition program. The first step to taking data is setting a scan region in volts. This region is determined for each experiment first via calculation using Eq. 3.3 and the literature value for the frequency of the transition between the two j states (ignoring the hyperfine structure), then fine-tuned in real time by

examining the spectra. The scan region is then divided into the number of voltage steps needed to resolve the hyperfine splitting such that with the passage of each bunch, the post-acceleration voltage is advanced by one step. In order to do this, the MCS must trigger the release of each bunch from ISCOOL (for the justification of bunched beam spectroscopy, see the next section). The exact time window (usually around 6 μs in width) during which the MCS accepts photons is determined by the flight time of the ions from the exit of the cooler to the interaction region, and is first estimated as,

$$\text{ToF} \propto \sqrt{\frac{\text{mass}}{\text{energy}}} \tag{3.6}$$

then confirmed experimentally on a case-by-case basis (generally in the range of 50 μs). The MCS can also be gated on the impact of the primary beam on the target (proton triggering, see next section). The same voltage scan is repeated several times over to build up statistics and avoid any errors associated with one particular scan.

3.5.3 Background Reduction

ISCOOL can be used to reduce the background due to non-resonant scattered photons by performing spectroscopy on a bunched beam instead of a continuous beam. With a bunched beam, the photomultipliers can be triggered to accept photons only during the time the atom beam is passing through the interaction region, eliminating a significant fraction of the continuously scattered laser light without losing any resonantly scattered atomic photons. The reduction in the noise is equal to the bunching time divided by the temporal bunch length, which typically yields a background suppression of the order of 10^4 [5].

Another method for enhancing the signal to noise ratio and for increasing the sensitivity to structures with different half lives (i.e. isomers) is a technique called proton triggering. This refers to triggering the data acquisition system to either release a bunch or advance to the next voltage step only within a specific time window after a proton pulse on the target. The proton pulse on target signals (approximately) the time of highest isotope production, after which production falls off due to radioactive decay, until the next proton pulse. The time window chosen is normally one or a couple half lives of the isotope of interest, ensuring that photomultiplier counts are registered only while these isotopes are still present in a considerable fraction.

3.5.4 COLLAPS Laser System

The COLLAPS laser is used to excite the atoms being studied to a higher, unstable level, and the photons emitted upon decay are recorded to form a spectrum. This laser is a low power, narrow line-width dye jet laser operating in CW mode. It is pumped by a Nd:YAG laser with 10 W of power and the final output is frequency doubled to meet the experimental requirements. The laser is set up as a ring cavity with the beam circulating counterclockwise in the top loop, as shown in Fig. 3.6, achieved using an optical diode operating under the Faraday effect [65]. The modes are selected using the combination of a birefringent filter, which provides a bandwidth of 2 GHz, and an etalon assembly which has a bandwidth of 10 MHz. A galvanometric rotating Brewster plate before the output coupler compensates for cavity length drifts. See [65] for a review of relevant photonics concepts and devices. The primary laser setup is shown in Fig. 3.6.

To provide the 280 nm wavelength needed for the atomic Mn experiment, the

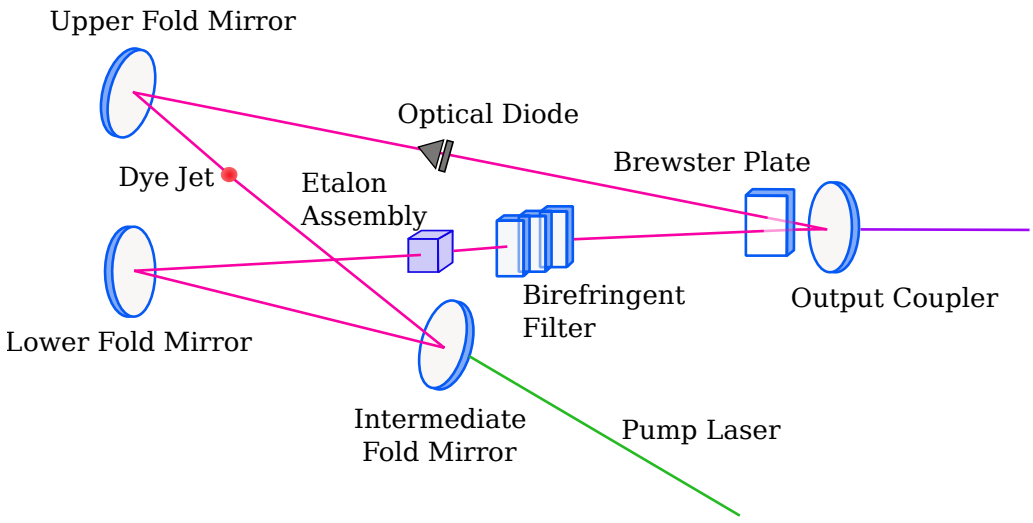

Figure 3.6: Schematic of the main dye laser setup at COLLAPS, with the dye jet oriented perpendicular to the page.

beam from the dye jet laser was frequency doubled using an external ring-cavity frequency doubler. The frequency doubling is accomplished using a non-linear, Lithium Triborate crystal inside a triangular-shaped Delta cavity. The cavity consists of two folding mirrors, the doubling crystal and a piezo-mounted, Brewster-cut prism. The beam circulates multiple times in this cavity before passing out through the second folding mirror, increasing the efficiency of the process. Stabilization is achieved using the Pound-Drever-Hall technique [69], which is based on measuring the derivative of the intensity of the reflected light in a Fabry-Pérot interferometer. The fundamental is resonating correctly in the interferometer when the intensity of the reflected light is zero, and whether the cavity length is too high or too low can be determined by taking the rate of change of the intensity of the reflected light as the frequency is changed by small amounts. In practice, it is easier to change the phase than the frequency so a phase-modulator is used to produce the sidebands. These bands should

be separated from the main resonance by about 100 MHz in order to be efficiently detected. Phase sensitive electronics then send an error signal to the piezo-mounted prism which adjusts the cavity length.

Long-term stabilisation of the fundamental beam was done by locking the dye laser to a frequency-stabilized helium-neon laser (He:Ne). Two beam splitters were used to channel part of the dye laser beam to the He:Ne laser setup and part to the wavemeter, which has its own internal He:Ne laser for continuous calibration. The stabilization He:Ne setup and the component of the laser beam are overlapped in a piezo-driven Fabry-Pérot interferometer by a polarizing beam splitter, and split again at the output of the interferometer by another beam splitter, which directs the beams onto two photodiodes. The He:Ne photodiode is used to lock the interferometer to its frequency and the dye laser photodiode is coupled to the external control input of the dye laser in order to feed in the error signal.

The primary dye laser beam is directed to the COLLAPS beamline via a series of mirrors and a telescope to adjust the focus and size of the beam. It passes into the vacuum chamber via a Brewster window and the power can be adjusted with neutral density filters.

Chapter 4

Atomic Mn Experiment

Collinear laser spectroscopy was performed on a beam of atomic manganese in order to measure the hyperfine structure of the odd-even isotopes in the range $A = 51 - 63$. From the spectra, the spins and hyperfine parameters were extracted, which allowed the calculation of magnetic dipole moments for these isotopes. These values were then compared to the results of large scale shell model calculations in order to investigate the size of the $N = 40$ subshell gap, the importance of the orbitals outside the pf shell and the role played by both neutron and proton excitations.

4.1 Manganese Production at ISOLDE

In this experiment, manganese ions were produced by the impact of the 1.4-GeV pulsed proton beam from the PS Booster on a thick uranium carbide target. The official CERN yield for ^{63}Mn, the most exotic manganese isotope measured in this experiment, is 2×10^5 ions/μC from the primary beam on a UC_x target [70]. However, this yield is only a guideline and actual yields vary significantly with online conditions.

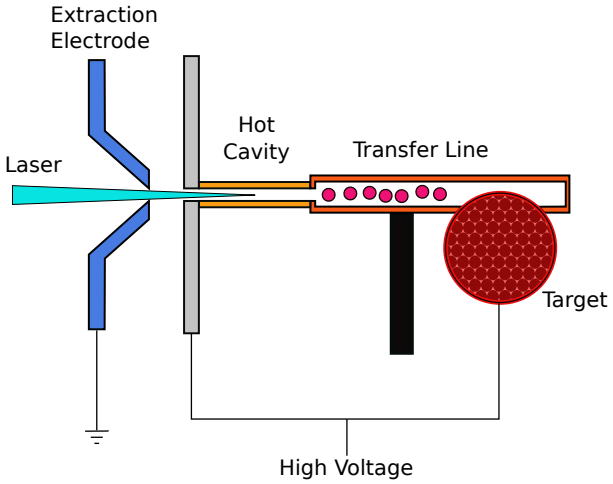

Figure 4.1: A cross sectional view of the setup for the RILIS ion source, showing the target, transfer line, hot cavity and extraction electrode.

The yield of Mn ions was increased, and isobaric contaminants minimized, through the use of ISOLDE's resonant laser ion source (RILIS, [71]). RILIS is often employed to ionize elements that are either inefficiently ionized or not available through surface or plasma ion sources, and can provide ionization efficiencies between 1 and 30% [71].

The RILIS concept of stepwise photo-ionization relies on the uniqueness of the pattern of atomic energy levels for a particular element. The energy of the photons produced by each laser in the (usually) three-step process corresponds to the energy of a transition in the atomic shell. Using the right combination of transitions, an electron can be freed from the atom, creating an ion. This is done inside the hot cavity of the ion source in order to confine the atoms until they are ionized and extracted by the potential difference between the extraction electrode and the target unit (see Fig. 4.1). The laser beams enter the ion source by passing through a quartz window on the back of the first (90°) bending magnet and travelling straight to the

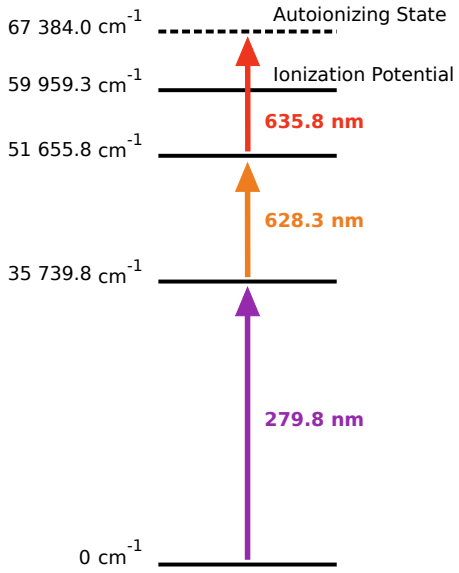

Figure 4.2: Three-step ionization scheme used by RILIS to produce manganese ions. The autoionizing state results when the total excitation energy in the atom is larger than the ionization potential, resulting in the release of an electron.

target unit. See Fig. 3.1 for the ISOLDE layout.

The repetition rate of the lasers must match the residence time of the atoms in the cavity in order to minimize duty cycle losses and ensure that each atom has a laser interaction. High repetition rate lasers are used at around 10 kHz to match the $\sim 100\,\mu$s that the average atom spends in the ion source [72]. RILIS was used to produce manganese ions for both experiments described here with an efficiency around 19% [71]. The scheme used is shown in Fig. 4.2.

For this ionization scheme, two dye lasers and a titanium saphire (Ti:Sa) laser were employed. All three were pulsed, high-power, broadband lasers, pumped by Nd:YAG lasers providing around 40 W of pumping power. The Ti:Sa laser provided the first step of the ionization scheme with about 30 mW of power on the laser table,

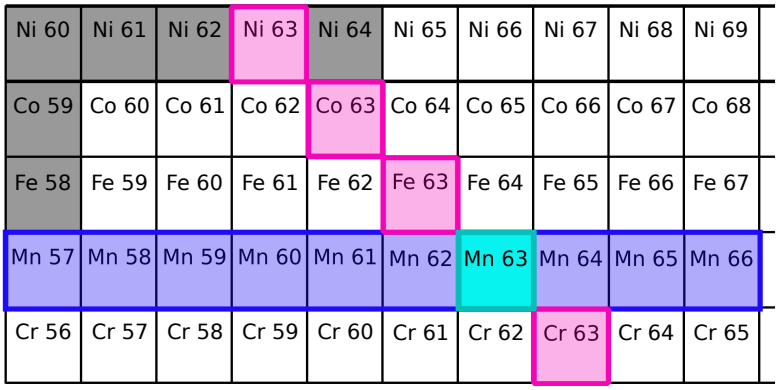

Figure 4.3: The element-selective capabilities of the laser ion source (blue) combined with the mass selective capabilities of the separating magnets (pink) allows the selection of one isotope with low levels of contaminants.

while the second and third steps were provided by the dye lasers with approximately 2.5 W on the table.

RILIS is a powerful tool for reducing beam contamination since atoms are ionized in a chemically-selective way using the atomic properties of each element. The combination of the element-selective ion source and the mass-selective dipole separator can produce beams of very high purity. Fig. 4.3 demonstrates this concept. Laser ionization, however, does not eliminate all contamination, since some isobars can still be surface ionized in the hot cavity. The level of contamination in an experiment is determined on a case-by-case basis. For Mn, the most likely contaminant is neutron-deficient, surface ionized Ga, however this was not deemed to be a significant portion of the beam.

4.2 COLLAPS Setup

After passage through the HRS, the Mn ions were trapped in ISCOOL for approximately 50 ms before being released in 6 μs bunches to the COLLAPS beamline. The beam energy, determined by the potential of the ISCOOL high voltage platform, was 40 keV. The alkali vapour used in the charge-exchange cell in this case was sodium, and three photomultiplier tubes were in operation to register the atom-laser interactions.

The atomic transition chosen for this experiment was from the well-populated $3d^5\,4s^2\ {}^6S_{5/2}$ ground state to the $3d^5\,4s4p\ {}^6P_{3/2}$ excited state at 35 689.98 cm^{-1} [73]. This transition was chosen as it is the most efficient from the ground state [74], and it meets the requirement that the necessary wavelength of 280.2 nm is feasible with the COLLAPS laser. The two other available ground state transitions, to states with $J = 5/2$ and $J = 7/2$, did not provide any spectroscopic improvements over the transition to the $J = 3/2$ state, and the higher spin values mean that the hyperfine structure is split over more peaks, reducing the intensity of each peak, and thus lowering the spectroscopic sensitivity.

The laser frequency was set to 17 867.0092 cm^{-1} and was then frequency doubled to provide approximately 1-3 mW of light during the experiment (see Sec. 3.5.4 for the laser setup). Near the end of the run, there was a slight shift in frequency to 17 867.0083 cm^{-1}, at which the laser was re-locked, and this has been compensated for in the analysis. As described in Ch. 3, the photons released when the atoms decayed back to the ground state were registered by the photomultipliers, which were triggered to only accept photons when an atom bunch passed through the interaction region. This reduced the background counts by $\sim 10^4$.

The correct scan region was first estimated by taking the known fine-structure transition frequency of ^{55}Mn. The total post acceleration voltage was then advanced from the lowest bound of the scan region, in pre-determined steps, to the highest bound, with one bunch released per step. The number of steps must be a compromise between the desired resolution of the scan and the amount of time required.

In the case of ^{63}Mn, which has a shorter half life than the other isotopes (250 ms [75]), a proton triggering technique was used which consists of accepting photons only during a time window after each proton impact on target corresponding to one half life of the isotope. The data acquisition system then advances the voltage scan for every cycle. This enhanced the signal to noise ratio on the observed hyperfine structure by further suppressing the stray light background.

4.3 Analysis

The spectra for the odd-even Mn isotopes were recorded on a computer and analysed with the intention of extracting the spins and hyperfine A and B coefficients, which is done by comparing the relative positions of the hyperfine peaks (see Ch. 2). The spectra were first recorded as a function of voltage then were converted to frequency during analysis using Eq. 3.3. A reference frequency was subtracted from each spectrum in order to make it easier to deal with the frequency values, which are in the THz range when converted directly from voltage. This does not change the extracted parameters, since only relative frequencies are of interest. The reference value used was the known centre-of-gravity for ^{55}Mn ($35\,689.980\,\mathrm{cm}^{-1}$ [73]). The spectra were then fit using a least-squares minimization procedure. After determining appropriate starting values for the minimization from individual spectra, all the spectra for one

isotope were fit simultaneously, giving the most robust results.

The extracted errors on the fit parameters are taken from the least squares code - the covariance matrix is calculated and the standard deviation of each parameter is taken from the square root of the diagonal elements. The errors are then calculated as,

$$\text{Error} = \sigma \times \sqrt{\chi^2_{\text{R}}} \tag{4.1}$$

where χ^2_{R} is the reduced chi-square and σ is the standard deviation from the covariance matrix.

The line shape used to fit the atomic data was a non-normalized Lorentzian, given by [66],

$$L(x) = I\,\frac{\Gamma}{4((x-x_0)^2 + (\frac{1}{2}\Gamma)^2)}$$

where I is a parameter describing the intensity of the peak, Γ is the full width at half maximum and x_0 is the centroid. A Voigt line shape [66] (a convolution of Gaussian and Lorentzian line shapes) is a more physically accurate choice, since the natural line-shape of an atomic transition is Lorentzian, and any broadening (Doppler, thermal, etc.) as a result of the beam production process is Gaussian, however a comparison of fits using Voigt and Lorentzian profiles showed no difference in the extracted values. For this reason, the less complex and time-intensive Lorentzian fit was chosen. Due to the low laser power used to excite the transition, it is likely that each atom interacted with the laser only once during its time in the interaction region. This assumption allowed us to constrain the relative intensities of the hyperfine peaks in the fit to the Racah values [76] at 90°, which are determined using angular momentum coupling rules. This stabilised the fit for the cases in which some peaks in the spectrum were not resolved. An equivalent fit, with the intensities of the peaks as free parameters,

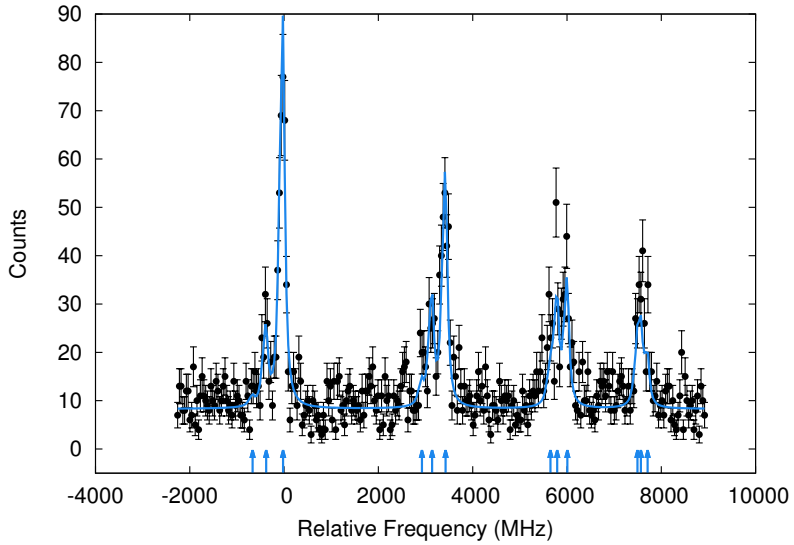

Figure 4.4: An example fit to one spectrum for ^{63}Mn. The frequencies are relative to the centre-of-gravity of ^{55}Mn. The arrows show the location of the hyperfine peaks.

left the extracted values unchanged within errors, demonstrating that the assumption of a single laser interaction per atom is valid. Fig. 4.4 shows an example of a fit to one of the spectra for ^{63}Mn, with the locations of the peaks marked by arrows.

Since the B value of the lower ($^6S_{5/2}$) state has been shown to be much less than 1 MHz [55], it has been constrained to zero in the analysis. The ratio $A(^6S_{5/2})/A(^6P_{3/2})$ was also constrained to be 0.0752 for all the unstable isotopes, the value determined by leaving both $A(^6S_{5/2})$ and $A(^6P_{3/2})$ as free parameters in the fit of the ^{55}Mn spectra. This ratio is common across any isotopic chain and was thus used to stabilize the fit of the other isotopes (see Ch. 2). The hyperfine anomaly was not considered at this level of accuracy.

4.3.1 CEC processes

During the fitting process, it was observed that the line shapes of the hyperfine peaks were slightly distorted with respect to the true symmetric shapes. As described in Sec. 3.5.1, this is a result of the variety of inelastic events that can occur inside the charge-exchange cell. Processes such as collisional excitation and non-resonant charge-exchange can result in the formation of some atoms in an excited state, with the excitation energy coming from the kinetic energy of the beam. When these atoms are excited then decay back to the atomic ground state, they have a lower velocity and thus require a higher acceleration voltage to return to the Doppler-shifted resonance frequency. Through this process, additional peaks are produced which are located at a slightly lower frequency, very close to the main resonance peak [77].

These non-resonant processes were taken into account in the fitting procedure by the inclusion of a second Lorentzian profile associated with each peak. Each of these secondary peaks was given a fixed *energy* offset determined through the simultaneous fit of the high-statistics ^{55}Mn data. The fitted *frequency* offset was determined to be $-78.6(11)$ MHz which corresponds to an energy of 4.6 eV. This indicates that the dominant non-resonant process is the excitation of atoms to the ^{6}P triplet at 4.4 eV [74]. The frequency offset for isotopes other than ^{55}Mn was determined by scaling the ^{55}Mn offset to the appropriate mass. The intensities of the secondary peaks were included in the fit as a fraction of the main peak height, and a common fraction was taken for all secondary peaks in one spectrum. The fitted values of the relative intensities indicate that the atoms affected by these inelastic processes during charge-exchange constitute approximately 20% of the total measured beam.

Though this double peak structure is not obvious to the eye in any particular

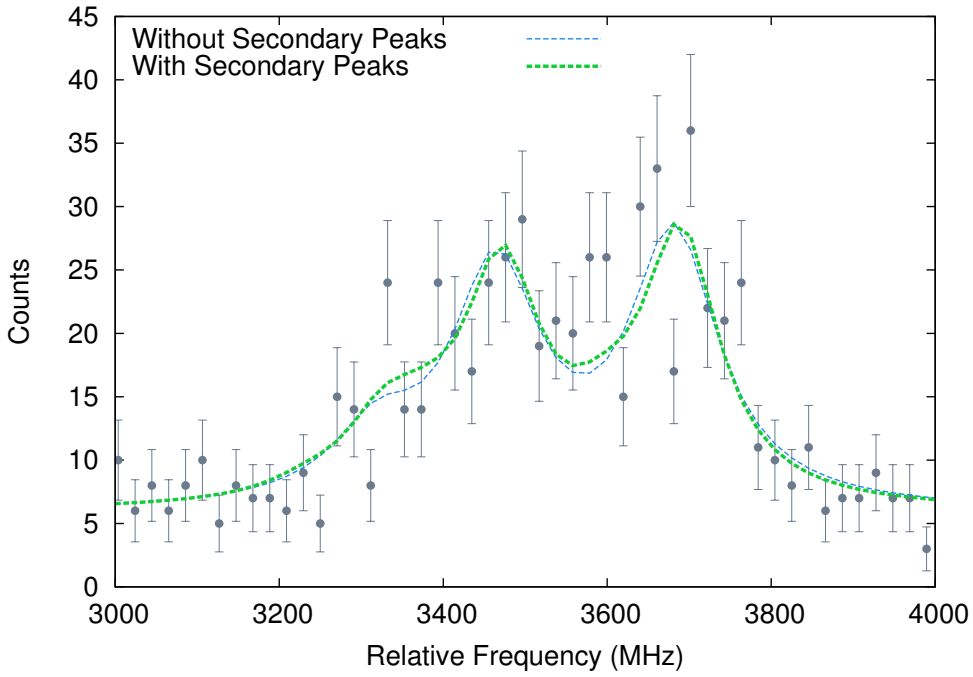

Figure 4.5: An example of the fit with and without secondary peaks included, shown for one multiplet of ^{55}Mn.

spectrum, it was found necessary to reproduce the literature value for the $A(^6S_{5/2})$ coefficient of ^{55}Mn. Davis et. al quotes a value for the lower state of the transition of $A(^6S_{5/2}) = -72.420836(15)$ MHz [55], however, when data from this experiment was fitted without the double peak structure, a value of $A(^6S_{5/2}) = -71.92(14)$ MHz was obtained. With the double peak structure, a value of $A(^6S_{5/2}) = -72.4(7)$ MHz is extracted, in good agreement with the literature value. Fig. 4.5 shows an example of the difference between the line shape with and without a secondary peak included.

Table 4.1: The measured nuclear spins, and A and B hyperfine coefficients for the $^6P_{3/2}$ excited state.

Isotope	Spin	A (MHz)	B (MHz)
^{51}Mn	5/2	-993.9(13)	17(8)
^{53}Mn	7/2	-997.1(10)	3(7)
^{55}Mn	5/2	-963.0(7)	13(2)
^{57}Mn	5/2	-967.4(9)	8(5)
^{59}Mn	5/2	-969.5(6)	8(6)
^{61}Mn	5/2	-981.6(6)	16(4)
^{63}Mn	5/2	-958.4(15)	11(13)

4.4 Results

4.4.1 Hyperfine Coefficients

Table 4.1 shows the hyperfine coefficients A and B of the transition's upper state. Literature values for the coefficients of the lower state of ^{55}Mn are $A(^6S_{5/2}) = -72.420836(15)$ MHz and $B(^6S_{5/2}) = -0.019031(17)$ MHz, obtained in spin-exchange optical pumping experiments [55]. Good agreement is shown between the $A(^6S_{5/2})$ value from this work ($A(^6S_{5/2}) = -72.4(7)$ MHz) and the literature value.

The A values have been used to calculate the magnetic moments of the isotopes using [5],

$$\mu = \mu_{\text{ref}} \frac{I\,A}{I_{\text{ref}}\,A_{\text{ref}}}$$

with the value of $\mu_{ref} = +3.46871790(9)$ for ^{55}Mn taken from [78]. The results of these calculations are shown in Tab. 4.2. Spectroscopy on the isotopes $^{50-56}$Mn has already been described and compiled elsewhere [55, 79, 80], and the reported magnetic moments for ^{51,53}Mn are in agreement with our results.

Table 4.2: The magnetic dipole moments, determined as described in Ch. 2 from the A and B values in Table 4.1. The value marked with * indicates the reference value taken from [78] with corrections for diamagnetic shielding. Values are compared to shell-model calculations using the GXPF1A and the LNPS effective interactions with free nuclear g-factors. All GXPF1A calculations have been done by Hanne Heylen (KU Leuven) and all LNPS calculations have been done by Silvia Lenzi (INFN).

Isotope	μ (μ_N)	μ (μ_N) [GXPF1A]	μ (μ_N) [LNPS]
^{51}Mn	+3.578(5)	+3.46	-
^{53}Mn	+5.025(5)	+4.76	-
^{55}Mn	+3.4687179(9)*	+3.35	-
^{57}Mn	+3.482(3)	+3.44	+3.60
^{59}Mn	+3.490(2)	+3.48	+3.56
^{61}Mn	+3.534(2)	+3.62	+3.56
^{63}Mn	+3.437(5)	+3.77	+3.48

4.4.2 Spins

An advantage of laser spectroscopy is the possibility of making an unambiguous determination of nuclear spins. The spins of all odd-even isotopes for $A = 51 - 63$ have been measured here by analyzing the pattern of the hyperfine structure peaks, as shown in Fig. 4.4.

Table 4.1 shows the spin values derived from the least-squares fit to the spectra. Where uncertainties existed, for example in the case of ^{61,63}Mn where the spins were only tentatively assigned, the correct spin was confirmed by the observation that the use of an alternative value for the spin in the fitting procedure produces a $B(^6P_{3/2})$ coefficient that is unphysically large (as mentioned earlier, $B(^6P_{3/2}) \approx 0\,\mathrm{MHz}$). For example, assuming $I = 7/2$ for ^{63}Mn gives $B(^6P_{3/2}) = -230(9)\,\mathrm{MHz}$ which would yield the unrealistically large quadrupole moment $Q_\mathrm{s} = -5.8(9)\,\mathrm{b}$. The same comparison can be done for the other isotopes and similarly large quadrupole moments

are calculated. The top part of Fig. 4.6 shows two fits to a spectrum of ^{63}Mn using spin 5/2 in one case and spin 7/2 in the other. In the bottom part of Fig. 4.6, quadrupole moments for the Fe, Mn and Cr isotopic chains are plotted alongside the values obtained for the quadrupole moments in this work assuming a spin 7/2 for ^{59,61,63}Mn. It can be seen that taking the incorrect spin (the correct spin is 5/2 for all three isotopes) produces quadrupole moments that deviate unrealistically from regional systematics, and indeed exceed any observed values of $Q_{\rm s}$ in any nuclei.

The spin data are somewhat surprising because in an independent particle shell-model interpretation, the odd manganese isotopes with 3 holes in the $\pi f_{7/2}$ shell would have a spin 7/2 ground state. However, except for ^{53}Mn (with 28 neutrons), all isotopes have been found to have spin 5/2. This result will be discussed in more detail in Sec. 4.5.

4.5 Discussion

Shell-model calculations of the energy levels and moments of neutron-rich isotopes in the region $Z = 20$ to $Z = 28$ have sought to characterize the rapid structural evolution and lack of a robust subshell closure near $N = 40$. Using the code ANTOINE [81] and the GXPF1A effective interaction [2], calculations of the magnetic moments of neutron-rich Mn have been performed in the pf model space, allowing up to eight particles (maximum 2 protons and 6 neutrons) to be excited from the $1f_{7/2}$ to the $2p_{3/2}$, $1f_{5/2}$ and $2p_{1/2}$ orbitals. In such shell model codes, a limit must be set on the number of possible excited particles based on computational constraints. For manganese, protons should occupy the $f_{7/2}$ orbital as a result of normal filling of the nuclear levels, however if no excitations are allowed, the ground state spin of ^{55}Mn

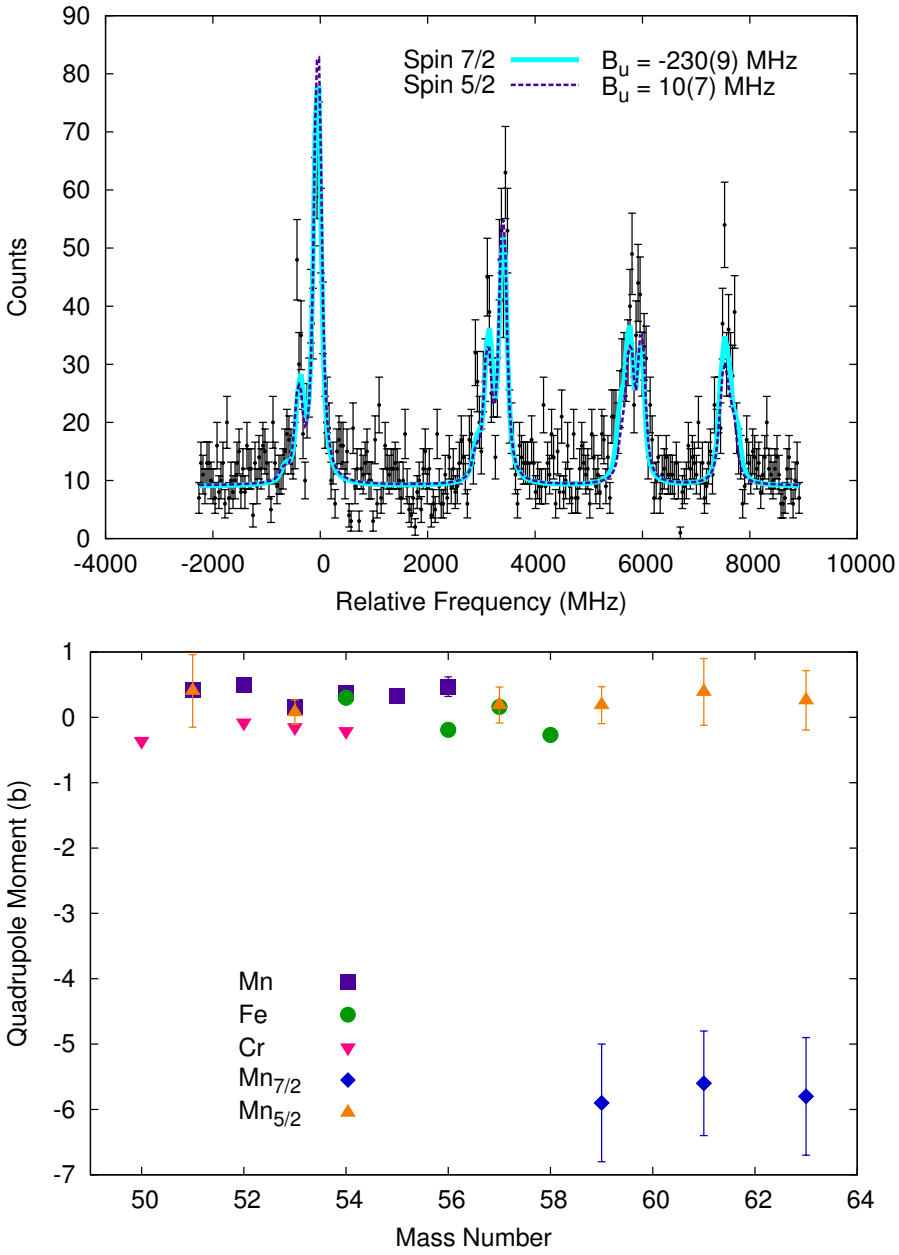

Figure 4.6: Top: Data for ^{63}Mn overlaid with the fit for spin 7/2 and spin 5/2. Bottom: Quadrupole moments for the Fe, Mn and Cr isotopic chains, plus the moments for ^{59,61,63}Mn derived using a value of $I = 7/2$. The data for Fe and Cr can be found in [79] (where the most recent value was taken if there were multiple entries), and the Mn data is taken from [80].

is incorrectly predicted to be 7/2. For the correct ground state spin of 5/2 to be predicted by GXPF1A, a minimum of two possible proton excitations are required. Ideally, a maximum number of neutron excitations should be permitted in order to accurately describe the role played by neutron excitation in the structure of Mn. In this case, computational limitations restricted the calculations to 6 possible neutron excitations. GXPF1A is a modification of the earlier GXPF1[1] interaction, however with proton excitations allowed, they agree on the g-factor value to within 0.6%.

Magnetic moments and their associated g-factors ($g = \mu_I / I\,\mu_N$) are highly sensitive to the nuclear wave function, and provide a stringent test of the models. Shell model results obtained with free g-factors are listed in Table 4.2 and a comparison of GXPF1A results to experimental values are shown in Fig. 4.7.

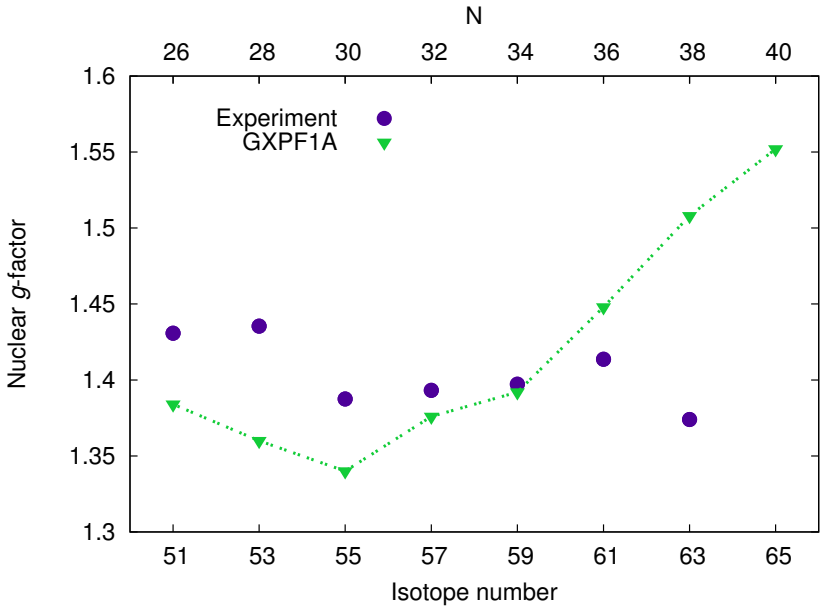

Figure 4.7: Comparison of experimental data from this study to calculations using the GXPF1A interaction. All calculations were performed with free g-factors. Error bars are within the symbols.

In this case, the use of free g-factors means that the values assigned to the spin (g_s)

Table 4.3: Comparison of the magnetic moments calculated using GXPF1A for $^{51-65}$Mn with free and effective g-factors. Values for the effective g-factors are given in Eq. 4.4. All GXPF1A calculations have been done by Hanne Heylen (KU Leuven).

Isotope	$\boldsymbol{\mu}$ **[Free]**	$\boldsymbol{\mu}$ **[Effect.]**
^{51}Mn	+3.46	+3.49
^{53}Mn	+4.76	+4.86
^{55}Mn	+3.35	+3.39
^{57}Mn	+3.44	+3.46
^{59}Mn	+3.48	+3.49
^{61}Mn	+3.62	+3.64
^{63}Mn	+3.77	+3.79
^{65}Mn	+3.88	+3.94

and orbital angular momentum (g_ℓ) g-factors are the values measured for unbound nucleons. These values are [82],

$$g_{\rm s}^{\pi} = 5.586 \qquad g_{\ell}^{\pi} = 1.0 \tag{4.2}$$

$$g_{\rm s}^{\nu} = -3.826 \qquad g_{\ell}^{\nu} = 0.0. \tag{4.3}$$

Calculations using the GXPF1A interaction do not reproduce the observed trend very well, but given the scale, the absolute values are reproduced within a 1-10% range up to ^{61}Mn. From $N = 36$ onwards, the GXPF1A calculations predict an increase in the g-factors towards the Schmidt value (Fig. 2.1, [53]), as would be expected if $N = 40$s were a magic number. Instead, the experimental data shows a decrease after $N = 36$. Using effective g-factors does not significantly improve the overall agreement. Table 4.3 lists values for the g-factors of each isotope using the effective spin and orbital angular momentum g-factors,

$$g_{\rm s}^{\pi} = 4.189 \qquad g_{\ell}^{\pi} = 1.1 \tag{4.4}$$

$$g_{\rm s}^{\nu} = -2.869 \qquad g_{\ell}^{\nu} = -0.1. \tag{4.5}$$

The widening discrepancy between the measured magnetic moments and the GXPF1A calculations suggests that the model space is insufficient to describe the structural changes in the heavier isotopes. If the $\nu 1g_{9/2}$ and $\nu 2d_{5/2}$ orbitals play a crucial role, as has been proposed to reproduce the level scheme of ^{66}Fe [7, 28] and in Cr [35], then the model space must be expanded. These orbitals are taken into account by the LNPS interaction, which, starting from a ^{48}Ca core, includes the entire pf shell for protons and the levels $1f_{5/2}$, $2p_{3/2}$, $2p_{1/2}$, $1g_{9/2}$ and $2d_{5/2}$ for neutrons [3]. Calculations done with this interaction reproduce very well the decreasing trend in the g-factors from ^{61}Mn ($N = 36$) onwards, as shown in Fig. 4.8. The calculated g-factors agree with the observed values for ^{61,63}Mn to within 1%. This confirms the importance of neutron excitations across $N = 40$ for isotopes with neutron numbers $N = 36$ and higher. For the sake of completeness, the results of LNPS calculations for the lighter Mn isotopes, using the full pf space with a ^{40}Ca core and blocking excitations to the $\nu 1g_{9/2}$ and $\nu 2d_{5/2}$ orbitals are also shown in Fig. 4.8. As expected, these results are similar to those of GXPF1A.

Since the observed magnetic moments of ^{57,59}Mn are better reproduced by the GXPF1A calculations, and the trend in the heavier isotopes can only be reproduced by the LNPS calculations, these results can be used to investigate changes in the ground state wavefunctions of odd-A Mn isotopes with increasing neutron number from ^{57}Mn ($N = 32$) onwards. Fig. 4.9 shows the predicted occupation of the relevant orbitals for the ground state wavefunction. The top panel shows the neutron occupation of orbitals past $N = 28$ as a function of neutron number (these are the neutron orbitals to which excitations are allowed in the LNPS calculations). For example, ^{65}Mn has 40 neutrons, with 12 neutrons in orbitals above $N = 28$. Fig. 4.9 shows

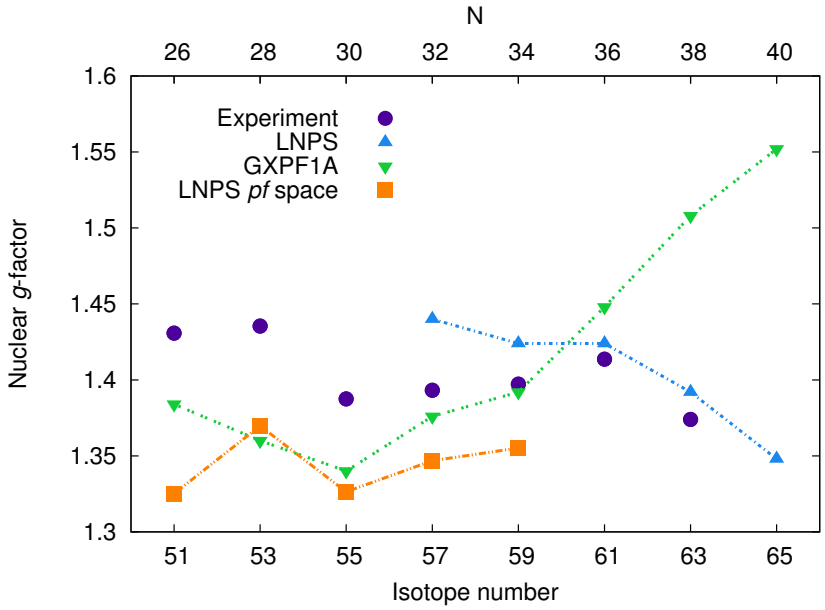

Figure 4.8: Comparison of experimental data from this study to calculations using the GXPF1A interaction, the LNPS interaction, and the LNPS interaction in the pf shell using a ^{40}Ca core and blocking excitations to the neutron $g_{9/2}$ and $d_{5/2}$ orbitals. All calculations were performed with free g-factors. Error bars are within the symbols.

8 of these neutrons in the pf orbitals and 4 in the $g_{9/2}d_{5/2}$ orbitals. The labels beside $N = 36, 38, 40$ indicate the dominant excitation modes for these wavefunctions, either 2 particle-2 hole, 4 particle-4 hole, or a combination of the two. Only an even number of particles can be excited past $N = 40$ because the parity of the orbitals changes between the pf shell and the $g_{9/2}d_{5/2}$ shell. Thus parity in the nucleus is only conserved when particles are promoted in pairs.

As expected, the level occupations calculated with LNPS show that additional neutrons are preferentially excited into the $1g_{9/2}$ orbital, with a marked augmentation of the $2d_{5/2}$ level occupation as well. The LNPS predicted ground state configuration for ^{65}Mn ($N = 40$) is dominated by 4p-4h neutron excitations, as is the case for Fe, Cr, Ti and Ca [3], indicating the strong contribution of these configurations to the

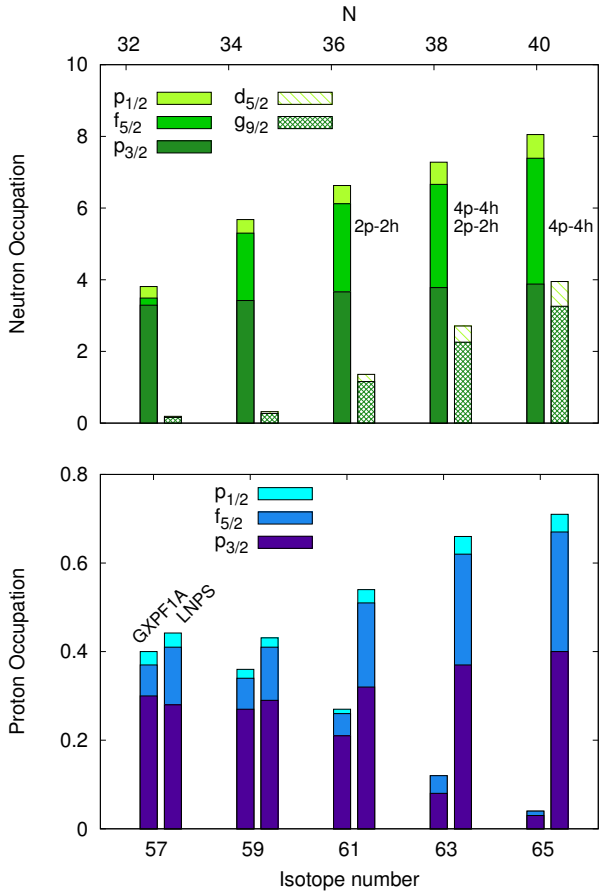

Figure 4.9: Top: Orbital occupation numbers for neutrons calculated using the LNPS interaction. Occupation levels are grouped into the pf group ($\nu p_{3/2}$, $\nu f_{5/2}$, $\nu p_{1/2}$) and the gd group ($\nu g_{9/2}$, $\nu d_{5/2}$). Bottom: Orbital occupation numbers for protons excited across $Z = 28$ calculated using the GXPF1A and LNPS interactions.

wavefunction.

The bottom panel of Fig. 4.9 shows the proton excitations from the $f_{7/2}$ orbital below $N = 28$ to the higher pf shell orbitals for both the GXPF1A and LNPS calculations. The numbers on the y-axis represent the average number of protons calculated to occupy each of the higher pf orbitals. Though these numbers seem small in comparison with the case of the neutrons, small admixtures of proton excitations can have a large effect on certain nuclear properties [83]. As can be seen in Fig. 4.9, the

LNPS calculation for ^{65}Mn shows that approximately 14% of the proton wavefunction is composed of excitations to the $p_{3/2}f_{5/2}p_{1/2}$ orbitals. This implies that, contrary to the simplest assumption of 5 protons residing in the $f_{7/2}$ orbital, ^{65}Mn has a mixed wavefunction, the properties of which are dominated by proton excitations within the pf shell.

A comparison between the proton level occupations predicted with the LNPS and GXPF1A interactions shows that LNPS predicts increasing numbers of proton excitations in the upper pf shell while GXPF1A predicts decreasing numbers, and far fewer excited protons in total, as one moves towards $N = 40$. The accuracy of the LNPS interaction in predicting the measured g-factors at higher neutron number, along with the predicted increase in proton excitations across $Z = 28$, suggest that proton excitations play a pivotal role in the structural evolution observed in this mass region. The removal of protons from the $f_{7/2}$ orbital as one moves away from ^{68}Ni induces a stronger binding of the orbits $\nu 1g_{9/2}$ and $\nu 2d_{5/2}$, allowing neutron promotion across $N = 40$. The promotion of these neutrons then results in a repulsive potential with the $\pi 1f_{7/2}$ orbital and an attractive potential with the $\pi 1f_{5/2}$ orbital, contributing to the reduction of the $Z = 28$ shell gap and thus enhancing the probability for the excitation of protons across it. A similar explanation has been put forth to describe the shell evolution seen in the $0^+_{1,2,3}$ states of ^{68}Ni, calculated using the advanced Monte Carlo shell-model [84], and to describe the level structure in neutron-rich Cu [37]. The resulting increase in deformation is reflected in the ground state spins, shown in Table 4.1, where spin 5/2 is favoured over the expected spin 7/2 [85, 33]. The ground state spins are correctly predicted to be 5/2 by both GXPF1A [8, 86] and LNPS, with the 7/2 states in ^{57,59,61,63}Mn at less than 300 keV for both interactions.

There are two abrupt decreases in the g-factors visible in Fig. 4.8, after $N = 28$ and after $N = 36$. The first discontinuity can be explained by the occupation of the higher νpf orbitals. This allows for more proton-neutron correlations, which influence the magnetic moment as protons are excited across the $Z = 28$ subshell gap. A similar effect was seen in Cu isotopes near $N = 28$ [14, 87]. The discontinuity between $N = 36$ and $N = 38$ is induced by the configuration mixing between the $f_{5/2}$ and the $f_{7/2}$ orbitals. A small off-diagonal matrix element, $\langle j_1||\mu||j_2\rangle$, can result in a sizeable correction to the magnetic dipole moment calculated with a pure $\pi 1f_{7/2}$ wavefunction. The off-diagonal elements will, in this case, be non-zero if the quantum numbers n and ℓ are equal for the two states j_1 and j_2, meaning that configuration mixing between spin-orbit partners $j_1 = \ell + 1/2$ and $j_2 = \ell - 1/2$ has a significant effect on the value of μ [83]. Thus the increased occupation of the $\pi 1f_{5/2}$ orbital from $N = 36$ onwards leads to small admixtures of the spin-orbit partner $\pi 1f_{5/2}$ into the wavefunction dominated by the $\pi 1f_{7/2}$ configuration, as discussed above, and this has a significant effect on the calculated magnetic moments.

As demonstrated, the magnetic moments are sensitive probes of the nuclear wave function and here they have provided the first evidence for the influence of neutron intruder orbitals on the ground states of isotopes with $N < 40$. However, the magnetic dipole moment is only indirectly sensitive to collectivity, whereas the electric quadrupole moment provides a direct probe of the quadrupole correlations between nucleons. Fig. 4.10 shows the GXPF1A and LNPS predictions for the quadrupole moments of Mn isotopes, in which the two predictions can be seen to deviate significantly starting at ^{61}Mn. This deviation can be attributed to increased correlations resulting from excitations across $N = 40$ and $Z = 28$, which are only included in the

LNPS calculation. In this region of the nuclear chart, where the onset of collectivity has been observed in Fe and Cr [7, 31], comparison of GXPF1A and LNPS predictions to the experimentally determined quadrupole moments will provide valuable information on the degree of collectivity in manganese isotopes.

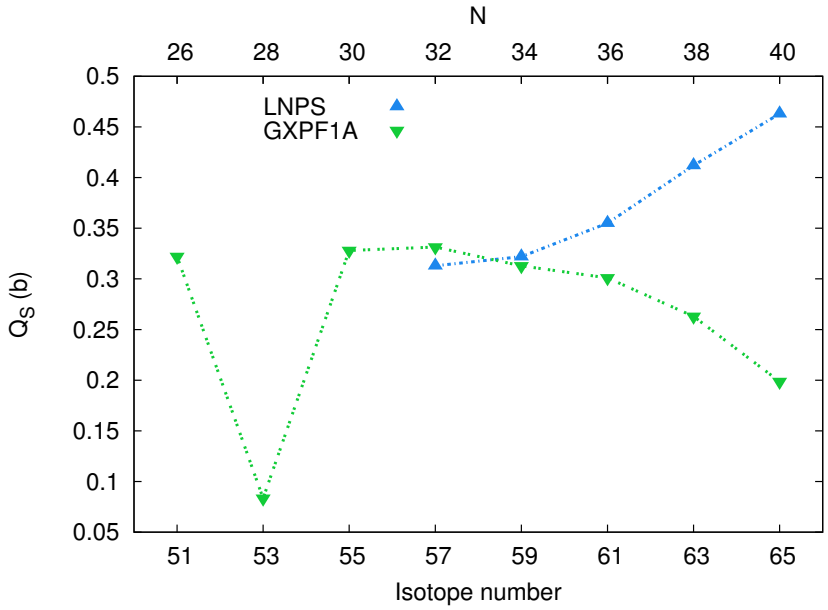

Figure 4.10: The electric quadrupole moments as predicted by the GXPF1A and LNPS effective interactions.

4.6 Need for Optical Pumping

Up to this point, only the results for the magnetic moments have been discussed, though both A and B hyperfine coefficients were measured for the transition in this experiment. However, as described earlier, the quadrupole splitting of the ground state is very weak ($B(^6S_{5/2}) \approx 0\,\mathrm{MHz}$) and as can be seen from the values in Table 4.2, the sensitivity to the quadrupole moment in the upper state is also very weak. This results in a large relative uncertainty on the value of $B(^6P_{3/2})$, making comparisons

to shell model calculations uninformative. For this reason, quadrupole moments have not been extracted. In the atom, all the transitions from the ground state have a similar insensitivity to the quadrupole splitting and thus are not suited to extract quadrupole moments.

There are accessible transitions in the ion, which, in principle, have the advantage of increased efficiency over the atom, since they do not suffer from the problem of populating a high density of states during the charge-exchange process. However, the transitions from the ground state in the ion are spectroscopically weak [74]. A suitable strong transition with sensitivity to the quadrupole moment exists from a metastable state [74], however the natural population of this state is too low to efficiently perform spectroscopy. If, however, this metastable state could be artificially populated, this transition could be used to extract quadrupole moments for the isotopes ^{53,55,57,59,61,63}Mn. In principle the increase in sensitivity should allow for the detection of hyperfine splitting for even more exotic Mn isotopes (but see Sec. 6.1 for details).

One method to achieve this is the use of optical pumping [88], whereby a laser is used to excite the ground state ions to a higher energy level from which they decay to populate the metastable state. The scheme to be used for manganese is shown in Fig. 4.11.

The ions are excited from the $^7S_3$ ground state to the $^5P_3$ state at $43\,370.51\,\mathrm{cm}^{-1}$. From here the ions decay with an Einstein A coefficient of 1.96×10^8 /s to the $^5S_2$ level at $9\,472.97\,\mathrm{cm}^{-1}$ [74], from which spectroscopy is performed. The transition from the metastable state to the ground state is forbidden [74], so as the ions decay from the unstable excited state, they accumulate in the metastable state, providing

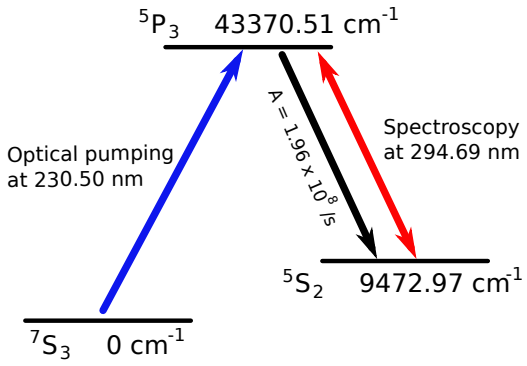

Figure 4.11: Optical pumping scheme used to excite trapped manganese ions from the ground state to a low-lying metastable state at 9 472.993 cm^{-1} via an intermediate excited state.

an increasing population for spectroscopy.

The laser wavelength required to excite manganese ions from the ground state ($^7S_3$) is 230 - 260 nm [74], a range difficult to produce in high-resolution, continuous-wave lasers. As an alternative, a broadband, pulsed laser can be used to pump the ground state ions to an excited state, however this results in lower efficiency since the laser is interacting with the ions for less time, and the power is spread out over a range of frequencies. This efficiency can be restored by optically pumping the ions while they are trapped, instead of while they are in-flight. ISCOOL provides a convenient location for this, since the ions can be trapped for up to several seconds in a nearly stationary state. Due to the long trapping time, multiple laser-ion interactions take place and thus high laser power is not required, nor is it necessary to use a continuous wave laser. Even though the transition is spectroscopically weak, the long interaction time in the cooler/buncher guarantees efficient excitation. The next chapter will discuss the details of how optical pumping was performed at ISOLDE.

Chapter 5

Radio Frequency Quadrupole Cooler and Buncher

The radio frequency quadrupole cooler and buncher (RFQCB) at ISOLDE, named ISCOOL, provides an important function to the HRS beamline. It cools the beam by reducing the random kinetic energy of the ions, as well as providing the option of ejecting the beam in bunches. With or without the bunching feature, ISCOOL can provide high quality beams to all the experiments at ISOLDE, and is thus an important part of the HRS beam line. ISCOOL is of particular importance to the COLLAPS experiment, which requires a low-emittance, bunched beam in order to increase sensitivity (see Sec. 3.5). It is also essential for any optical pumping experiments, since the efficiency of the optical pumping will be dependent on the extended interaction time inside ISCOOL. The first attempt at optical pumping in the cooler/buncher was not successful due to an internal misalignment, which had been long suspected. The confirmation of this problem led to a more thorough investigation of the various properties of the machine and the ways in which it could be improved. This chapter

presents some technical details about the RFQCB, as well as the work that has been done on it to make optical pumping at ISOLDE possible.

5.1 Emittance

One of ISCOOL's functions at ISOLDE is to improve beam quality by reducing the emittance of the beam, sometimes referred to as cooling the beam. In order to understand how ISCOOL can improve beam quality, it is therefore important to understand the concept of beam emittance. There are two categories of emittance - transverse and longitudinal.

The transverse emittance of the beam is a value that combines both the spatial extent of the beam and the divergence of the particles (which defines the spatial extent of the particles at a later time). Thus it is a measure of the dynamic quality of the beam, a much more useful measure than just a snapshot of the beam at a particular moment. Different applications may require different spatial configurations and angular divergence of beam particles, however for transport through an accelerator, a beam with a small spatial and angular spread is preferable. Normally the total 2D transverse emittance would have to be considered, however if motion in the x and y directions can be considered independent (as is often the case in accelerators), we can calculate the emittance in each coordinate seperately.

The transverse emittance can be understood by plotting the locus of points $(u,\dot{u})$ for the particles in the beam, as illustrated in Fig. 5.1. Here, u is either the x or y spatial coordinate and $\dot{u} = p_u/p$ is the corresponding angular divergence of the beam, with p as the momentum. The $(u,\dot{u})$ space is called phase space and coordinates for particles in a well-formed beam will map out an ellipse in phase space. We can then

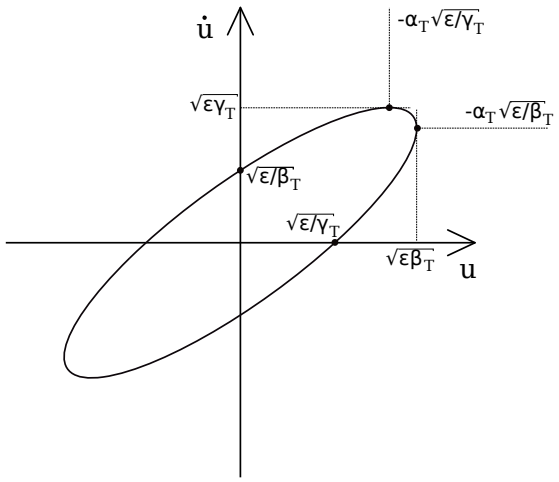

Figure 5.1: An ellipse in phase-space defined by the position u and angular divergence $\dot{u}$ of all the particles in the beam. The area of the ellipse is the emittance ϵ of the beam, which can be written in terms of the Twiss Parameters ϵ, α_{T}, β_{T}, and γ_{T}.

define the emittance as the area of this phase-space ellipse divided by π,

$$\epsilon = \Delta u\,[\mathrm{mm}] \times \Delta \dot{u}\,[\mathrm{mrad}] \tag{5.1}$$

where Δu is half the spatial extent of the beam and $\Delta \dot{u}$ is half the angular divergence [89].

This ellipse is more accurately described by the Twiss parameters, ϵ, α_{T}, β_{T}, and γ_{T}, as shown in Fig. 5.1. The Twiss parameters will be useful later in characterizing the motion of the beam through electrostatic elements. The emittance can now be written as [90],

$$\epsilon = \gamma_{\mathrm{T}} u^2 + 2\alpha_{\mathrm{T}} u\dot{u} + \beta_{\mathrm{T}} \dot{u}^2. \tag{5.2}$$

In practice, the edge of the beam is not a hard boundary and so when measuring or calculating the emittance, one often takes the 90% emittance, that is the ellipse enclosing 90% of the beam particles.

Emittance in the longitudinal direction is also relevant for bunched beams, where it is a measure of the energy and temporal spread of the bunch. As with the transverse emittance, it can be defined as the area of an ellipse in a phase space with coordinates ΔE and Δt, divided by π,

$$\epsilon_{\text{long.}} = \Delta E\,[\text{eV}] \times \Delta t\,[\mu\text{s}] \tag{5.3}$$

where ΔE is the energy spread and Δt is the pulse width.

An important feature of the emittance is that it obeys Liouville's Theorem, which states that, under conservative forces, volumes in phase-space are constant [91]. This implies that the emittance of the beam (the area in 2D phase-space, since the x, y and z directions are decoupled) does not change as it travels through the accelerator, though the shape of the distribution may change [89]. This will become important during the discussion of the ways in which ISCOOL improves the emittance of the HRS beam.

5.2 Mechanical Design of ISCOOL

ISCOOL [63] is a helium-filled cylindrical Paul trap [90] constructed of four 800 mm long rods which carry the RF voltage, and which support the 25 axial electrodes (separated by ring-shaped ceramic insulators) that make up the body of the cylinder. The top frame in Fig. 5.2 shows two of the four RF rods attached to the end plates of the cylinder, while the bottom frame shows the fully built RFQCB cylinder with the 25 axial electrodes visible (the RF rods are inside the cylinder).

A cross-sectional view of a model RFQCB is shown in Fig. 5.3. The shape of the axial electrodes was chosen to minimize the necessary applied voltage - the fins

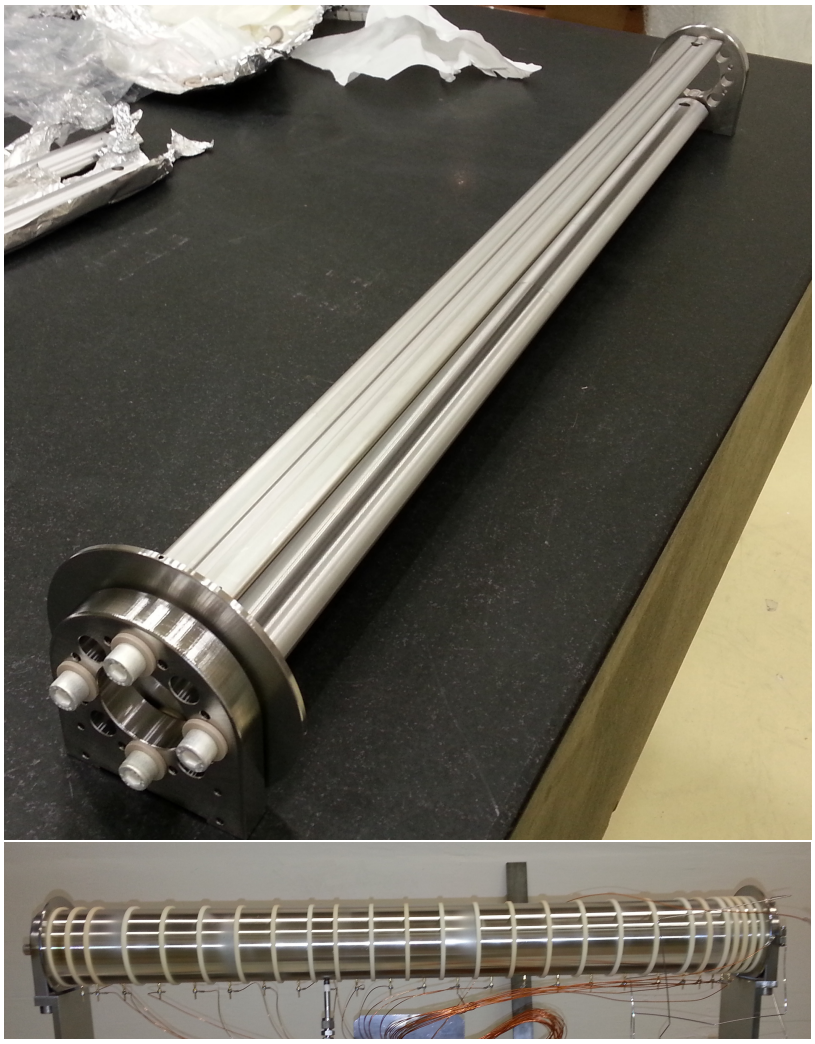

Figure 5.2: Top: The end plates of the RFQCB cylinder, with two of the four quadrupole rods attached, before putting on the axial electrodes. Bottom: The completed cylinder with only the axial electrodes and the lighter-coloured ceramic ring insulators visible.

Figure 5.3: Cross-sectional view of the RFQCB cylinder showing the profiles of the four hyperbolic RF rods and the shape of the axial electrodes. The lighter gray rectangles show the insulating bars.

extend inwards in order to increase the magnitude of the electric field on the central axis without the need to apply very high voltages to the electrode itself. The four RF rods have hyperbolic profiles and are insulated from the axial electrodes they support by thin ceramic bars. This allows the field created by the axial electrodes and the RF field to be controlled independently.

Outside of the RFQCB cylinder are the injection and extraction electrodes, responsible for maintaining the quality of the beam as it is decelerated and re-accelerated by the high voltage on which the machine is floated (see Sec. 3.3 for a brief discussion of the ISCOOL HV). The voltages on the electrodes take on increasing values between the ground potential and that of the high voltage in order to slow the ions down sequentially. Fig. 5.4 shows the layout of these electrodes. Detailed information about all the design features of ISCOOL can be found in [92].

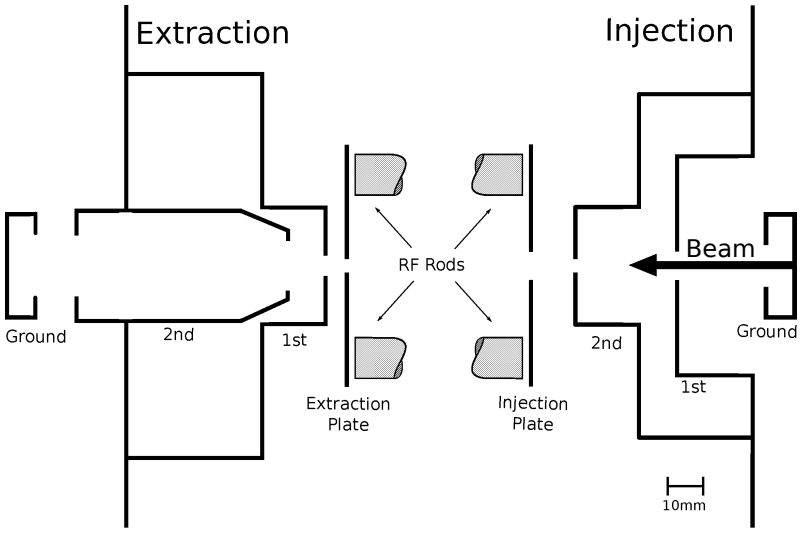

Figure 5.4: Schematic of the injection and extraction external electrodes, shown to scale, with the truncated cylinder of the RFQCB in the middle.

5.3 RFQCB Components

ISCOOL is used to cool the beam coming from the HRS by reducing its emittance, and it is used to bunch the beam by trapping it for a time in a potential well created by a longitudinal electric field. These two functions can be accomplished using three basic elements: the transverse radio frequency quadrupole field which is applied to the four RF rods, the DC longitudinal electric field which is applied to the axial electrodes and the buffer gas cooling of the beam by the injected helium gas.

5.3.1 The Radio Frequency Field

The voltage which produces the radio frequency field is applied by an oscillator and amplifier to the four long rods which run down the length of the RFQCB cylinder (see Fig. 5.2). They are powered such that each pair of opposite rods has the same

polarity (either +V or −V where V is the maximum voltage applied), and the polarity is switched at a frequency on the order of kilohertz. Switching the field in this way allows focussing in both transverse directions. To understand this, consider a static quadrupole field. This can be used to reduce the size of the beam in one transverse direction only - in one direction the ions will move away from the positively charged rods, and towards the central axis, while in the perpendicular direction they will move towards the negatively charged rods and away from the axis. By alternating the polarity of the quadrupole at high frequency, the ions can be pushed towards the axis in both the x and y directions, and thus the quadrupole field serves to confine the ions to an area near the central axis of the machine.

Mathematically, the motion of the ions in this alternating quadrupole field is governed by a special case of the Hill equation, known as the Mathieu equation. The derivation and solution of this equation can be found in Appendix A. It is important to note that the solutions to the equation of motion are stable in some cases and unstable in others, and whether or not they are stable is completely defined by the machine parameters (i.e. not dependent on initial conditions). Thus, based on the geometry of the machine, the voltage and frequency should be selected to produce stable ion trajectories.

5.3.2 The Axial Field

In the case of ISCOOL, the DC axial field is completely decoupled from the RF field since the RF voltage is applied to the four long rods while the axial potential is created by applying an independent voltage to each of the 25 axial electrodes. In this way, an axial electric field of any shape can be created. When ISCOOL operates in

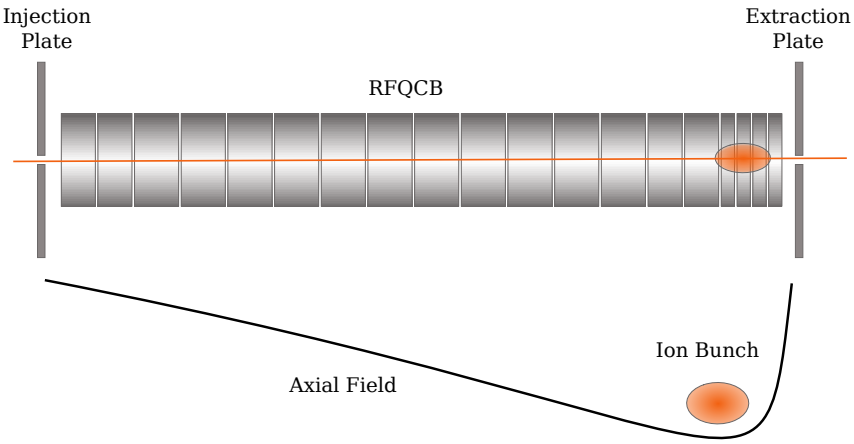

Figure 5.5: The longitudinal potential applied to the axial electrodes to create a potential well in which to form bunches.

continuous mode, it reduces the emittance of the beam but does not bunch it. The voltages on the axial electrodes are generally set to zero or a shallow slope and there is little effect from the axial field. In bunching mode, an axial field with a potential well near the extraction of the RFQCB is created, allowing the ions to be collected and then released as a bunch. Fig. 5.5 shows this configuration. The ions enter the RFQCB after being decelerated by the injection electrodes, and they encounter the negative slope of the axial electric field, which pulls them (since they are positively charged) towards the potential well at the end of the machine. They are collected in this potential well which is closed by putting a voltage higher than the energy of the ions on the final electrode (called the extraction plate, see Fig. 5.4). The bunch can then be ejected by lowering the voltage on the extraction plate, after which the ions are re-accelerated to their original energy by the voltage drop across the extraction electrodes.

5.3.3 The Buffer Gas Cooling

The buffer gas (in our case, ultrapure helium) is injected into the RFQCB cylinder in which the beam travels. The role of this gas is to lower the emittance of the beam by reducing the transverse motion of the ions, effectively damping their oscillations through multiple collisions. Thus some of the energy carried by the beam is transferred to the gas. Naturally the forward momentum of the beam in the longitudinal direction will also decrease, however the longitudinal electric field described in Sec. 5.3.2 will continue to pull the ions down the axis of the machine, thus they will not be lost. The ion-gas collisions are a non-conservative process and thus the buffer gas is the only element of the three RFQCB components that has the ability to change the emittance of the beam.

The action of the buffer gas can be analysed using two different methods - either the macroscopic approach is applied in which the gas is treated as a viscous drag on the motion of the ions, or the microscopic approach is applied in which we treat each ion-gas collision individually. The macroscopic approach has the advantage that it can be solved analytically if we consider only the large-amplitude motion of the ions, and this allows a solution to be derived and analysis to be performed without the need to consider the individual trajectories of the ions. However, it is not possible to account for effects such as stochastic processes and RF heating by treating the gas as a viscous drag force. This makes the macroscopic approach appropriate for some analysis, but unable to provide a complete picture. For this reason we will focus on the microscopic approach, however see [93] for a derivation and use of the viscous drag model.

In the microscopic approach, the trajectory of each ion is followed by considering a

series of drifts and collisions. The ion drifts for the length of one mean free path, then experiences a collision with a gas molecule which modifies its velocity, after which it drifts again. In order to avoid the complexity of the solutions to the Mathieu equation, which describe the motion of the ion in the RFQCB, we can use matrix methods and the Twiss Parameters introduced in Sec. 5.1 to track the evolution of the ion motion. A simulation using this method will be described in Sec. 5.4.

5.4 Ion Trajectory Simulation

In Sec. 5.3, the three major components governing ion motion in the RFQCB were discussed (RF field, axial field, buffer gas). A closer look at ISCOOL for the purposes of optical pumping, plus the impending upgrades for the HIE-ISOLDE project [59], motivated a more thorough investigation into the dynamics inside the cooler/buncher. Some measurements were made during the commissioning of the machine [63, 94] however there are many crucial properties, such as the effects of buffer gas pressure, injection/extraction dynamics, bunching efficiency/width and transmission efficiency under various circumstances which have not been studied. To understand how many of these parameters acting together can influence the trajectories of the ions, a simulation was written which tracks ions through ISCOOL, taking into account the RF field, the buffer gas and the longitudinal electric field.

The simulation is initiated by defining a series of general input parameters which apply to all ions. These parameters and their values for a typical simulation are listed in Table 5.1. These are nominal parameters, so may not be actual operating parameters for the machine.

Next the initial conditions of the ions must be defined. The default transverse

RF Peak Volt.	400 V
RF Freq.	0.35 MHz
Axial Field	32 V/m
Inj. Energy	200 eV
Pressure	0.1 mbar
Temp.	20 °C
Ion Mass	Hg 200u
Initial RF Phase	$\pi/5$
Radius of RFQ	0.02 m

Table 5.1: RFQCB nominal operational parameters used in the simulations.

spatial distribution for the ions is Gaussian, however an input file can be used to define the incoming velocity and position of each ion individually. An appropriate input file could be created with software such as CST Microwave Studio[1], which has implemented particle tracking through electromagnetic components. This would allow the passage of ions through the injection electrodes to be simulated and a file to be output containing the positions and velocities of the ions as they are injected into the RFQCB cylinder.

Once the initial conditions have been defined, the simulation calculates the effects of each of the three active forces (buffer gas, axial acceleration and RF quadrupolar field) on each ion. The simulation follows a drift-collision-drift method, in which the ion moves under the combined influence of the quadrupole field and axial electric field (the drift component) until colliding with a gas molecule (the collision component) and then resuming the drift component with altered speed and direction. Thus during the drift component, the ion's transverse motion is modified by the quadrupolar field, and its longitudinal motion is modified by the force of the axial electric field.

The effect of the axial electric field is simple to implement - during the drift

[1]CST STUDIO SUITE TM, Release Version 2012.08 - Jan 25 2013, Help System

component of the simulation, the longitudinal velocity of the ion is increased based on the electric field input value. The transverse motion, governed by the RF field, is more difficult to put into effect because the equations governing the motion of ions in a radio frequency quadrupole field are complicated to solve analytically. Thus, an approach based on matrix methods was adopted, using the known formulae for the passage of an ion through a static quadrupole lens. The method used here is to calculate the transverse motion of an ion in the sinusoidally-varying, quadrupolar field by approximating the 800 mm length of the RFQCB as a series of static, very short quadrupoles, each with constant strength which differs (sinusoidally) from the neighbouring quadrupoles. Thus if the first quadrupole has a strength equivalent to zero RF voltage (RF phase 0°), the second quadrupole would have a strength equivalent to the amplitude of the sinusoidal RF curve at some later phase (θ°), and the third quadrupole would have a strength equivalent to the amplitude of the sinusoidal curve at 2θ°, and so on. The phase advance with each quadrupole, θ, can be chosen randomly as long as it is small enough to accurately represent a continuously varying sinusoidal field; $\theta = \pi/200$ provides reasonable accuracy. The advantage to this approach is that there is an easy way to map the phase space coordinates of an ion from one side of a static quadrupole to the other, using a quadrupole transfer matrix. Thus the entire length of the oscillating RFQCB can be modelled by multiplying together the appropriate number of quadrupole transfer matrices for static quadrupoles whose strengths vary with the phase of the oscillating RF voltage. The method of transfer matrices is explained more thoroughly in Appendix B.

The length of the drift between collisions is equal to the mean free path of the ion in He gas, given some specified buffer gas pressure. The formula for the mean free

path of an ion through He atoms in thermal equilibrium is [95],

$$l = \frac{k_{\mathrm{B}}T}{\sqrt{2}\pi(r_{\mathrm{gas}} + r_{\mathrm{ion}})^2 P} \tag{5.4}$$

where T is temperature, P is pressure, k_{B} is the Boltzmann constant, r_{gas} is the radius of the gas atom (in our case $r_{\mathrm{He}} = 31\,\mathrm{pm}$ [96]) and r_{ion} is the radius of the ion (mercury ions were used in the simulation, with $r_{\mathrm{Hg}} = 150\,\mathrm{pm}$ [97]). With typical values for pressure and temperature, this gives a mean free path of around $l = 2.8\,\mathrm{mm}$.

After drifting for one mean free path, the ion experiences an elastic collision with a gas atom. The gas atoms are not tracked, but are created when required at the position of the ion from a Maxwell-Boltzmann velocity distribution. Conservation of momentum and kinetic energy dictate the change in velocity of the ion with each collision,

$$v_{\mathrm{final}} = \frac{M - m}{M + m} v_{\mathrm{ion}} + \frac{2m}{M + m} v_{\mathrm{gas}} \tag{5.5}$$

where M is the mass of the ion, m is the mass of the gas atom and v is the velocity. After the collision, the process repeats until the ion reaches the end of the machine (at $z = 800\,\mathrm{mm}$) or its transverse position exceeds the spacing between the quadrupole rods ($r = 20\,\mathrm{mm}$ in this case) at which point the ion is considered as lost on one of the surrounding surfaces.

Older simulations of ion motion in RF fields exist (see for example [98, 93]), however because of the quick progress of computational power, it is difficult to compare them to modern simulations. A slightly more recent simulation, using the ion optics code SIMION [99], is described in [100]. The script described in this work is similar to that in [100] in that they both include the effects of the buffer gas as individual elastic collisions with ions modelled as hard spheres, as opposed to modelling the

buffer gas using a viscous drag model, which is computationally easier but less accurate in these regions of low pressure. In the viscous drag model, the drag force on the ion is determined based on a mobility parameter, which should be measured experimentally however data for energies above 10 eV is difficult to come by [101]. The simulations compared here include the effects of the RF field on ion motion, however, the SIMION simulation calculates the electric fields of the structure based on the applied voltages, a method more difficult and time consuming than the method of quadrupole transfer matrices used here. The matrix method also allows an analysis of the results based on phase space considerations, which is a more natural system for accelerator dynamics. The script described here includes the effect of the longitudinal electric field, which is not included in the SIMION simulations. In addition, the code described here uses the mean free path of a particle in a gas to determine the collision frequency, instead of the ion mobility calculations used in the SIMION script, which have certain constraints [101]. This script was designed to be extensively modifiable - it has been used to simulate the inclusion of different pressure regions within the RFQCB chamber (see Ch. 8) and different types of longitudinal fields. The level of accuracy can be increased or decreased as the situation requires and all the properties of an ion can be read out at any point during its trajectory.

There are also some limitations to the usefulness of this simulation. It models only the interior of the RFQCB cylinder and thus does not include the effects of the injection and extraction electrodes. These parts of the machine are better simulated using finite-element codes, such as CST Microwave Studio. The effect of space charge limitations on the ions has also not been taken into account, though this does not play a large role under normal operating conditions and it would be relatively simple

to add in an approximation for this. As mentioned above, the collisions between ions and gas atoms are assumed to be hard-sphere, elastic collisions. This is a reasonable approximation, however it would be possible to modify this part of the code to include more accurate interaction potentials if more accuracy was desired. Finally, the simulation only calculates one transverse direction, based on the symmetry of the machine. This is correct as long as the machine is free of mechanical imperfections that break the independence of the forces in the x and y directions. However, including these sorts of effects is complicated in any simulation and difficult to quantify in the lab, and thus has been left out of the described simulation.

The first application of these simulations was to test the theory that the He pressure inside ISCOOL was too low to completely cool the ions. The flow of gas in and out of the machine, and the pressure inside the RFQCB cylinder are all unknown quantities, though the gas pressure is an important factor in the production of a high quality beam. The internal pressure should be high enough to cool the beam effectively but not so high that the pressure in the adjoining areas (injection and extraction electrode regions) increases or the beam interacts too frequently with the gas during the time that it is bunched, both of which will negatively impact the quality of the beam by increasing its emittance. Fig. 5.6 shows a simulation of ion trajectories through the RFQCB cylinder with two different pressures, while Fig. 5.7 shows the emittance of a beam as a function of pressure.

The simulation was done for Hg 1+ ions with an incoming energy of 200 eV and an initial emittance around 50 π mm mrad (a worst-case scenario). These were determined based on a simulation of the machine which did not include the effect of the pressure outside the cylinder, or the effect of RF heating within the cylinder. The

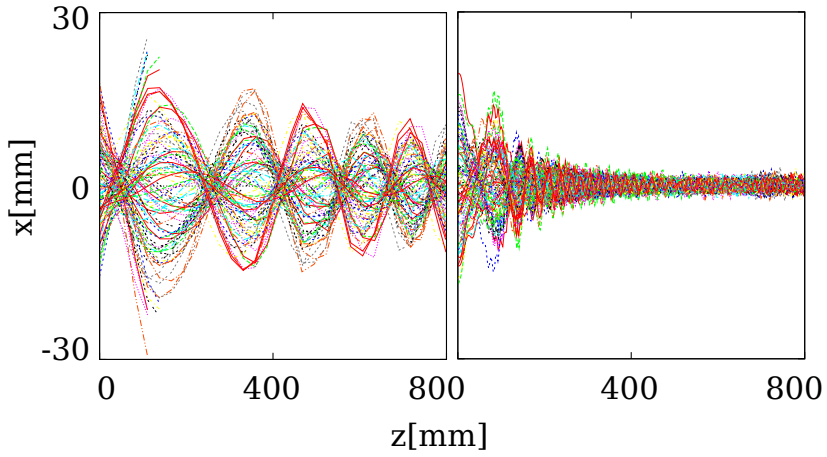

Figure 5.6: The left figure shows the beam profile in the 800 mm of the RFQCB for a helium pressure of 0.01 mbar. The right figure shows the same thing but for a pressure of 0.1 mbar, the nominal ISCOOL pressure.

poor beam properties are evident in the low pressure case, and the in-trap losses are around 15%. At pressures near 0.1 mbar, the transmission through the quadrupole structure is nearly always 100%. It can be seen that the lowest emittance occurs around a pressure of 0.1 mbar, and this number has been confirmed in other studies - see for instance [92].

The ISCOOL pressure should be 0.1 mbar, however, the actual pressure inside the chamber is unknown. Evidence based on instances of poor transmission and crude measurements of the exit energy of ions indicate that it is likely the pressure is closer to 0.01 mbar than to 0.1 mbar. While the pressure inside the chamber is likely too low to completely cool the ions, the increase in He flow is limited by the need to avoid beamline contamination. If the differential pumping system is not functioning effectively, it means that there is gas collecting in the regions of the extraction and injection electrodes. This would result in decreased beam quality and poor injection efficiency.

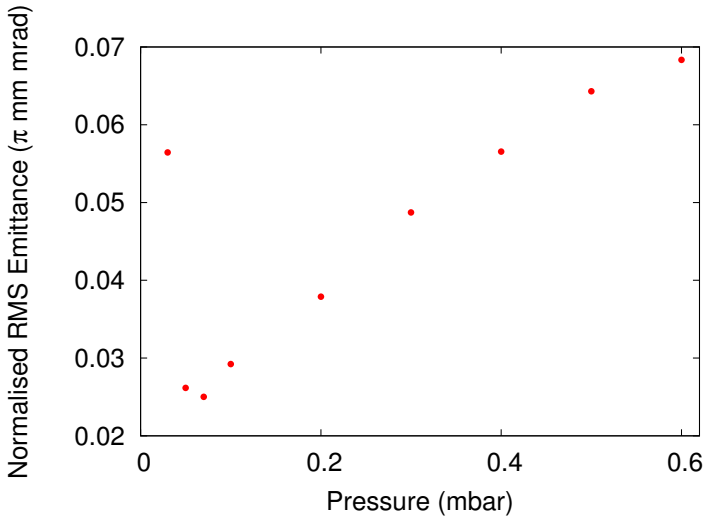

Figure 5.7: RMS normalised emittance (normalised to 60 keV, the re-acceleration energy) as a function of pressure, calculated based on data from the described simulation.

Benchmarking simulations of the ISCOOL vacuum using the code MOLFLOW+ [102] were done to identify the gas pressure in the regions near extraction and injection. These areas are small spaces between electrodes without sufficient passages for helium to escape and with direct feeding of helium via the differential pumping apertures in the injection and extraction plates (see Fig. 5.4). Preliminary results show a pressure near injection and extraction elevated by nearly one order of magnitude with respect to the beamline [103], motivating some changes to the RFQCB design which will be discussed in Ch. 8.

Low He pressure also has consequences for laser spectroscopy experiments. An imperfect cooling process detracts from the advantages gained by using an RFQCB since less cooling will produce a beam with higher longitudinal and transverse emittance. The higher longitudinal emittance implies a larger energy spread and so the observed resonance peaks will have more Gaussian broadening. The larger transverse

emittance implies a wider ion beam and thus the need for higher laser power with the same power density in order to probe the ions. This will result in more randomly scattered photons and higher background counts, or the necessity of focussing the beam strongly near the interaction region, which would result in skewed resonances.

5.5 Optical Pumping with ISCOOL

As outlined in Sec. 4.6, the insensitivity of the ground state transitions to quadrupole splitting in atomic manganese suggested the need for an alternative spectroscopy scheme. A suitable transition, with sensitivity to the quadrupole moment, exists in the ion [80] and unlike the atomic case, the population will not be spread over a range of states during the charge exchange process. The transition involves spectroscopy from a metastable state, the population of which can be enhanced by the use of optical pumping. In order to improve the efficiency of the optical pumping in the described experiment, the bunching capabilities of ISCOOL could be used to provide an interaction region in which the laser and ions would be overlapped for an extended period of time. This would allow multiple laser-ion interactions, meaning that a larger portion of the beam would be pumped to the excited state, compared to an in-flight setup in which the laser and fully-accelerated ions only interact while traversing a section of beam pipe. As an example, a beam of ^{88}Sr at 60 keV would take only 2.76 μs to traverse a one metre length of beam pipe (the length of the optical pumping region used in [104], for example), whereas the same beam could be trapped in ISCOOL for several seconds, if desired. To counteract the natural low-efficiency of the ground state transition in manganese ions, pumping in ISCOOL was a necessity.

The optical pumping setup at ISOLDE is as follows: the laser originates in the

RILIS cabin, passes through a quartz window on the back of the second separator magnet, then follows the beam line for approximately two metres before entering ISCOOL from the injection side. This path is shown in Fig. 5.8.

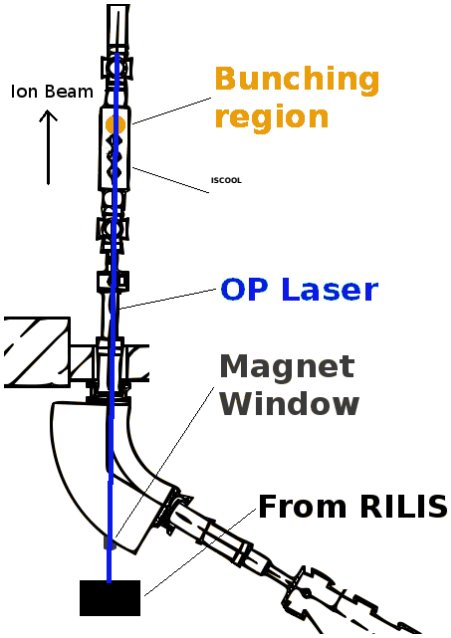

Figure 5.8: The path of the laser (green) from the RILIS cabin to the bunching region of the RFQCB. The black box represents an enclosed tube in which the laser travels from the RILIS cabin (located on the floor above) to the separator magnet room.

Since this was the first attempt to send RILIS lasers on this path, it was not clear exactly where the beam should be focussed. During normal RILIS operation, three laser beams are sent to the target system of either the HRS or the GPS and must be focussed precisely into the ion source. Since the ion source is not visible during operation, this focussing is accomplished by picking off a part of the beam along its trajectory and sending it back to the RILIS cabin along a path of length exactly equal to the distance to the ion source. This provides a secondary beam in the RILIS cabin that has travelled the exact same path length as the primary beam entering

the ion source, and thus if the beam appears well focussed inside the RILIS cabin, it is well focussed inside the ion source. A similar approach was used to focus the optical pumping beam into the RFQCB, however the exact distance to the injection apertures of the RFQCB is unknown and was therefore estimated to be approximately the same as to the ion source. This means that the position of the beam waist was not well known, and so fine tuning was done by hand to optimize the focus.

The design of ISCOOL also posed a challenge to the setup for optical pumping. Because the RFQCB cylinder is full of helium gas, there are a series of small apertures in the injection and extraction electrodes located on either end, designed to allow the beam to pass while producing a differential pumping effect on the helium. The geometry of these injection and extraction electrodes can be seen in Fig. 5.4. The injection side is composed of three electrodes with small apertures, plus the ground electrode which is a tube of 28 mm in diameter. The smallest of the three apertures is 4 mm in diameter, and thus this is the tightest constraint to the entry of the laser. Since these apertures are in close proximity to one another, any misalignment between them has a significant effect on the ability of a beam to pass through them without clipping. These electrodes, as well as those on the extraction side, were in fact misaligned and this interfered with the use of optical pumping at ISOLDE, as well as causing problems with the transmission of the ion beam through the RFQCB. Attempts to pass a RILIS laser into the bunching region of the RFQCB with this misalignment present were not successful, thus the misalignment had to be remedied in order to continue with the optical pumping of manganese.

5.5.1 ISCOOL Re-Alignment

During the successful career of ISCOOL, certain problems have been encountered that can be traced back to an internal misalignment of the multiple electrodes that make up the injection and extraction systems of the machine. Since the first and second electrodes (as labelled in Fig. 5.9) for both the injection and extraction side are fixed to each other, and then mounted on the inside of the vacuum chamber, while the cylinder of the RFQCB is mounted to the cover of the vacuum chamber, there is no guarantee that they are adequately aligned. The problem lies in the multiple components (many of them welded) found between the first and last electrode. This produces an accumulation of error, so it is difficult to ensure the alignment of the electrodes even though the cover has alignment pins to confirm that it is well placed. If we treat the first and second electrodes as a whole (they are bolted together), then the problem becomes the alignment of this electrode group, on either the injection or extraction side, to the (injection or extraction) plate.

The misalignment of ISCOOL was first diagnosed via the observation that extreme beam steering was required in order to transmit any beam. The steering was so severe that the beam missed the faraday cup at the exit of the machine entirely. ISCOOL was also visibly misaligned with respect to the beam line - it could be seen that the bellows on the injection side were stretched to their limit.

To begin the process of alignment, the deviation between the plate electrode (fixed to the cover) and the electrode group (fixed to the vacuum tank) was measured. Fig. 5.10 shows the result of this measurement.

In total, it was shown that while the first and second electrodes are well aligned, the alignment of these electrodes to the plate at the entrance/exit of the RFQCB was

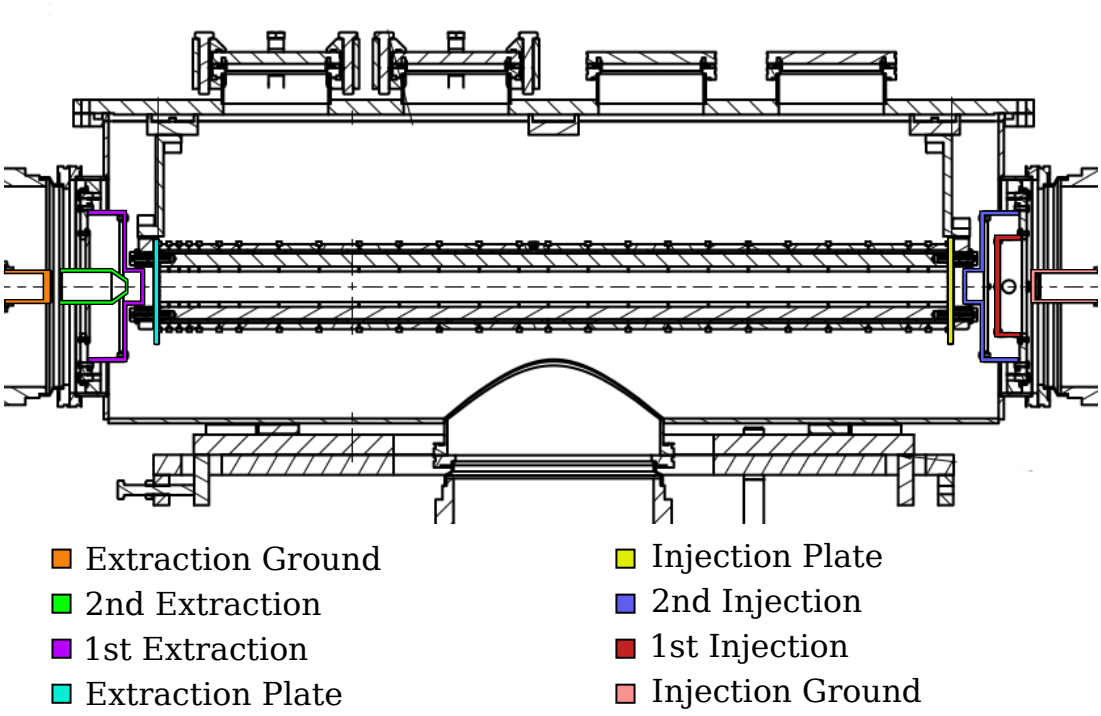

Figure 5.9: Mechanical drawing of ISCOOL with the injection and extraction electrodes colour-coded.

off by 0.75 mm. In order to fix this problem, the system supporting the RFQCB cylinder was modified to create supports that were horizontally and vertically adjustable (no adjustment in the position along the axis of the cylinder was necessary). Fig. 5.11 shows the changes made. An adapter piece was added with two screws pushing on either side of the RFQCB support piece (for horizontal movement) and the two nuts holding the support up are adjusted to provide vertical movement.

Alignment Method and Results

The method used to align the apertures was to take a high resolution photograph (using a Canon EOS 5D Mark III on a Manfrotto adjustable tripod) of the injection or extraction plate, then compare it with a photograph taken from the same spot

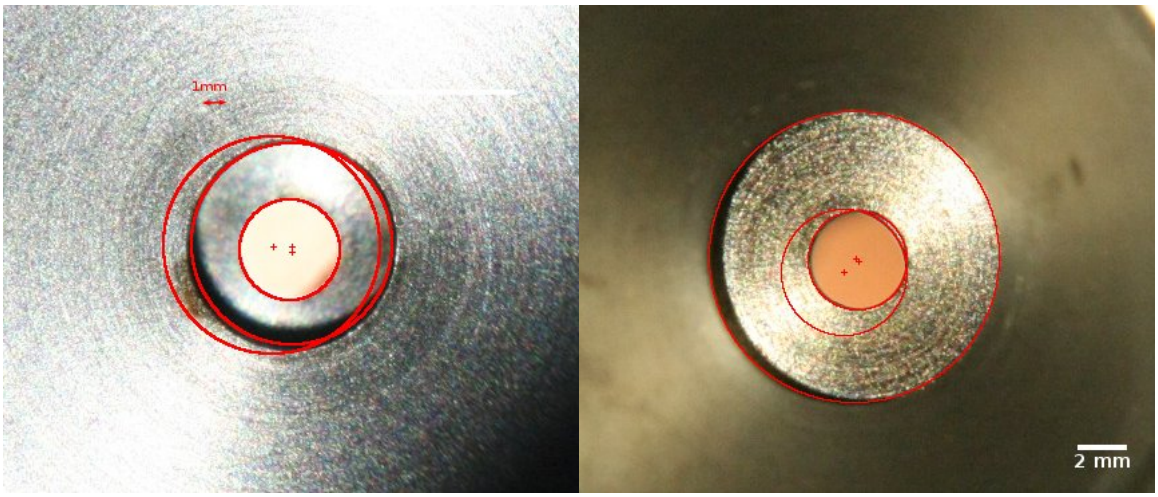

Figure 5.10: Measurement of the misalignment of the injection side (left) and extraction side (right). The three circles show the positions of the apertures in the first, second and plate electrodes on each side.

with the electrode group (first and second electrodes) attached. This allowed an accurate determination of the centres of the apertures and their radial distances from one another, as was shown in Fig. 5.10. This technique is useful only because it has been verified that the position of the electrode group does not change with each new instance of mounting and dismounting - every time the electrodes are bolted to the tank, they take up the same position, to within our accuracy limit. This means that an iterative process can be used in which the RFQCB cylinder is moved, and then the results are checked against the position of the electrode group. This is done several times to achieve the desired accuracy.

The first step in this process is to align the camera so that it is looking straight down the axis of the RFQCB cylinder. This is done by aligning the injection and extraction plate apertures on the RFQCB itself, as demonstrated in Fig. 5.12.

Once the camera was aligned, a picture was taken first of the injection/extraction plate aperture, then of the same spot with the electrode group attached. Since the

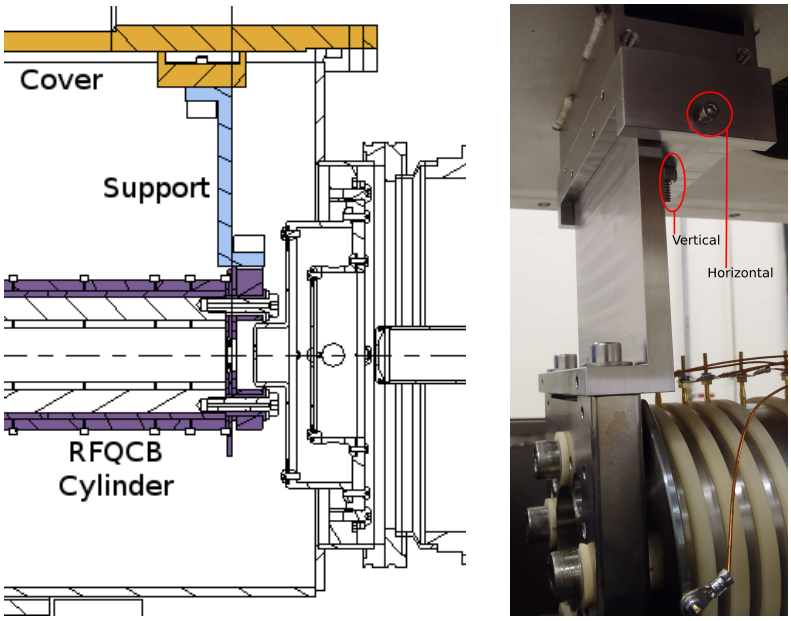

Figure 5.11: The left figure shows the original support system used in ISCOOL and the right figure shows the modified system, with the adaptor piece attached above the support.

camera was not moved or adjusted between these two pictures, they could be directly compared to determine if the centres of the apertures lined up. Once the offset of the plate aperture from the electrode group apertures was determined, the adjustment screws on the supports were used to adjust the RFQCB cylinder (and thus the plate) to match the electrode group, and then another round of photos was taken to determine the outcome. This system of move-and-check was applied until the apertures were aligned on both sides, to within 0.1 mm. It was finally possible to align both sides of the RFQCB cylinder with their respective electrode groups. The injection and extraction sides are shown in Fig. 5.13

Since ISCOOL had to be removed from ISOLDE to perform these operations, it had to be re-aligned to the ISOLDE beam line during re-installation. This was done by passing a RILIS laser through the machine and adjusting the RFQCB support

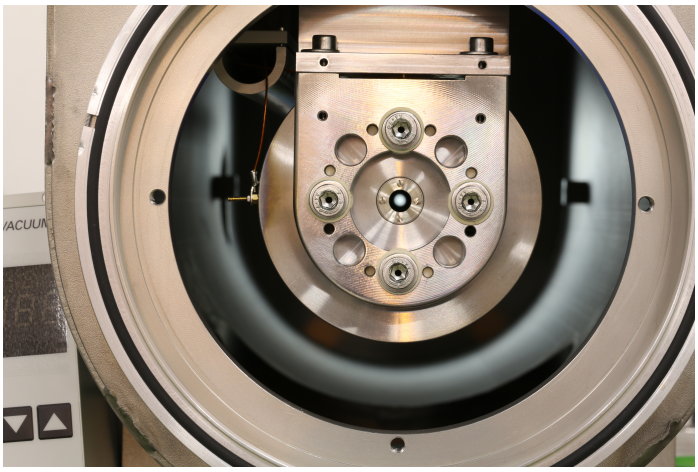

Figure 5.12: A photo showing the injection and extraction apertures aligned. The extraction aperture is the far one, shown by the white circle of light.

such that the laser passed through the centre of the static quadrupole triplets both before and after ISCOOL. An estimation of the accuracy of this process shows errors of approximately 0.256 mm in the vertical direction and 0.47 mm in the horizontal direction.

The results of the re-alignment were immediately apparent in the operation of the machine. Beam steering was reduced to a normal level and 100% transmission was easier to achieve. While this improved significantly the day-to-day operation of the machine, the real improvement in terms of physics was the ability to get lasers into the bunching region of ISCOOL and so facilitate optical pumping experiments.

5.5.2 Proof of Concept with ^{88}Sr

In order to prove that the alignment of ISCOOL was successful and thus the technique of optical pumping was now possible at ISOLDE, preliminary tests were performed with stable strontium. Strontium has a documented property that the ions in a

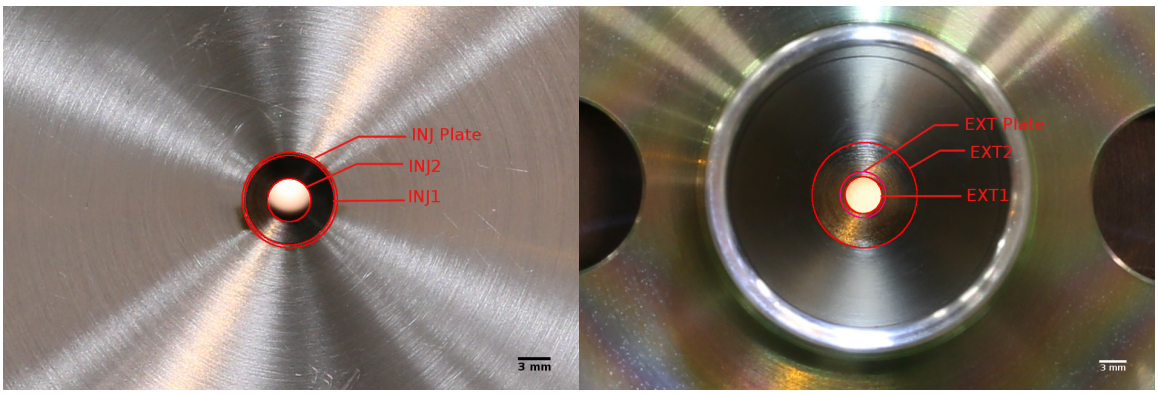

Figure 5.13: The final alignment of the injection side (left) and the extraction side (right), showing red circles around the three apertures.

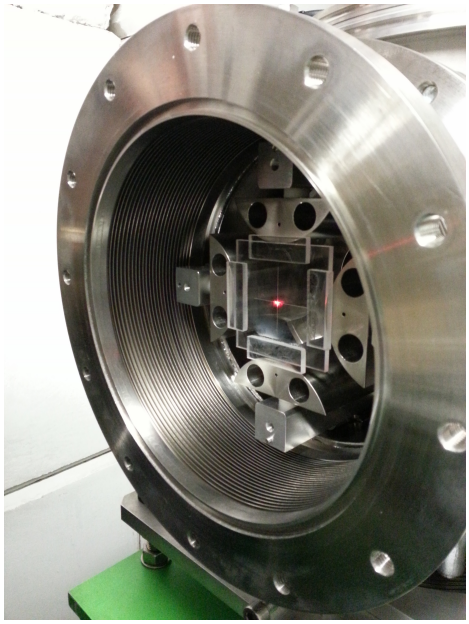

Figure 5.14: The ISCOOL injection quadrupole triplet with a plexiglass target and the laser beam visible, during the alignment process.

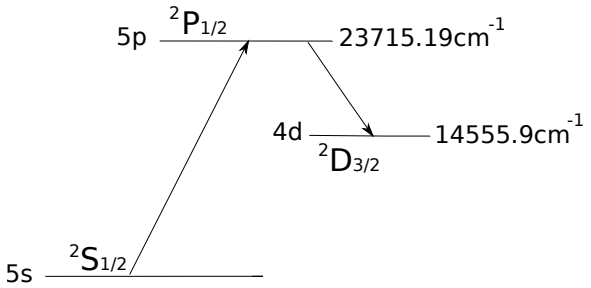

Figure 5.15: Optical pumping scheme for $^{88}Sr^{+}$

metastable state charge exchange more efficiently with sodium vapour in a charge exchange cell than the ground state ions [104]. This property can be used to detect the optical pumping effect without the need for a full laser spectroscopy setup by counting the rate of atoms detected versus the rate of ions detected. If a higher count of atoms is seen with the optical pumping laser on, we can infer that the strontium ions are being optically pumped. The scheme for this requires a laser tuned to 11857.6 cm^{-1}, which produces a two-photon interaction that excites the strontium ions from the 5s $^2S_{1/2}$ ground state to the 5p $^2P_{1/2}$ unstable state, from which they decay to populate the low lying metastable state with configuration 4d $^2D_{3/2}$ [74]. This is shown in Fig. 5.15.

Experimental Setup

This test was carried out using the HRS at 30 kV and the COLLAPS beamline. A beam of ^{88}Sr was produced radiogenically by heating an irradiated target and was ionized with a surface ion source. It was then transported through the two dipole mass separating magnets into ISCOOL, where the beam was cooled, trapped for at least 10 ms (up to 1 s) and released as a bunch. The optical pumping laser was diverted from the RILIS cabin, following the same path to ISCOOL as described in Sec. 5.5

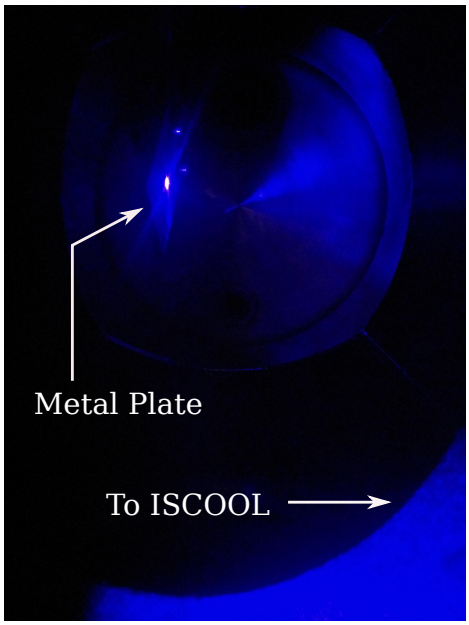

Figure 5.16: Optical pumping laser light hitting a small fluorescing target as seen through a viewport after the cooler/buncher. Photo by Bruce Marsh.

and Fig. 5.8. The blue light can be seen after passage through the cooler/buncher via a viewport in the beamline, as shown in Fig. 5.16.

Once the bunch was extracted from the cooler/buncher, it was transported to the COLLAPS beam line where it passed through the charge exchange cell filled with sodium vapour. The CEC can be floated up to 10 kV, providing the opportunity to vary the final energy of the beam. The charge-neutralized beam then passed a deflector which bent the ions away from the straight beam path while leaving the atoms unaffected. The atoms then impinged on a metal plate from which the secondary electron monitor (SEM) detected the ejected electrons and gave a count of particles. The setup is shown in Fig. 5.17.

The ISOLDE beam gate was used to control the total number of ions in the cooler/buncher and to ensure that the same number of ions entered during each

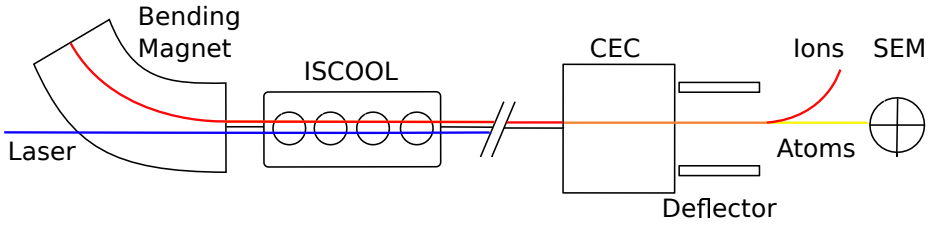

Figure 5.17: Optical pumping setup for ^{88}Sr at COLLAPS.

cycle. Meaurements of ions versus atoms showed that the CEC was neutralizing approximately 35% of the beam.

The deflector after the CEC was switched on and off to compare the total particles coming through the CEC (ions and atoms) to the neutral rate (just atoms, ions deflected). Since the metastable state of Sr^+ has a higher charge exchange cross section compared to the ground state, a higher neutral current was expected when the lasers were used [105].

First Optical Pumping Evidence

Because of the difference in charge exchange properties between ground state and metastable state strontium, the expected indication of successful optical pumping in the cooler was an increased rate of atoms detected at the SEM with the lasers on, in comparison to the rate of atoms detected with the lasers off. Such a signal was quickly observed, however it remained to prove that the signal was indeed due to optical pumping and not an unintended effect of the laser, such as heating. To verify this, a wavelength scan was performed with the laser, and is shown in Fig. 5.18 for data collected over 50 bunches at a final beam energy of 21 keV (the CEC floated on 9 kV with respect to the 30 keV beam energy). The dropoff as the wavelength moves away from the resonant frequency for optical pumping is clearly visible. It was

verified that the flat top of the profile is not due to saturation of the SEM, but is likely due to power broadening.

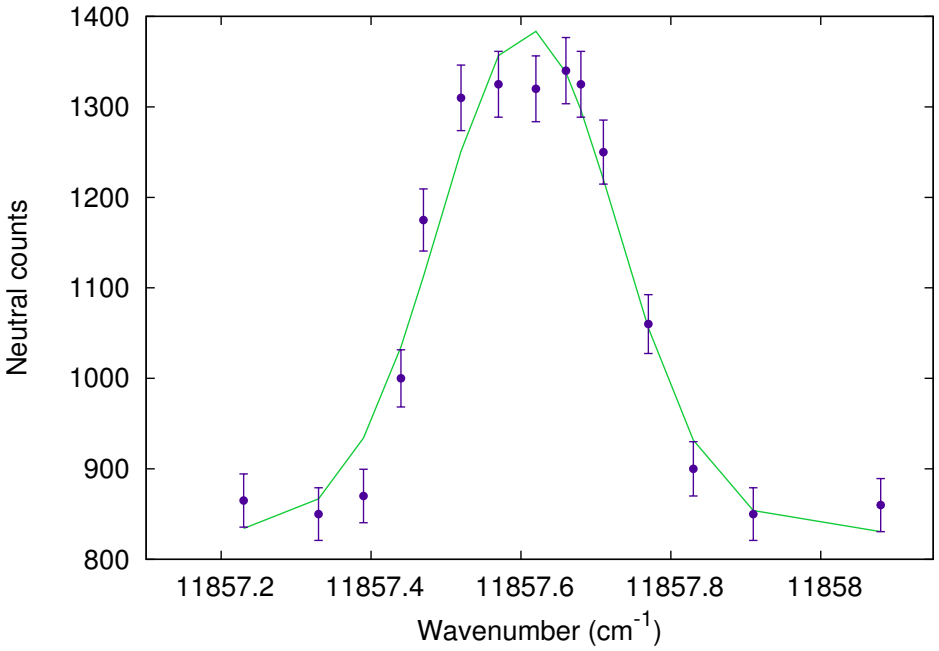

Figure 5.18: Neutral counts as a function of wavenumber.

To determine the saturation levels for this process, a power scan was performed and the results can be seen in Fig. 5.19 for data collected for 1000 bunches at a final beam energy of 21 keV. The nominal laser power used for these tests was 375 mW, however it can be seen that the neutral count rate, that is the number of atoms detected per bunch, is the same for 190 mW and only really begins to fall for laser powers less than 13 mW. Note that the value of the power at 1.3 mW and 0.13 mW was not measured but calculated by the use of two neutral density filters (ND 1 and ND 2). Though this curve seems to imply saturation of the optical pumping effect, it is likely that the saturation is happening on a per pulse basis - all of the ions are interacting with the photons in every pulse but due to the processes of relaxation this

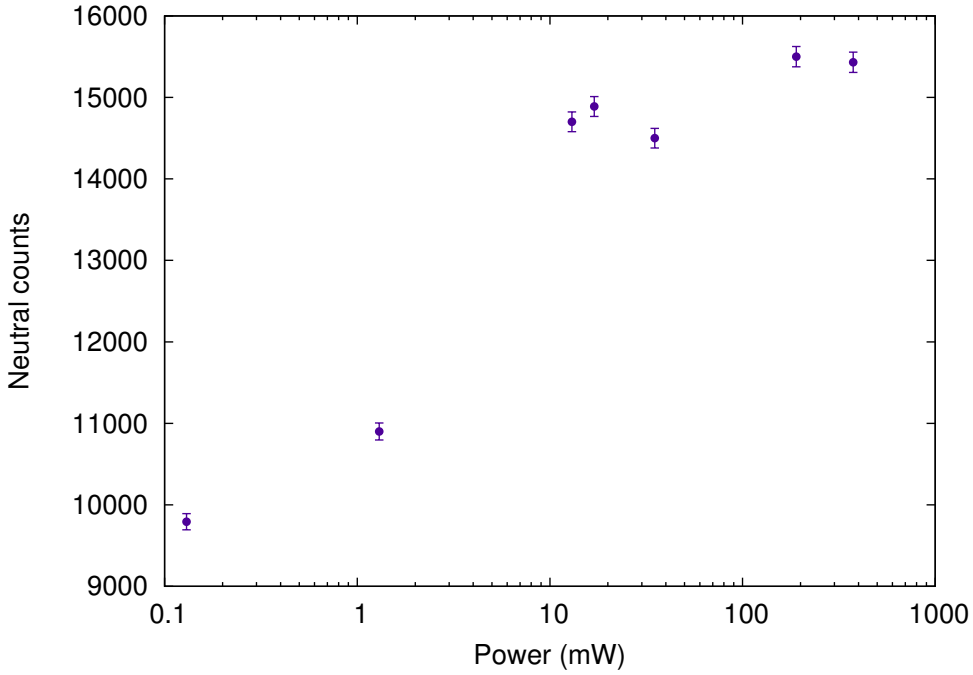

Figure 5.19: Neutral counts as a function of laser power.

does not mean a saturation of the ions into a metastable state. Dedicated tests would be required to determine with certainty the optical pumping efficiency, however an estimation will be made later on.

Finally, Fig. 5.20 shows the ratio of atoms detected with and without the lasers for 1000 bunches with a repetition rate of 10 ms as a function of final beam energy. The trend of higher neutralization cross sections with lower beam energy has been seen in other studies ([105], [104]), however due to the risk of sparks in the charge exchange cell it was not floated above 10 kV, corresponding to a minimum beam energy of 20 keV.

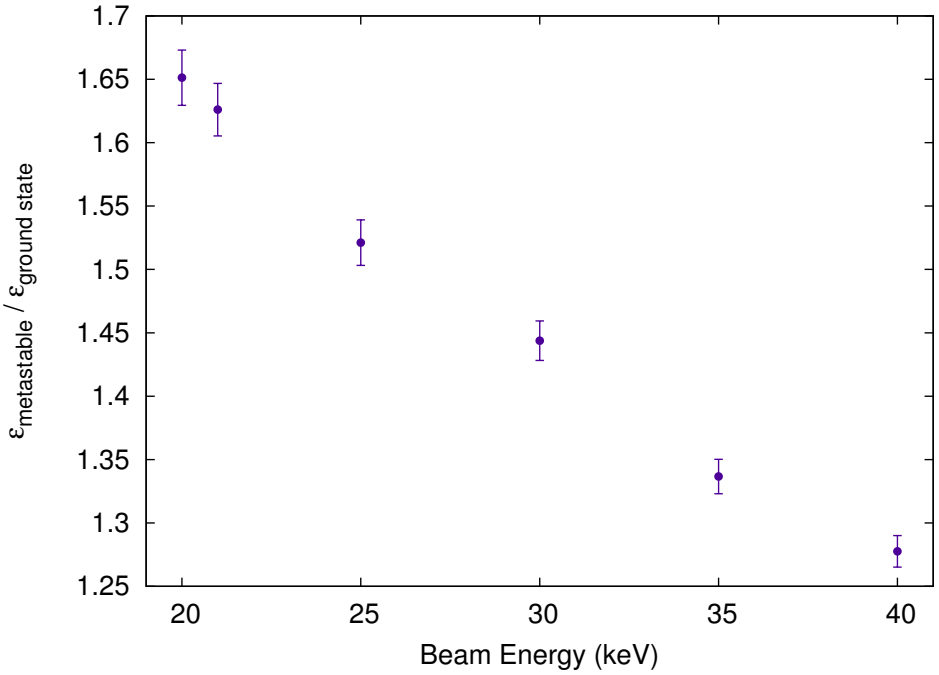

Figure 5.20: Signal to noise ratio for different final beam energies.

ISCOOL Results

In addition to proving that optical pumping in the cooler/buncher at ISOLDE is possible, these tests have provided further information on the performance of ISCOOL under different circumstances. Fig. 5.21 shows the neutral counts with the laser on and neutral counts with the laser off for different cooling times (note the cooling time used in Fig. 5.20 is not shown here). The relative stability of the neutral ions (lasers off) over longer bunching times indicates that ISCOOL is working well and in-trap losses are not affecting the performance of the machine. It also opens the door to experiments that may want to trap ions for long periods of time.

Fig. 5.22 shows the time of flight spectrum for three different cases - a cooling time of 1s with no lasers, a cooling time of 1s with lasers and a cooling time of 10s with

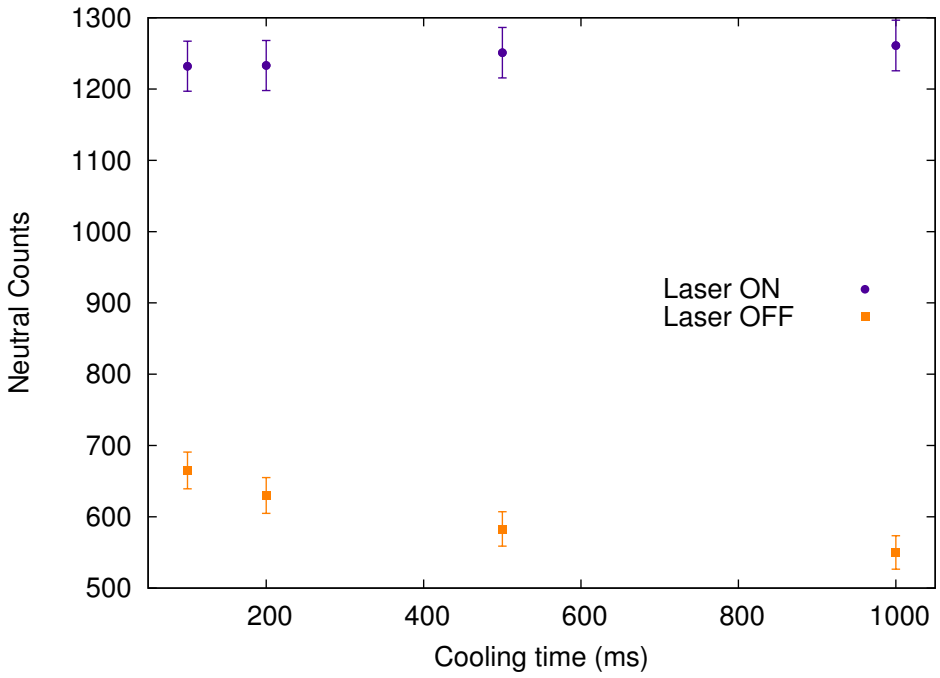

Figure 5.21: The neutral counts detected with the lasers on and those with the lasers off. Population of the $^2D_{3/2}$ state over time increases the number of optically pumped ions.

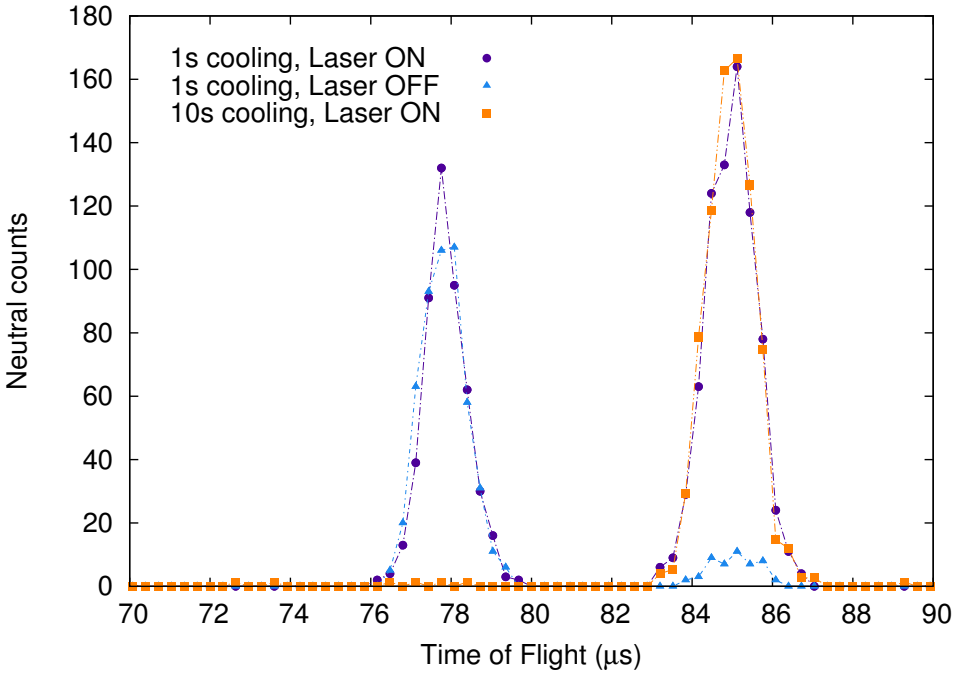

Figure 5.22: Time of flight spectra showing Sr on the left and SrO on the right.

lasers. Here we see molecules forming at the mass of SrO in ISCOOL (see Eq. 3.6 for the approximate relation between mass and time of flight). The comparison between lasers on and lasers off shows that nearly the same amount of Sr is charge exchanged, but a much higher proportion of SrO is charge exchanged with the laser on. Most likely metastable Sr preferentially forms the oxide, resulting in the higher numbers of neutral SrO observed. It is also clear that by 10 s, all the Sr has been converted to SrO. This type of in-cooler chemistry is a subject that needs to be further explored; one can imagine exploiting it for multiple purposes at ISOLDE, but also mitigating it as a loss mechanism in certain situations.

Efficiency Estimates

An estimation of the efficiency of the optical pumping is made difficult by the number of unknowns in this experiment, however with some assumptions an approximate value can be calculated.

The first unknown is the level of contamination in the beam. The target in use had been irradiated for long periods, then left without protons for about 4.5 days before these tests began. The ^{88}Sr seen is all radiogenic, and the only possible contaminants are ^{88}Rb and ^{88}Y. ^{88}Rb has a lifetime of only 17.8 minutes, and so should have decayed by the time of the experiment, however ^{88}Y has a lifetime of 106.6 days. Normally a yield check is performed before experiments to determine the levels of contamination and the yield of the desired species, however due to timing issues it was not possible for this experiment. However, a yield check was done several months later for a follow-up test on a target of the same material and the contribution from ^{88}Y to the beam was found to be negligible. The difference between these two targets is the amount of time since the first irradiation - the target used during the first experiment was an old target which had been used multiple times, and the target on which the yield check was done had only been used for one experimental run. This could contribute to a difference in the ^{88}Y contaminant via the decay chain $^{88}\text{Zr} \rightarrow {}^{88}\text{Y}$ with a half life of 83.45 days, however ^{88}Y also decays to ^{88}Sr in 106.65 days and since Zr cannot be extracted from the target, there is no evidence of its production. Thus is seems reasonable to assume that the contribution of ^{88}Y to the ^{88}Sr beam was negligible during the described experiment.

The second unknown is the charge exchange cross sections of ground state and

metastable strontium since these were not measured directly in this experiment. Calculations and observations of the ratio of the charge exchange cross section for the ground state and metastable state have been reported in [104]. They measured a signal to background ratio (meaning a ratio of charge exchange cross sections $\sigma_{\text{metastable}}/\sigma_{\text{ground state}}$) of approximately 1.5 for a beam of ^{88}Sr at 30 keV. Vermeeren et. al. (1992) performed a later experiment with better optical pumping efficiency and a more sensitive setup, and at 30 keV, they find a neutralization cross section ratio $\sigma_{\text{metastable}}/\sigma_{\text{ground state}} = 2.3$ [105]. Using these measurements we can attempt to estimate the efficiency of the optical pumping in our experiment.

If we assume that there are no contaminants in the beam and that without the optical pumping laser, all the ions are in the ground state (i.e. no collisional or in-source excitation, also an assumption in [105]), then we can use the results from [105] to estimate the optical pumping fraction in our experiment. Vermeeren et. al. (1992) claim 95(5)% optical pumping efficiency and a pure strontium beam in their experiment. Under the above assumptions, we can write the ratio of neutral counts with laser on to neutral counts with laser off as,

$$\frac{N_{\text{laserON}}}{N_{\text{laserOFF}}} = \frac{TB \cdot x \cdot \epsilon_{\text{m}} + TB(1-x)\epsilon_{\text{g}}}{TB \cdot \epsilon_{\text{g}}} \tag{5.6}$$

where $N_{\text{laserON}\,|\,\text{laserOFF}}$ represents the neutral count rate with lasers on or off, TB represents the total amount of beam, x represents the fraction of the beam optically pumped to the metastable state, ϵ_{m} represents the efficiency of charge exchange for metastable ions and ϵ_{g} represents the efficiency of charge exchange for ground state ions. Considering the low neutralization efficiencies in the charge exchange cell, we can say that the ratio of charge exchange efficiencies ($\epsilon_{\text{m}}/\epsilon_{\text{g}}$) is equal to the ratio of charge exchange cross sections ($\sigma_{\text{m}}/\sigma_{\text{g}}$), and using the value of $\sigma_{\text{m}}/\sigma_{\text{g}} = 2.3$ from [105]

and our counts for $N_{\text{laserON}}/N_{\text{laserOFF}}$, the optical pumping fraction can be calculated. Using data from Fig. 5.21, we find that for 100 ms trapping time, $x_{100\text{ms}} = 0.65(11)$ and for 500 ms trapping time, $x_{500\text{ms}} = 0.88(16)$.

Though the calculated optical pumping efficiency is only an approximation, the positive result of the ^{88}Sr experiment proved that in-cooler optical pumping was feasible at ISOLDE, and provided the motivation to continue with the first optical pumping physics case, ionic manganese.

Chapter 6

Ionic Manganese Experiment

The first optical pumping physics case to be carried out at ISOLDE was on ionic manganese, in order to measure the quadrupole moments that were previously unavailable due to the insensitivity of the atomic ground state quadrupole splitting to the quadrupole interaction.

6.1 Experimental Setup

The method for producing radioactive manganese ions at ISOLDE, and extracting them as a beam, has been described in Sec. 4.1. The details of the setup for this second experiment are nearly the same, with some modifications made for the inclusion of optical pumping. The ions were produced using a UC_x target, and were ionized with the resonant laser ion source using the scheme shown in Fig. 4.2. In this case, the yields of Mn ions were much lower than the previous experiment, due to multiple target malfunctions. Though theoretically the enhanced spectroscopic efficiency of the optically pumped transition would have allowed the measurement of more exotic

isotopes, like ^{65}Mn, the low yields made this impossible. Nevertheless, good results were obtained and the nuclei $^{53-63}$Mn were measured in high resolution.

As in the atomic case, the ions were extracted as a beam, this time at 30 keV, and were then collected in ISCOOL, which cooled the ions and trapped the cooled ions in a potential well. While they were trapped in the potential well, the ions were optically pumped and subsequently released in bunches of approximately 4 μs length.

The technique of optical pumping was used on the Mn ions in order to prepare them for efficient spectroscopic study, according to the scheme shown in Fig. 4.11. The ions were excited from the $^7S_3$ ground state to the $^5P_3$ state at 43 370.51 cm^{-1}. From here the ions decayed with an Einstein A coefficient of 1.96×10^8 /s to the $^5S_2$ level at 9472.97 cm^{-1}, from which spectroscopy was performed. The decay from the $^5S_2$ metastable state to the ground state is a forbidden transition, so with increasing laser interaction time, the population of ions available for spectroscopy accumulated [74].

The transition from the ground state to the excited state in the ion is not efficient, however this disadvantage is compensated for by performing the optical pumping in the cooler/buncher. Since the ions remain trapped in the potential well throughout the interaction with the optical pumping laser, multiple laser-ion interactions took place even with moderate laser power. It was also not necessary to use a high-resolution continuous wave laser, where frequency quadrupling is difficult to achieve [106]. A broadband, pulsed laser was used in this case (a frequency quadrupled titanium saphire laser at 230.5 nm) since the broadband laser linewidth is well matched to the Doppler broadened profile of the ions in the trap. In this case, the bunches were accumulated in the potential well of ISCOOL for 200 ms, allowing multiple

interactions with the 10 kHz repetition rate laser.

The metastable ions were then directed to the COLLAPS experimental setup, as shown in Fig. 3.4 and Fig. 3.5, except for the notable removal of the charge-exchange cell for this ionic experiment. The CEC was replaced with an empty length of beam pipe which was floated on an additional 65 V relative to the tuning voltage on the interaction region, in order to prevent the spectroscopy laser from interacting resonantly with the ions before they reached the interaction region.

As before, the ion beam was overlapped with a co-propagating frequency-doubled narrowband dye laser at a Doppler-shifted vacuum wavelength of 294.69 nm providing approximately 1 mW of power, in order to probe the transition from the metastable state, as described above. A series of tuning electrodes modulated the energy of the bunch from its initial 30 keV, thus effectively Doppler shifting the laser frequency seen by the ions over the range of the hyperfine splitting. Four photomultiplier tubes surrounded the interaction region of the setup and detected the emitted fluorescence as the ions decayed back to the metastable state. The background due to dark counts and randomly scattered laser light was reduced by a factor of approximately 10^4 by restricting the data acquisition system to accept photomultiplier counts only during the time that the ion bunch traversed the interaction region [5]. In the case of ^{63}Mn, photons were only accepted within one half life of the proton pulse on target (proton triggering) in order to further suppress the background counts [107].

6.2 Efficiency Measurements

As discussed in Sec. 5.5.2, optical pumping efficiency estimates can be difficult to make. During this experiment, some power scans were taken in order to observe the

resonant photon count rate as a function of optical pumping laser power. Saturation of the optical pumping transition would then be indicated by a constant resonant count rate, even with increased laser power. Fig. 6.1 shows the results of this scan. This data was taken by monitoring the intensity of one peak in the ^{55}Mn hyperfine spectrum relative to the spectrum background as the laser power was modulated using neutral density filters. The maximum power was 19 mW on the laser table, and the data shown is normalized to the count rate at full power. One full power measurement was taken in between each partial power measurement, in order to correct for fluctuations in the ion beam intensity. From this data, the only conclusion to be made is that the transition is not saturated. Higher laser power does indeed produce a higher signal .

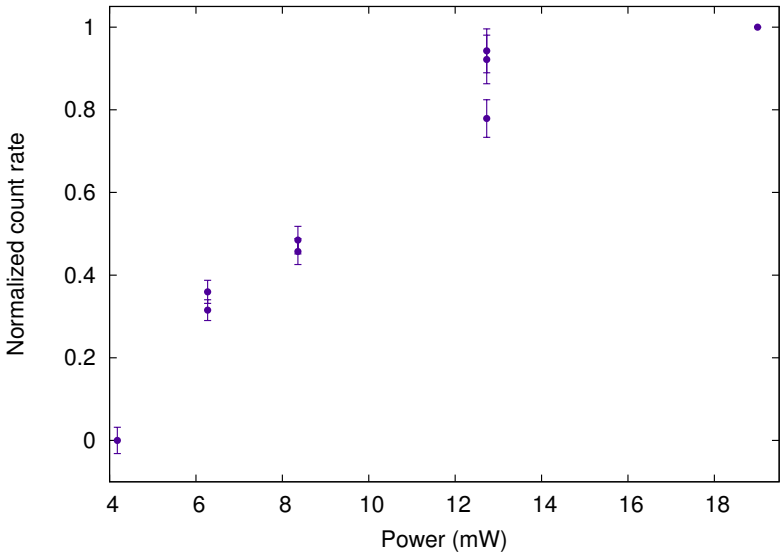

Figure 6.1: Count rates for a single hyperfine peak normalized to the count rate at full power, as a function of optical pumping laser power. Multiple points indicate multiple measurements of the same laser power at different times.

Total experimental efficiencies can be more easily estimated, and used to compare the efficiency for the ionic manganese experiment to the atomic manganese experiment reported in Ch. 4. The measurements of resonant photons-per-ion are based on the ion rate before the RFQCB and the photons are counted over all the peaks in the hyperfine spectrum, to allow for the preferential population of F states during optical pumping, which may skew the individual intensities of the peaks. The efficiency is calculated as,

$$\epsilon = \frac{\text{photons}}{\text{ions}} = \frac{\text{total photons in spectrum} - \text{background counts}}{\text{FC reading} \times \text{bunching time} \times \text{Number of bunches}} \tag{6.1}$$

where FC stands for faraday cup and the number of bunches is equal to the number of scans done for the spectrum. To compare the ionic and atomic experiments, two corrections must be made. The first is to compensate for the different number of photomultiplier tubes used (3 during the atomic experiment, 4 during the ionic). Assuming the efficiency of all the PMTs to be the same, we simply multiply the atomic photon count by 4/3. The second correction is due to the faraday cup readings, which were taken on different faraday cups for the two experiments. To compensate for the difference of current measured on the two faraday cups, a scaling factor has been used. In this way, the efficiencies were approximated as,

$$\epsilon_{\text{atomic}} \approx 1\,\text{photon}/1.2 \times 10^4\,\text{ions} \tag{6.2}$$

$$\epsilon_{\text{ionic}} \approx 1\,\text{photon}/1.2 \times 10^3\,\text{ions}. \tag{6.3}$$

Thus even with a non-optimal optical pumping setup, the ionic experiment shows a higher efficiency. The use of the optical pumping can be seen in Fig. 6.2, in which the resonant signals with and without optical pumping are compared. The dramatic effect of the optical pumping on the population of the metastable state can be seen.

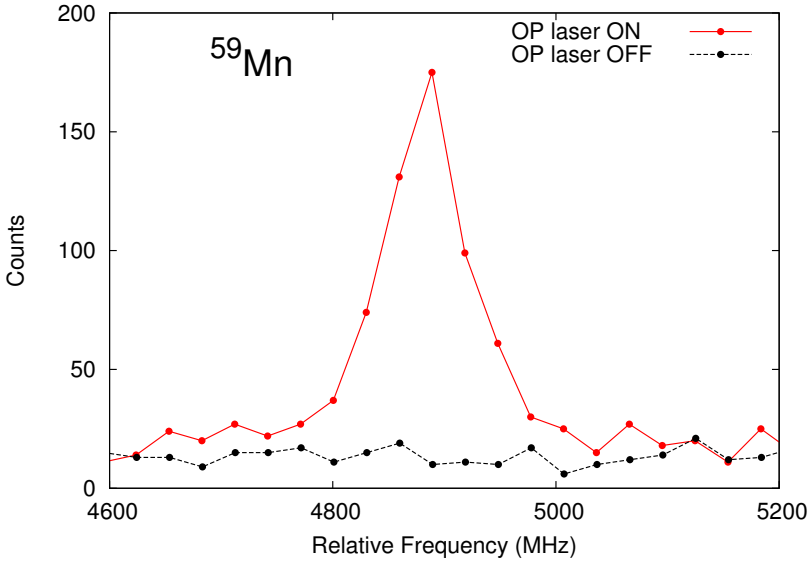

Figure 6.2: Comparison of counts recorded for one hyperfine peak with the optical pumping laser on and off.

6.3 Analysis

The analysis of the ionic spectra proceeded much the same way as for the atomic spectra; the spectra were recorded as a function of voltage, then converted to frequency, and the known centroid of the transition (33 897.54 cm^{-1} for the ionic transition $^5S_2 \rightarrow ^5 P_3$ [74]) was subtracted from each frequency data point. In this case the peaks were fit as Voigt profiles, a convolution of Lorentzian and Gaussian lineshapes [108], using the equation,

$$V(x) = G(x) \otimes L(x) \tag{6.4}$$

$$G(x) = \frac{1}{\sigma\sqrt{2\pi}} exp\left(-\frac{(x-x_c)^2}{2\sigma^2}\right) \tag{6.5}$$

$$L(x) = \frac{1}{\pi}\frac{\Gamma}{(x-x_c)^2+\Gamma^2} \tag{6.6}$$

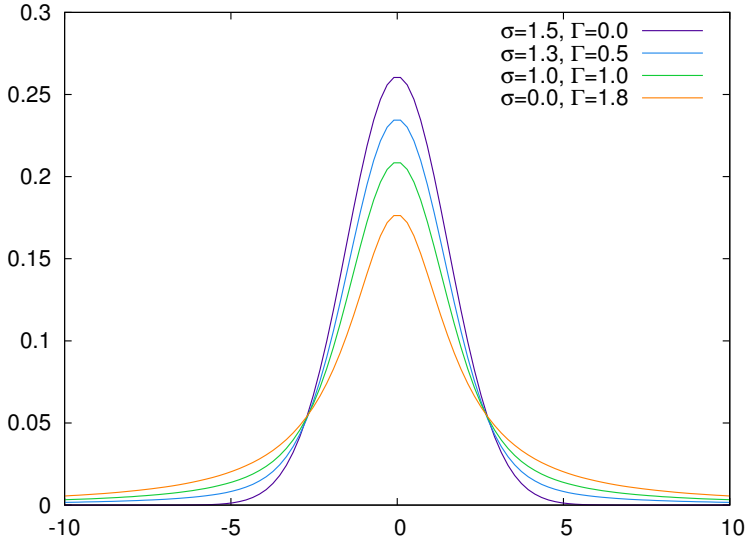

Figure 6.3: Comparison of Lorentzian, Gaussian and Voigt line shapes.

where σ^2 is the variance of the Gaussian distribution, $G(x)$, making the full width at half maximum $\mathrm{FWHM_G} = 2\sigma\sqrt{2\ln 2}$, x_c is the centroid of the lineshape and 2Γ is the full width at half maximum of the Lorentzian distribution, $L(x)$. This convolution can be implemented using the Faddeyeva function ($w(z)$, [109]) as,

$$V(x) = \frac{A\Re[w(z)]}{\sigma\sqrt{2\pi}} \tag{6.7}$$

$$w(z) = \exp^{-z^2}\mathrm{erfc}(-iz) \tag{6.8}$$

$$z = \frac{x - x_c + i\Gamma}{\sigma\sqrt{2}} \tag{6.9}$$

where erfc is the complimentary error function and A is the peak area. Fig. 6.3 shows a comparison of Lorentzian, Gaussian and Voigt lineshapes.

The fit to the spectra was done with a least-squares minimization routine and errors were extracted as shown in Eq. 4.1. All spectra of the same isotope were fitted simultaneously with free intensities and no restrictions on the $A(^5S_2)/A(^5P_3)$ ratio.

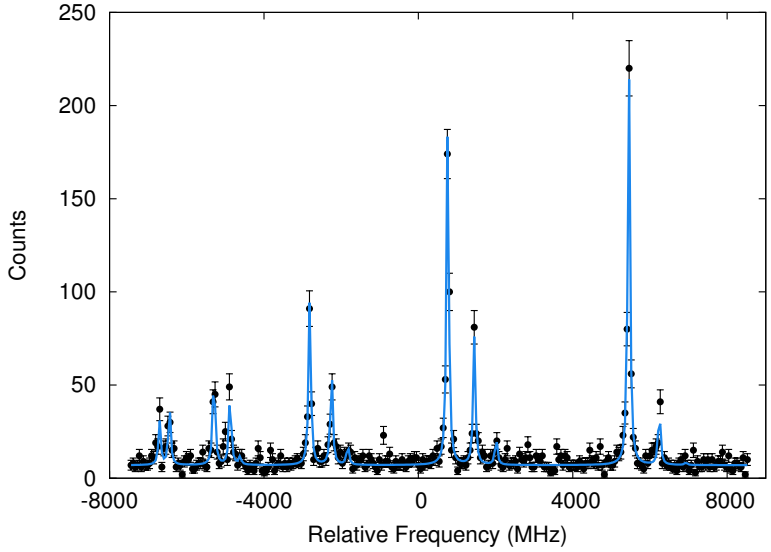

Figure 6.4: Data and fit for one scan of ^{61}Mn.

Fig. 6.4 shows an example fit.

6.4 Results

The extracted hyperfine spectrum A and B coefficients for the $^5P_3$ and $^5S_2$ states are shown in Table 6.1. The A and B coefficients quoted here for ^{55}Mn are in good agreement with the previously measured values of $A(^5P_3) = -150.8(3)$ MHz and $B(^5P_3) = +85(4)$ MHz, obtained in a similar optical pumping experiment for neutron-deficient isotopes [80]. The value of $B(^5S_2)$ was zero within errors for all isotopes, as was found in [80]. The spectroscopic quadrupole moments were extracted using the relation [5],

$$Q = Q_{\text{ref}} \frac{B}{B_{\text{ref}}}$$

where the value of $Q_{\rm ref} = 0.33(1)$ b for ^{55}Mn taken from [110] has been used as the reference. Values for the moments are shown in Table 6.2.

Table 6.1: The hyperfine A and B values of the upper ($^5P_3$) and lower ($^5S_2$) states extracted in this experiment.

Isotope	Spin	$A(^5P_3)$ (MHz)	$B(^5P_3)$ (MHz)	$A(^5S_2)$ (MHz)
^{53}Mn	7/2	−156.2(9)	+16(13)	−1239.4(1)
^{55}Mn	5/2	−150.1(2)	+86(3)	−1195.3(4)
^{57}Mn	5/2	−151.3(5)	+95(6)	−1201.1(7)
^{59}Mn	5/2	−151.2(6)	+90(9)	−1204.9(9)
^{61}Mn	5/2	−153.5(4)	+95(5)	−1218.2(6)
^{63}Mn	5/2	−149.7(6)	+124(7)	−1185.8(9)

6.5 Discussion

In this work, the measured quadrupole moments of neutron-rich mangenese isotopes are compared to the values calculated using two modern shell model effective interactions, as was done for the atomic Mn data, in order to probe the degree of deformation and collectivity in these nuclei. The interactions will again be the GXPF1A effective interaction [2] and the LNPS effective interaction [3]. The GXPF1A interaction assumes a ^{40}Ca core and considers excitations within the entire pf shell for a maximum of 2 protons and 6 neutrons (see Sec. 4.5 for more details). The LNPS calculations use a ^{48}Ca core and consider the entire pf shell for protons, plus neutron excitations within the $p_{3/2}$, $f_{5/2}$, $p_{1/2}$, $g_{9/2}$ and $d_{5/2}$ orbitals. A maximum of 11 excitations across $Z = 28$ and $N = 40$ are allowed, due to the limitations imposed by the required computational power. The results of these calculations are listed in Table 6.2 for the electric quadrupole moment of each isotope. Effective charges of $e_\pi = 1.31$ and

$e_\nu = 0.46$ are used to calculate the quadrupole moments. As mentioned in Ch. 2, effective charges can be used to account for the core polarization effects induced by valence nucleons. As was done for the atomic data (Ch. 4), free g-factors are used in the calculations of the dipole moments, which show good agreement with our previous measurements.

Table 6.2: The magnetic dipole and electric quadrupole moments derived from the A and B coefficients shown in Table 6.1. Also shown are the quadrupole moments calculated using the GXPF1A and LNPS effective interactions. The shell model calculations are done with effective charges $e_\pi = 1.31$ and $e_\nu = 0.46$. The value marked with * indicates the reference value taken from [78] with corrections for diamagnetic shielding. The value marked with the ** indicates the reference value taken from [110]. All GXPF1A calculations have been done by Hanne Heylen (KU Leuven) and all LNPS calculations have been done by Silvia Lenzi (INFN).

Isotope	Spin	$\mu\,(\mu_N)$	Q_s (b)	Q_s (b) [GXPF1A]	Q_s (b) [LNPS]
^{53}Mn	7/2	+5.035(5)	+0.06(5)	+0.08	-
^{55}Mn	5/2	+3.46871790(9)*	+0.33(1)**	+0.32	-
^{57}Mn	5/2	+3.485(2)	+0.37(3)	+0.33	+0.31
^{59}Mn	5/2	+3.496(3)	+0.34(4)	+0.31	+0.32
^{61}Mn	5/2	+3.535(2)	+0.36(3)	+0.30	+0.35
^{63}Mn	5/2	+3.441(3)	+0.48(4)	+0.26	+0.41

Fig. 6.5 shows the experimental quadrupole moments extracted in this experiment compared to theoretical calculations using the GXPF1A and LNPS interactions. The dramatic drop at ^{53}Mn, well reproduced by GXPF1A, can be attributed to the $N = 28$ shell closure. The GXPF1A effective interaction successfully predicts the quadrupole moments up to ^{57}Mn, but at ^{59}Mn ($N = 34$) the predictions and experimental data begin to diverge, with the data instead following the upward trend predicted by LNPS. This is due to the exclusion of the $g_{9/2}$ and $d_{5/2}$ levels from the GXPF1A model space, as seen in the case of atomic Mn, and thus confirms the importance of neutron

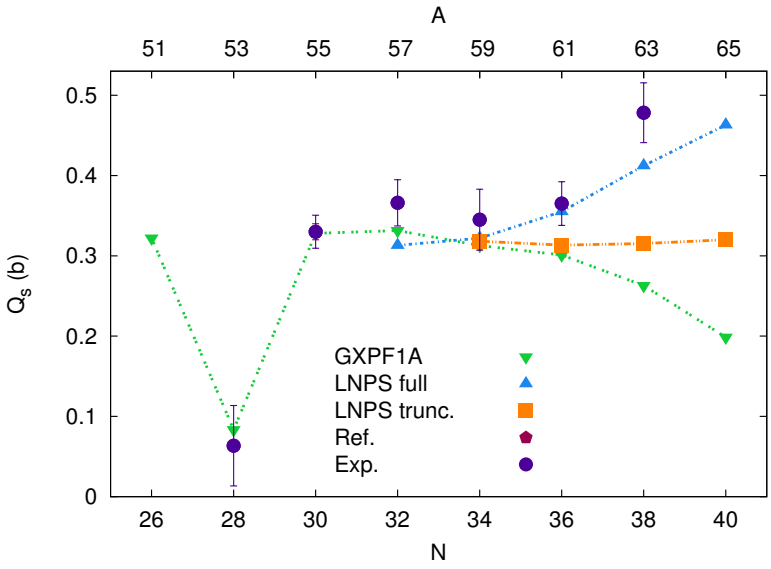

Figure 6.5: Comparison of the quadrupole moments determined in this work to the results of calculations using the GXPF1A and LNPS effective interactions. The results of LNPS calculations with neutron excitations limited to the $\nu\, g_{9/2}$ orbital (excluding excitations to $\nu\, d_{5/2}$) are also shown and are labelled as *trunc.* to differentiate them from the $fpg_{9/2}d_{5/2}$ space calculations, labelled as *full*. The reference point (*Ref.*) is taken from [110].

excitations to these orbitals in describing the wave functions of the neutron-rich Mn isotopes. Indeed, the occupation of the gd orbitals is the signature of collectivity in these nuclei. The increasing trend in deformation cannot be ascribed to the action of the $d_{5/2}$ orbital alone, it is the reciprocal nature of the neutron excitations that are responsible for the effect. Without the $d_{5/2}$ available, correlations are reduced (the $N = 40$ gap is larger, since the tensor force between nucleons is weaker) and there are fewer excitations to the $g_{9/2}$. This, in turn, results in still fewer excitations of neutrons past $N = 40$, and in fewer proton excitations past $Z = 28$.

Also shown in Fig. 6.5 are calculations done with the LNPS effective interaction, limiting the excitation of neutrons to the $g_{9/2}$ orbital, and thus excluding $\nu\, d_{5/2}$ from the model space (labelled *trunc.*). The quadrupole moments calculated in this space

do not reproduce the rising trend of the experimental data, but remain nearly the same from $N = 34$ onwards. This demonstrates the necessity of including both the $\nu g_{9/2}$ and $\nu d_{5/2}$ orbitals in the model space - neutron excitations to $\nu g_{9/2}$ alone are not sufficient to explain the deformation in the Mn isotopes.

Since the exclusion of the $\nu d_{5/2}$ orbital has a marked effect on both neutron and proton excitations, it is helpful to look at the seperate neutron and proton contributions to the total quadrupole moment. This can be done by decomposing it into its components, $Q = Q_\pi + Q_\nu$, the results of which are shown in Fig. 6.6. In the full model space, the neutrons are the dominant contribution to the overall increase in the quadrupole moments, although the protons also induce an increase of $\Delta Q_\mathrm{s} = 0.035\,\mathrm{b}$ between $N = 34$ and $N = 40$. The jump in the experimentally observed quadrupole moments between $N = 36$ and $N = 38$ is due to a combination of the increase in the neutron and proton quadrupole components. The comparison between the $fpg_{9/2}$ and $fpg_{9/2}d_{5/2}$ spaces emphasizes the trends already observed; In the limited $fpg_{9/2}$ model space, both the neutron and proton contributions remain essentially flat, showing no increase in deformation towards $N = 40$ as a result of the limited excitations.

The effects of the exclusion of the $\nu\, d_{5/2}$ orbital can also be seen in the magnetic moments. Fig. 6.7 shows the experimental values of the g-factor extracted from this experiment compared to calculations done with GXPF1A and LNPS (reported in Ch. 4), and the LNPS calculations without the $\nu\, d_{5/2}$ orbital. Here we see that at $N = 34$, the LNPS calculations with and without the $\nu\, d_{5/2}$ orbital coincide, and the overall experimental trend is adequately reproduced by the truncated fpg space LNPS predictions. However, a small deviation from the full $fpgd$ model space calculations (on the order of 2%) can be seen in the g-factors calculated without the

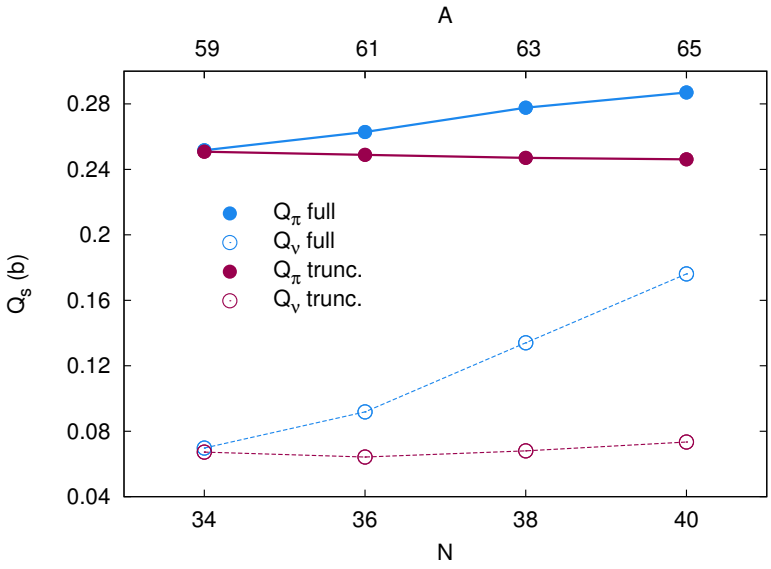

Figure 6.6: Contribution of the neutrons and protons to the total quadrupole moment for both the $fpg_{9/2}$ and $fpg_{9/2}d_{5/2}$ space, where the labels *full* and *trunc.* have been used to indicate the $fpg_{9/2}d_{5/2}$ and $fpg_{9/2}$ spaces respectively.

$\nu\, d_{5/2}$ orbital. This is due to the influence of neutron excitations across $N = 40$ on proton excitations across $Z = 28$, which play an important role in determining the ground state magnetic moments. Without the $\nu d_{5/2}$ orbital available, there are fewer neutron excitations past $N = 40$, widening the $Z = 28$ gap and reducing the proton excitations out of the $f_{7/2}$ orbital. This weakens the strong downward trend that is otherwise observed in the g-factors.

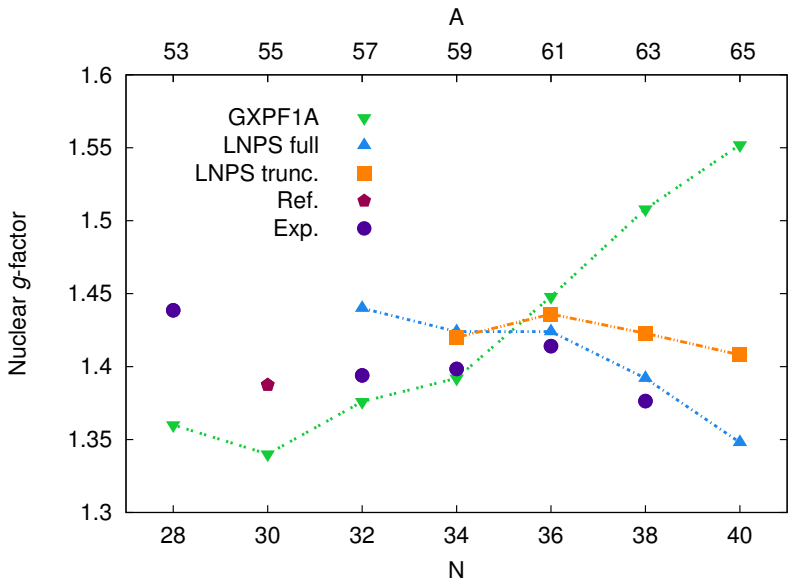

Figure 6.7: Comparison of the magnetic dipole moments determined in this work to the results of calculations using the GXPF1A and LNPS effective interactions. The results of LNPS calculations with neutron excitations limited to the $\nu\, g_{9/2}$ orbital (excluding excitations to $\nu\, d_{5/2}$, labelled *trunc.*) are also shown. The reference point (*Ref.*) is taken from [78] with corrections for diamagnetic shielding.

Chapter 7

Summary

In this work, the results of collinear laser spectroscopy on neutron-rich, odd-even manganese isotopes have been presented in correlation with upgrades to the radio frequency quadrupole cooler and buncher (RFQCB) at ISOLDE, which was necessary to complete these measurements.

Manganese atoms were produced at ISOLDE, CERN and were delivered to the COLLAPS experiment via ISOLDE's RFQCB, ISCOOL. In a first experiment, the electromagnetic moments of the odd-even atomic manganese isotopes $^{51-63}$Mn were probed using the technique of collinear laser spectroscopy. The spectra obtained by this method show the hyperfine structure of the isotopes for the selected transition ($3d^5\,4s^2\,{}^6S_{5/2} \rightarrow 3d^5\,4s4p\,{}^6P_{3/2}$), and allow the extraction of the hyperfine A and B coefficients. The A coefficient was used to determine the magnetic dipole moments of the isotopes, and these were subsequently compared with the predictions of two modern shell model effective interactions, GXPF1A and LNPS. These two interactions differ mainly in the model space they consider; GXPF1A considers only the pf shell for neutrons while LNPS includes two orbitals outside the pf shell, the $g_{9/2}$ and $d_{5/2}$

orbitals. The comparison reveals that, at higher masses, LNPS is a much better fit to the experimental data, pointing to the role of the gd intruder orbitals in the ground state wave function. Orbital occupation numbers also show that LNPS predicts a swift increase in proton excitations past the $Z = 28$ shell closure, indicating that the wave functions in this region of the nuclear chart are governed by the close interplay between proton and neutron excitations. This is the first direct proof that proton and neutron excitations past the shell closures are playing an important role in the ground state wave functions of neutron-rich manganese.

While the hyperfine B parameters were also extracted from the spectra in this experiment, the insensitivity of the ground state transitions to the quadrupole interaction prevented the precise determination of B and thus made the electric quadrupole moment impossible to extract with reasonable precision. In order to measure this quantity, another experiment was proposed using ionic manganese, for which there is a suitable transition with sensitivity to the quadrupole moment. This transition, however, is from a metastable state which has a low natural population. To achieve higher efficiencies, it was necessary to optically pump the ions from the ground state, via the intermediate, unstable $3d^5 4p\,{}^5P_3$ state at $43\,370.510\,\mathrm{cm}^{-1}$, to the metastable $3d^5 4s\,{}^5S_2$ state at $9472.970\,\mathrm{cm}^{-1}$. This process was made more efficient by performing the optical pumping in the bunching region of the radio frequency quadrupole cooler and buncher, where the ions are routinely trapped for tens or hundreds of milliseconds before being released to the COLLAPS experiment. This allowed multiple laser-ion interactions and thus a large portion of the ground state ion bunch was pumped to the metastable state for spectroscopic investigation.

The challenge to this scheme was the difficulty in getting the laser into the correct

position inside the RFQCB, where it could interact with the ion bunch. The laser path to the bunching region must pass through three small apertures necessary for the differential pumping system that keeps the helium buffer gas trapped inside the cylinder of the RFQCB. The alignment of the many apertures in the machine was already known to be inaccurate, therefore this had to be remedied in order to proceed with optical pumping. This was accomplished with a new alignment system and an iterative alignment process, improving the performance of the RFQCB as well as making optical pumping possible at ISOLDE.

The second experiment proceeded with manganese ions in much the same way as the first experiment, with the exception of the use of a frequency-quadrupled titanium sapphire laser at 230.5 nm to excite the optical pumping transition, and the removal of the COLLAPS charge-exchange cell which would normally produce atoms. The transition chosen provided the necessary sensitivity to the quadrupole interaction, and spectroscopic quadrupole moments were measured for the odd-even isotopes in the range $^{53-63}$Mn. They were again compared with the results of calculations done with GXPF1A, which predicts a downwards slope to the quadrupole moments from ^{59}Mn onwards, and LNPS, which predicts an upwards slope. Whereas the quadrupole moments calculated in the atomic experiment did not allow a differentiation between these two different trend predictions, the results of the ionic experiment showed clearly that the rising value of the quadrupole moment from $N = 36$ onwards was well reproduced by LNPS, while the reduced model space of GXPF1A limited its accurate predictions to isotopes with values of $N < 36$. The good agreement between the LNPS values and the measured quadrupole moments confirms the validity of the wave function used in these calculations. It also supports the calculated neutron

excitations past $N = 40$ which result from the increase in proton-neutron interactions in the neutron-rich manganese isotopes, and the crucial role the $\nu d_{5/2}$ orbital plays in collectivity.

The work done here to make optical pumping possible and the upgrades made to ISCOOL suggest many possible future projects, such as a re-design of the RFQCB. This would incorporate changes to the differential pumping system used to contain the helium buffer gas, for instance a segmented design or modified injection and extraction apertures. Easier ways of illuminating the bunching region with lasers might also be included to facilitate in-trap applications such as optical pumping, molecular dissociation and 2+ ionization. Examples such as the use of optical pumping to optimize the selected transition for laser spectroscopy, and the creation of refractory beams by using in-trap dissociation, demonstrate the wide ranging applications of these laser techniques for both physics and technical cases.

Chapter 8

Future Work

ISCOOL is a versatile machine that can be used for a variety of tasks beyond its stated purpose of emittance reduction and bunching, and thus the work presented here has suggested some possible future projects to improve, or make use of, the development of optical pumping at ISOLDE. In parallel to these developments, a new RFQCB has been constructed, to be placed in a test stand in order to assess design upgrades and experimental ideas without jeopardizing ISOLDE. While the new RFQCB has been built (except for the control and RF systems), it has not yet been installed in the test stand. Nevertheless, some of the design modifications discussed below will be in reference to as yet untested upgrades made to the new RFQCB. The lessons learned during the construction of this machine and the hands-on work with ISCOOL will inform the design of the next-generation RFQCB for ISOLDE.

8.1 Use of Lasers in ISCOOL

The physics cases for optical pumping are abundant across the periodic table and applicable specifically to any isotopes for which ground state transitions are inefficient, inaccessible with the available lasers, or insensitive to nuclear properties (for instance isotopes with $J = 0$ ground states, which will not allow a determination of the nuclear spin from the hyperfine spectrum [5]). Optical pumping can also be applied if it is desirable to avoid transitions from the atom, for instance due to the population of a large number of states during charge exchange. The cases of Y [111], Nb [88] and neutron-deficient Mn [80] have already been studied using this technique at Jyväskylä, Finland.

The ability to reliably interact a laser with an ensemble of ions trapped inside the potential well of ISCOOL also opens the door to other experiments and techniques, for example in-cooler 2+ ionization or production of exotic beams. Lasers could be used to dissociate molecules in the cooler and this would allow the production of beams not currently available at ISOLDE. Refractory elements, like Hf, which are not extracted from the target in atomic form, could be extracted as a molecular beam, then broken up in ISCOOL and ejected to produce a beam of ions. If implemented, this technique would be able to produce many new beams for study.

8.2 Upgrades to ISCOOL

Working with ISCOOL has suggested some upgrades which would improve its reliability and functionality. The modifications that did not involve major mechanical changes to the machine have already been implemented (for instance, an upgrade of

the internal wiring, the re-alignment procedure described in Sec. 5.5.1, and modification of the helium injection system), while others require more invasive work and are envisioned for the next-generation RFQCB at ISOLDE.

8.2.1 Laser Entry Upgrades

The challenges associated with laser entry into ISCOOL, described in this work, have suggested a modification that allows lasers to be introduced into the bunching region of the RFQCB using a transverse geometry instead of a collinear one, as shown in Fig. 8.1.

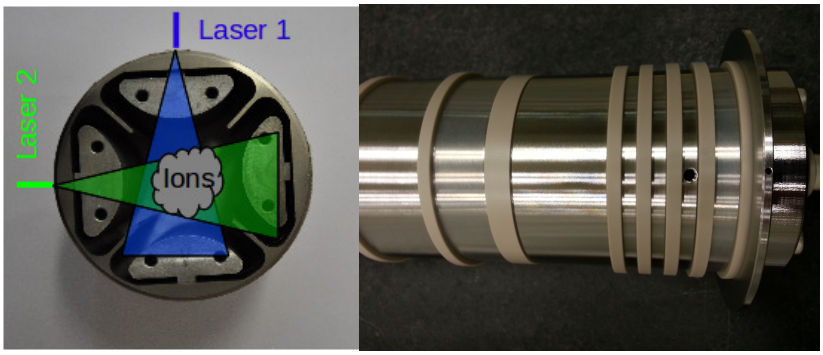

Figure 8.1: Left: Schematic view of transversal laser entry for two lasers into the bunching area of the new RFQCB. Right: Laser entry ports in the axial electrodes (holes continue through the RF electrodes underneath) of the new RFQCB.

This modification has been made to the new RFQCB for the test stand. The laser light will be carried by up to four optical fibres and will couple to the RFQCB cylinder via specially designed adapters. The passage from the exterior through one of the side flanges on the vacuum tank will be accomplished using a Teflon feedthrough as described in [112]. This system will avoid the need to pass the lasers through the various apertures of the magnet and the RFQCB injection system, as well as avoiding the possibility that the line of the laser does not overlap the line of the beam. Based

on an opening angle of 12.7° for the chosen optical fibres, a laser beam should easily be able to encompass the 3-10 mm diameter ion beam at the centre of the cylinder. Thus it should be simple to overlap the entire ion bunch with laser light.

8.2.2 Alignment Upgrades

The alignment upgrade made to ISCOOL allowed the passage of lasers through the machine, enabling optical pumping at ISOLDE, and the alignment system used appears to be quite robust, however the alignment procedure was long and inconvenient. In future generations, the use of a precise system accessible from outside the machine would be a great improvement. For instance, the RFQCB in use at Le Centre de Sciences Nucléaires et de Sciences de la Matière in Orsay [113], a copy of ISCOOL, has been made adjustable by the use of microscrews. This requires a cover designed with openings that allow the controls for the screws to protrude. However, any system that traverses the vacuum tank presents the risk of vacuum leaks. A more direct alignment method would be to redesign the support of the first and second injection/extraction electrodes so that they are not fixed directly onto the vacuum tank. The precision of the shape of the welded tank is much less than the required precision of the position of the electrodes, therefore a system in which all the pieces that must be aligned are fixed together would be preferable.

8.2.3 Vacuum Upgrades

The primary goal of future vacuum upgrades would be to decrease the amount of helium leaking out of the injection and extraction apertures, as discussed briefly in Sec. 5.4. Preliminary simulations have shown the pressure outside the injection and

extraction electrodes to be an order of magnitude higher than the nominal beam line pressure [103], meaning that helium from inside the cylinder is getting trapped in the areas between the injection and extraction electrodes, outside the RF containment field, thus decreasing injection/extraction efficiency and reducing overall beam quality. This effect also limits the internal helium pressure, thus putting a cap on the efficiency of ion cooling. Since the RFQCB works in the molecular or transition pressure regimes [114], attempts to change the pattern of gas flow in the cylinder must rely on the fact that collisions of the helium atoms occur mainly with the surfaces of the machine, and not between the atoms themselves.

This suggests some possible adjustments. One idea would be to thread the apertures on the injection and extraction electrodes or replace them with short tubes in order to increase the surface area associated with the passage of helium atoms out of the machine. Such a modification would increase the probability that a helium atom hits a surface, either sending it back the way it came, or slowing its outward progress. Though calculations of gas flow in these situations rely heavily on the geometry of the machine, we can make some simple estimates. Currently the smallest aperture on either the injection or extraction side is 4 mm in diameter. Assuming the pressure regime to be molecular, the conductance of an aperture is [115],

$$C_{\mathrm{ap}} = A\sqrt{\frac{k_B T}{2\pi m}} \tag{8.1}$$

where A is the cross sectional area of the aperture, k_B is the Boltzmann constant, T is the temperature, and m is the mass of the gas. With helium gas at 20° C and a 4 mm diameter aperture, this gives a conductance of $C_{\mathrm{ap}} = 3.9\,\mathrm{l/s}$. This can be taken as the conductance through this aperture for the current RFQCB. If we instead replace this aperture by a tube of 4 mm diameter and 1 cm length, we can use the

approximation [115],

$$C_{\text{tube}} \approx C_{\text{ap}} \times \frac{4}{3}\frac{d}{l} \tag{8.2}$$

where d is the diameter of the tube and l is the length. This gives $C_{\text{tube}} = 2.1\text{l/s}$. Thus if the ion optics of the injection and extraction systems can be made to accept tubes instead of apertures, the conductance can be reduced by nearly a factor of two. If the tube, or even the aperture, is threaded, this will increase the surface area seen by the gas, and the chances that a helium atom will be deflected are also increased. If we take the previous construction of a 1 cm long tube of 4 mm diameter, the increase in surface area can be obtained from standard M4 thread geometry. The pitch of an M4 fine thread is $P = 0.5\,\text{mm}$, which means that the surface area of the tube will increase by approximately 15%. However, we must also take into account that the diameter of the tube will increase from 4 mm to 4.87 mm in the areas where the threads have been cut out, and this effect will offset some of the gains from the increased surface area. Thus we can average the effects of the larger and smaller diameter in both the calculation of C_{ap} and C_{tube}. This gives the value $C_{\text{tube,thread}} = 1.2\,\text{l/s}$ for the conductance of a threaded tube, which is a 43% improvement over the tube without threads. Of course these calculations are very rudimentary and the use of the conductance formulae for the molecular regime is also only an approximation; at nominal pressure the RFQCB functions in the transition regime, for which analytic calculations are difficult. In any case, these basic calculations show that significant gains can likely be made in this area.

Another solution to this problem that has been used elsewhere (see for example [116]) is the segemented-RFQCB design, in which the cylinder is divided into three parts separated by barriers and the gas is injected into the middle segment, leaving

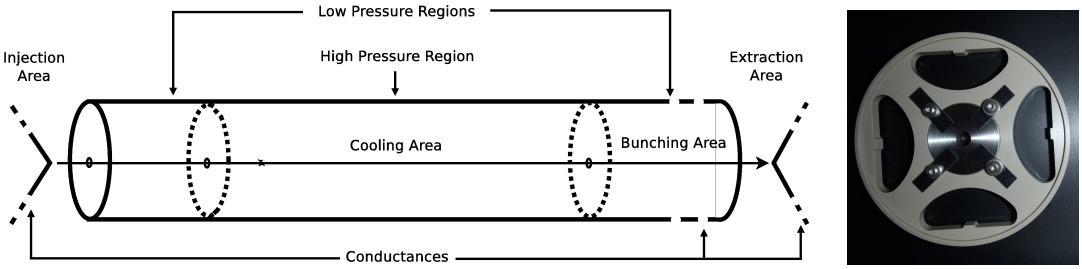

Figure 8.2: Left: Schematic of the RFQCB cylinder with the barriers added in. Right: Design of the barriers - the four hyperbolic shapes are for the RF electrodes to pass.

the two segments near the injection and extraction apertures at a lower pressure and thus reducing the amount of He that leaks out. This system has been implemented for the test stand RFQCB at ISOLDE and Fig. 8.2 shows the layout of the cylinder and the format of the barriers.

We can estimate the reduction in gas flow as a result of the barriers by considering the reduction in cross sectional area. The cross sectional area seen by the helium gas in ISCOOL is the area of one axial electrode, with the area taken up by the four RF rods subtracted. This is shown in Fig. 8.3, where the area filled by the spots is the region in which the gas can move, and is approximately 2080 mm^2.

This is a complicated geometry, but if we approximate this area as a circle, we find $C_{\text{open}} = 647\,\text{l/s}$. Using the design specifications of the barriers, which stipulate a clearance of 0.1 mm around the RF rods, and the sizes of the apertures in the barriers to allow the beam to pass (different for injection and extraction), we can calculate conductances for the barriers. The result is $C_{\text{barrier,INJ}} = 38.5\,\text{l/s}$ for the injection side barrier, and $C_{\text{barrier,EXT}} = 12.1\,\text{l/s}$ for the extraction side barrier, demonstrating that the barriers should have a signifcant effect on gas flow in the cylinder.

While the segmented design may reduce the flow of helium through the exit apertures, it remains to be seen how it will affect the ion trajectories inside the RFQCB.

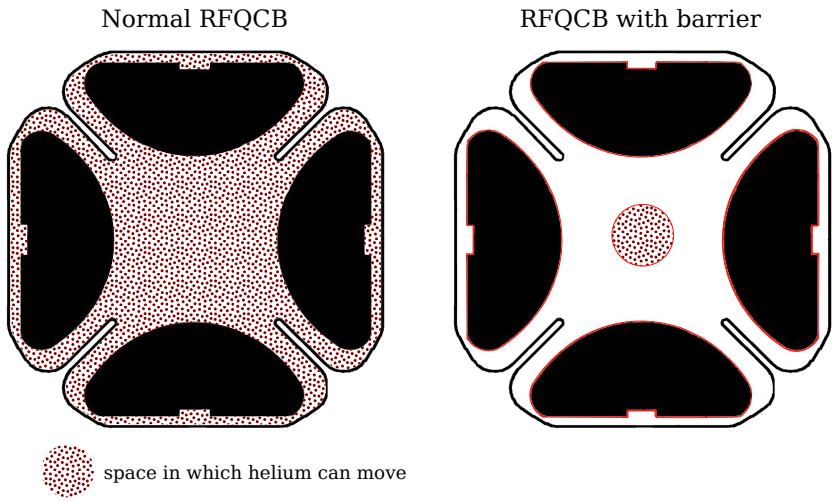

Figure 8.3: Schematic of the area in which helium can flow for the current version of the RFQCB (left) and with the barriers (right).

Simulations have been performed, similar to those discussed in Sec. 5.4, but with three separate pressure regions. The results are shown in Fig. 8.4 for a pressure of 0.1 mbar in the central section and 0.01 mbar in the two end sections.

The most obvious problem with this system is the low pressure near injection when the beam is first entering the cylinder with a large emittance. The advantage gained through a lower pressure outside of the cylinder must be balanced by the disadvantage of low beam cooling near the entrance of the cylinder. Achieving the optimal balance will require experimentation.

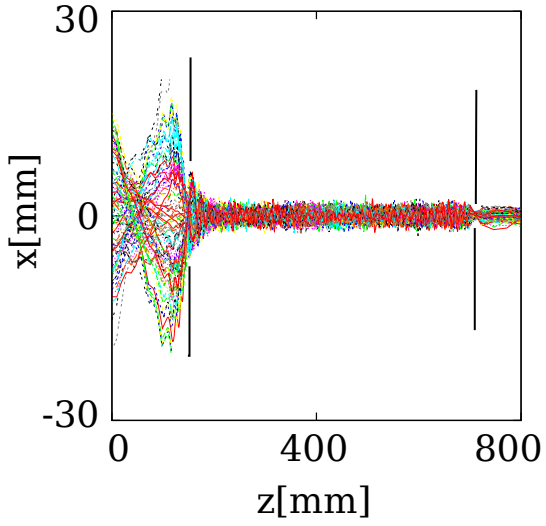

Figure 8.4: Simulation of the ion trajectories in a segmented RFQCB with central pressure 0.1 mbar, and pressure in the injection and extraction segments of 0.01 mbar. The vertical black lines represent the approximate position of the barriers (but are not to scale).

References

[1] M. Honma, T. Otsuka, B. A. Brown, and T. Mizusaki. New effective interaction for pf-shell nuclei and its implications for the stability of the $N = Z = 28$ closed core. *Phys. Rev. C*, 69:034335, Mar 2004.

[2] M. Honma, T. Otsuka, B.A. Brown, and T. Mizusaki. Shell-model description of neutron-rich pf-shell nuclei with a new effective interaction GXPF1. *Eur. Phys. J. A*, 25:499–502, 2005.

[3] S. M. Lenzi, F. Nowacki, A. Poves, and K. Sieja. Island of inversion around ^{64}Cr. *Phys. Rev. C*, 82:054301, Nov 2010.

[4] E. Caurier, G. Martínez-Pinedo, F. Nowacki, A. Poves, and A. P. Zuker. The shell model as a unified view of nuclear structure. *Rev. Mod. Phys.*, 77:427–488, Jun 2005.

[5] B. Cheal and K.T. Flanagan. Progress in laser spectroscopy at radioactive ion beam facilities. *J. Phys. G Nucl. Part. Phys.*, 37(11):113101, 2010.

[6] K. Blaum, J. Dilling, and W. Nörtershäuser. Precision atomic physics techniques for nuclear physics with radioactive beams. *Phys. Scripta*, 2013(T152):014017, 2013.

[7] J. Ljungvall, A. Görgen, A. Obertelli, et al. Onset of collectivity in neutron-rich Fe isotopes: Toward a new island of inversion? *Phys. Rev. C*, 81:061301, Jun 2010.

[8] J. J. Valiente-Dobón, S. M. Lenzi, S. J. Freeman, et al. Spectroscopy of neutron-rich $^{59-63}$Mn isotopes. *Phys. Rev. C*, 78:024302, Aug 2008.

[9] O. Sorlin, S. Leenhardt, C. Donzaud, et al. $^{68}_{28}Ni_{40}$: Magicity versus superfluidity. *Phys. Rev. Lett.*, 88:092501, Feb 2002.

[10] S. Rahaman, J. Hakala, V. -V. Elomaa, et al. Masses of neutron-rich Ni and Cu isotopes and the shell closure at $Z = 28$, $N = 40$. *Eur. Phys. J. A*, 34(1):5–9, 2007.

[11] K. Langanke, J. Terasaki, F. Nowacki, D. J. Dean, and W. Nazarewicz. How magic is the magic ^{68}Ni nucleus? *Phys. Rev. C*, 67:044314, Apr 2003.

[12] H. Grawe and M. Lewitowicz. Shell structure of nuclei far from stability. *Nuc. Phys. A*, 693(12):116 – 132, 2001.

[13] C. Guénaut, G. Audi, D. Beck, et al. High-precision mass measurements of nickel, copper, and gallium isotopes and the purported shell closure at $N = 40$. *Phys. Rev. C*, 75:044303, Apr 2007.

[14] P. Vingerhoets, K. T. Flanagan, M. Avgoulea, et al. Nuclear spins, magnetic moments, and quadrupole moments of Cu isotopes from $N = 28$ to $N = 46$: Probes for core polarization effects. *Phys. Rev. C*, 82:064311, Dec 2010.

[15] B. Cheal, E. Mané, J. Billowes, et al. Nuclear spins and moments of Ga isotopes

reveal sudden structural changes between $N = 40$ and $N = 50$. *Phys. Rev. Lett.*, 104:252502, Jun 2010.

[16] O. Sorlin, C. Donzaud, F. Nowacki, et al. New region of deformation in the neutron-rich $^{60}_{24}Cr_{36}$ and $^{62}_{24}Cr_{38}$. *Eur. Phys. J. A*, 16(1):55–61, 2003.

[17] H. L. Crawford, R. M. Clark, P. Fallon, et al. Quadrupole collectivity in neutron-rich Fe and Cr isotopes. *Phys. Rev. Lett.*, 110:242701, Jun 2013.

[18] R. Ferrer, M. Block, C. Bachelet, et al. Penning trap mass spectrometry of neutron-rich Fe and Co isotopes around $N = 40$ with the LEBIT mass spectrometer. *Phys. Rev. C*, 81:044318, Apr 2010.

[19] S. Naimi, G. Audi, D. Beck, et al. Surveying the $N = 40$ island of inversion with new manganese masses. *Phys. Rev. C*, 86:014325, Jul 2012.

[20] T. Otsuka, T. Suzuki, R. Fujimoto, H. Grawe, and Y. Akaishi. Evolution of nuclear shells due to the tensor force. *Phys. Rev. Lett.*, 95:232502, Nov 2005.

[21] S.B. Patel. *Nuclear Physics: An Introduction*. New Age International, 1991.

[22] C. J. Chiara, I. Stefanescu, N. Hoteling, et al. Influence of the $\nu g_{9/2}$ orbital on level structures of neutron-rich $^{61,62}Mn_{36,37}$. *Phys. Rev. C*, 82:054313, Nov 2010.

[23] N. Aoi, E. Takeshita, H. Suzuki, et al. Development of large deformation in ^{62}Cr. *Phys. Rev. Lett.*, 102:012502, Jan 2009.

[24] A. N. Deacon, S. J. Freeman, R. V. F. Janssens, et al. Yrast structures in the neutron-rich isotopes ^{59,60}Fe and the role of the $g_{9/2}$ orbital. *Phys. Rev. C*, 76:054303, Nov 2007.

[25] S. Zhu, A. N. Deacon, S. J. Freeman, et al. Level structure of the neutron-rich ^{56,58,60}Cr isotopes: Single-particle and collective aspects. *Phys. Rev. C*, 74:064315, Dec 2006.

[26] A.N. Deacon, S.J. Freeman, R.V.F. Janssens, et al. Changes in shape polarisation across the odd neutron-rich Cr isotopes. *Phys. Lett. B*, 622(12):151 – 158, 2005.

[27] E. Caurier, F. Nowacki, and A. Poves. Large-scale shell model calculations for exotic nuclei. *Eur. Phys. J. A*, 15(1-2):145–150, 2002.

[28] W. Rother, A. Dewald, H. Iwasaki, et al. Enhanced quadrupole collectivity at $N = 40$: The case of neutron-rich Fe isotopes. *Phys. Rev. Lett.*, 106:022502, Jan 2011.

[29] M. Hannawald, T. Kautzsch, A. Wöhr, et al. Decay of neutron-rich Mn nuclides and deformation of heavy Fe isotopes. *Phys. Rev. Lett.*, 82:1391–1394, Feb 1999.

[30] M. Sawicka, J.M. Daugas, H. Grawe, et al. Isomeric decay of ^{67}Fe evidence for deformation. *Eur. Phys. J. A*, 16(1):51–54, 2003.

[31] N. Aoi, H. Suzuki, E. Takeshita, et al. Shape transition observed in neutron-rich pf-shell isotopes studied via proton inelastic scattering. *Nuc. Phys. A*, 805(14):400c – 407c, 2008. INPC 2007 Proceedings of the 23rd International Nuclear Physics Conference.

[32] K. Sato, N. Hinohara, K. Yoshida, et al. Shape transition and fluctuations in neutron-rich Cr isotopes around $N = 40$. *Phys. Rev. C*, 86:024316, Aug 2012.

[33] D. Radulov, C. J. Chiara, I. G. Darby, et al. β decay of ^{61}Mn to levels in ^{61}Fe. *Phys. Rev. C*, 88:014307, Jul 2013.

[34] H. Jin, Y. Sun, K. Kaneko, and S. Tazaki. Shell model description with neutron $g_{9/2}$ excitation for neutron-rich $^{57-62}$Mn isotopes. *Phys. Rev. C*, 87:044327, Apr 2013.

[35] T. Baugher, A. Gade, R. V. F. Janssens, et al. Intermediate-energy coulomb excitation of ^{58,60,62}Cr: The onset of collectivity toward $N = 40$. *Phys. Rev. C*, 86:011305, Jul 2012.

[36] F. Recchia, S. M. Lenzi, S. Lunardi, et al. Spectroscopy of odd-mass cobalt isotopes toward the $N = 40$ subshell closure and shell-model description of spherical and deformed states. *Phys. Rev. C*, 85:064305, Jun 2012.

[37] E. Sahin, M. Doncel, K. Sieja, et al. Shell evolution beyond $N = 40$: ^{69,71,73}Cu. *Phys. Rev. C*, 91:034302, Mar 2015.

[38] M. G. Mayer. On closed shells in nuclei. *Phys. Rev.*, 74:235–239, Aug 1948.

[39] K.L.G. Heyde. *The Nuclear Shell Model*. Springer Series in Nuclear and Particle Physics. Springer Berlin Heidelberg, 2012.

[40] M. G. Mayer. On closed shells in nuclei. II. *Phys. Rev.*, 75:1969–1970, Jun 1949.

[41] O. Haxel, J. H. D. Jensen, and H. E. Suess. On the "magic numbers" in nuclear structure. *Phys. Rev.*, 75:1766–1766, Jun 1949.

[42] W.G. Love and G.R. Satchler. Core polarization and the microscopic model of inelastic scattering. *nucA*, 101(2):424 – 448, 1967.

[43] H. O. Funsten, N. R. Roberson, and E. Rost. Inelastic proton scattering from nuclei with 28 neutrons. *Phys. Rev.*, 134:B117–B132, Apr 1964.

[44] P. Ring and P. Schuck. *The Nuclear Many-Body Problem*. Physics and astronomy online library. Springer, 2004.

[45] W.-T. Chou, J.-Y. Zhang, R.F. Casten, and D.S. Brenner. Shell structure in empirical p-n interactions: comparison with Nilsson and shell model calculations. *Phys. Lett. B*, 255(4):487 – 492, 1991.

[46] A. Bohr, B. R. Mottelson, and D. Pines. Possible analogy between the excitation spectra of nuclei and those of the superconducting metallic state. *Phys. Rev.*, 110:936–938, May 1958.

[47] R. Casten. *Nuclear Structure from a Simple Perspective*. Oxford science publications. Oxford University Press, 2000.

[48] K. S. Krane. *Introductory Nuclear Physics*. John Wiley & Sons, New York, 1988.

[49] D. Griffiths. *Introduction to Quantum Mechanics*. Addison-Wesley, 2004.

[50] C.A. Bertulani. *Nuclear Physics in a Nutshell*. Princeton University Press, 2007.

[51] H. Paar. *An Introduction to Advanced Quantum Physics*. Wiley, 2010.

[52] G. Neyens. Nuclear magnetic and quadrupole moments for nuclear structure research on exotic nuclei. *Rep. Prog. Phys.*, 66(4):633, 2003.

[53] H. Miyazawa. Deviations of nuclear magnetic moments from the Schmidt lines. *Prog. Theor. Phys.*, 6(5):801–814, 1951.

[54] C.E. Burkhardt and J.J. Leventhal. *Topics in Atomic Physics*. Springer New York, 2006.

[55] S.J. Davis, J.J. Wright, and L.C. Balling. Hyperfine structure of the ground state of Mn^{55}. *Phys. Rev. A*, 3:1220–1223, Apr 1971.

[56] W.H. King. *Isotope Shifts in Atomic Spectra*. Physics of Atoms and Molecules. Springer US, 1984.

[57] D. Forkel-Wirth and G. Bollen. ISOLDE - a laboratory portrait [special issue]. *Hyperfine Interact.*, 129, 2000.

[58] D. Voulot, F. Wenander, E. Piselli, et al. Radioactive beams at REXISOLDE: Present status and latest developments. *Nucl. Instrum. Meth. B*, 266(1920):4103 – 4107, 2008. Proceedings of the {XVth} International Conference on Electromagnetic Isotope Separators and Techniques Related to their Applications.

[59] R. Catherall, M. Augustin, C. Babcock, et al. An overview of the HIE-ISOLDE design study. *Nucl. Instrum. Meth. B*, 317:204 – 207, 2013. XVIth International Conference on ElectroMagnetic Isotope Separators and Techniques Related to their Applications, December 27, 2012 at Matsue, Japan.

[60] U. Köster. ISOLDE target and ion source chemistry. *Radiochim. Acta*, 89:749, 2009.

[61] M. Brice. Cern-ex-0204023-01, 2002. Online: Accessed August 31, 2015.

[62] T.J. Giles, R. Catherall, V. Fedosseev, et al. The high resolution spectrometer at ISOLDE. *Nucl. Instrum. Meth. B*, 204:497 – 501, 2003. 14th International Conference on Electromagnetic Isotope Separators and Techniques Related to their Applications.

[63] H. Frånberg, P. Delahaye, J. Billowes, et al. Off-line commissioning of the ISOLDE cooler. *Nucl. Instrum. Meth. B*, 266(1920):4502 – 4504, 2008.

[64] S.L. Kaufman. High-resolution laser spectroscopy in fast beams. *Opt. Commun.*, 17(3):309 – 312, 1976.

[65] R. Menzel. *Photonics: Linear and Nonlinear Interactions of Laser Light and Matter*. Advanced texts in physics. Springer Berlin Heidelberg, 2007.

[66] W. Demtröder. *Laser Spectroscopy: Vol. 1: Basic Principles*. Laser Spectroscopy Series. Springer-Verlag, 2008.

[67] J. Papuga, M. L. Bissell, K. Kreim, et al. Shell structure of potassium isotopes deduced from their magnetic moments. *Phys. Rev. C*, 90:034321, Sep 2014.

[68] A. Klose, K. Minamisono, Ch. Geppert, et al. Tests of atomic charge-exchange cells for collinear laser spectroscopy. *Nucl. Instrum. Meth. A*, 678:114 – 121, 2012.

[69] E. Black. An introduction to Pound-Drever-Hall laser frequency stabilization. *Am. J. Phys.*, 69(1):79–87, 2001.

[70] M. Oinonen, Y. Jading, U. Köster, et al. Laser ionization in β decay studies of Zn and Mn nuclei. *Hyperfine Interact.*, 127(1):431–436, 2000.

[71] B.A. Marsh, L.-E. Berg, D.V. Fedorov, et al. The ISOLDE RILIS pump laser upgrade and the LARIS laboratory. *Hyperfine Interact.*, 196(1-3):129–141, 2010.

[72] B. A. Marsh. Resonance ionization laser ion sources for on-line isotope separators. *Rev. Sci. Instrum.*, 85(2), 2014.

[73] G.A. Martin, J.R. Fuhr, and W.L. Wiese. Atomic transition probabilities scandium through manganese. *J. Phys. Chem. Ref. Data, Suppl.; (United States)*, 17:3, Oct 1988.

[74] A. Kramida, Yu. Ralchenko, J. Reader, and NIST ASD Team. NIST Atomic Spectra Database (ver. 5.2), [Online]. Available: `http://physics.nist.gov/asd` [2015, August 8]. National Institute of Standards and Technology, Gaithersburg, MD., 2014.

[75] National nuclear data center. `http://www.nndc.bnl.gov/nudat2/`. information extracted from the NuDat 2 database.

[76] G. Racah. Theory of complex spectra II. *Phys. Rev.*, 62:438–462, Nov 1942.

[77] K. R. Anton, S. L. Kaufman, W. Klempt, et al. Collinear laser spectroscopy on fast atomic beams. *Phys. Rev. Lett.*, 40:642–645, Mar 1978.

[78] O. Lutz and W. Steinkilberg. ^{55}Mn NMR studies in aqueous permanganate solutions. *Z. Naturforsch*, 29a:1467–1470, July 1974.

[79] N.J. Stone. Table of nuclear magnetic dipole and electric quadrupole moments. *Atomic Data and Nuclear Data Tables*, 90(1):75 – 176, 2005.

[80] F.C. Charlwood, J. Billowes, P. Campbell, et al. Ground state properties of manganese isotopes across the N = 28 shell closure. *Phys. Lett. B*, 690(4):346 – 351, 2010.

[81] E. Caurier and F. Nowacki. Present Status of Shell Model Techniques. *Acta Phys. Pol. B*, 30:705, March 1999.

[82] 2014 CODATA Recommended Values, [Online]. Available: http://physics.nist.gov/cuu/Constants [2016, Feb. 14]. Physical Measurement Laboratory of the National Institute of Standards and Technology, Gaithersburg, MD., 2014.

[83] H. Noya, A. Arima, and H. Horie. Nuclear moments and configuration mixing. *Prog. Theor. Phys. Supp.*, 8:33–112, 1958.

[84] Y. Tsunoda, T. Otsuka, N. Shimizu, M. Honma, and Y. Utsuno. Novel shape evolution in exotic Ni isotopes and configuration-dependent shell structure. *Phys. Rev. C*, 89:031301, Mar 2014.

[85] J.R. Comfort, P. Wasielewski, F.B. Malik, and W. Scholz. Properties of ^{55}Mn, ^{56}Mn and ^{57}Fe in the unified rotational model. *Nuc. Phys. A*, 160(2):385 – 408, 1971.

[86] D. Steppenbeck, A. N. Deacon, S. J. Freeman, et al. High-spin structures in the neutron-rich isotopes $^{57-60}$Mn. *Phys. Rev. C*, 81:014305, Jan 2010.

[87] T. E. Cocolios, A. N. Andreyev, B. Bastin, et al. Magnetic dipole moment of ^{57,59}Cu measured by in-gas-cell laser spectroscopy. *Phys. Rev. Lett.*, 103:102501, Aug 2009.

[88] B. Cheal, K. Baczynska, J. Billowes, et al. Laser spectroscopy of niobium fission fragments: First use of optical pumping in an ion beam cooler buncher. *Phys. Rev. Lett.*, 102:222501, Jun 2009.

[89] J. Buon. Beam phase space and emittance. *CERN Accelerator School : 5th general accelerator physics course*, (LAL-RT-90-15-REV.), Feb 1992.

[90] P. H. Dawson. *Quadrupole Mass Spectrometry and its Applications*. Elsevier Scientific Pub. Co., Amsterdam, 1976.

[91] J.R. Taylor. *Classical Mechanics*. University Science Books, 2005.

[92] I. Podadera Aliseda. *New Developments on Preparation of Cooled and Bunched Radioactive Ion Beams at ISOL-Facilities: The ISCOOL Project and the Rotating Wall Cooling*. PhD thesis, Universitat Politécnica de Catalunya, 2006.

[93] T. Kim. *Buffer Gas Cooling of Ions in a Radio Frequency Quadrupole Ion Guide: A study of the cooling process and cooled beam properties*. PhD thesis, McGill University, 1997.

[94] A. Jokinen, M. Lindroos, E. Molin, M. Petersson, and The ISOLDE Collaboration. RFQ-cooler for low-energy radioactive ions at ISOLDE. *Nucl. Instrum. Meth. B*, 204:86–89, 2003.

[95] S.K. Roy. *Thermal Physics and Statistical Mechanics*. Basic physics through problems series. New Age International, 2001.

[96] L.E. Sutton. *Tables of Interatomic Distances and Configuration in Molecules and Ions : Supplement 1956-59*. Special publication. Chemical Society, 1965.

[97] J. C. Slater. Atomic radii in crystals. *J. Chem. Phys.*, 41(10):3199–3204, 1964.

[98] M.D.N. Lunney, F. Buchinger, and R.B. Moore. The temperature of buffer-gas cooled ions in a Paul trap. *J. Mod. Opt.*, 39(2):349–360, 1992.

[99] D. Dahl. SIMION for the personal computer in reflection. *Int. J. Mass Spect.*, 200(13):3 – 25, 2000.

[100] M. Petersson. A monte-carlo method to simulate buffer gas cooling of ions inside a radio frequency quadrupole. Master's thesis, Linköping Institute of Technology, 2002.

[101] W. McDaniel and E.A. Mason. *The mobility and diffusion of ions in gases*. Wiley series in plasma physics. Wiley, 1973.

[102] R. Kersevan and J.-L. Pons. Introduction to MOLFLOW+: new graphical processing unit-based monte carlo code for simulating molecular flows and for calculating angular coefficients in the compute unified device architecture environment. *J. Vac. Sci. Technol. A*, 27(4):1017–1023, 2009.

[103] M. Hermann, G. Vandoni, R. Kersevan, and C. Babcock. Simulations of the HIE-ISOLDE radio frequency quadrupole cooler and buncher vacuum using the monte carlo test particle code MOLFLOW+. *Nucl. Instrum. Meth. B*, 317(0):488 – 491, 2013. XVIth International Conference on ElectroMagnetic Isotope Separators and Techniques Related to their Applications, December 27, 2012 at Matsue, Japan.

[104] R.E. Silverans, P. Lievens, and L. Vermeeren. A sensitive measuring scheme in collinear fast-ion-beam laser spectroscopy: the optical pumping, state-selective neutralization and particle detection sequence. *Nucl. Instrum. Meth. B*, 26:591 – 597, 1987.

[105] L. Vermeeren, P. Lievens, A. Buekenhoudt, and R.E. Silverans. Charge exchange collisions between alkaline-earth ions and alkali atoms. *J. Phys. B*, 25:1009 – 1019, 1992.

[106] D. T. Yordanov, D. L. Balabanski, J. Bieroń, et al. Spins, electromagnetic moments, and isomers of $^{107\text{-}129}$Cd. *Phys. Rev. Lett.*, 110:192501, May 2013.

[107] H. Heylen, C. Babcock, J. Billowes, et al. Spins and magnetic moments of ^{58,60,62,64}Mn ground states and isomers. *Phys. Rev. C*, 92:044311, Oct 2015.

[108] B.H. Armstrong. Spectrum line profiles: The voigt function. *J. Quant. Spectrosc. Radiat. Transfer*, 7(1):61 – 88, 1967.

[109] V.N. Faddeyeva, N.M. Terentev, and V.A. Fok. *Tables of the Probability Integral for Complex Argument*. Pergamon Press, 1961.

[110] J. Dembczyński, W. Ertmer, U. Johann, S. Penselin, and P. Stinner. Laser-RF double-resonance studies of the hyperfine structure of metastable atomic states of ^{55}Mn. *Zeit. Phys. A: Hadrons Nucl.*, 291(3):207–218, 1979.

[111] K. Baczynska, J. Billowes, P. Campbell, et al. Nuclear spin determination of ^{100m}Y by collinear laser spectroscopy of optically pumped ions. *J. Phys. G Nucl. Part. Phys.*, 37(10):105103, 2010.

[112] E.R.I. Abraham and E.A. Cornell. Teflon feedthrough for coupling optical fibers into ultrahigh vacuum systems. *Appl. Opt.*, 37(10):1762–1763, Apr 1998.

[113] D. Lunney, C. Bachelet, C. Guénaut, S. Henry, and M. Sewtz. COLETTE: A linear Paul-trap beam cooler for the on-line mass spectrometer MISTRAL. *Nuc. Phys. A*, 598(2):379 – 387, 2009.

[114] N. Marquardt. Introduction to the principles of vacuum physics. *CERN Accelerator School: Vacuum Technology*, 1999.

[115] M.H. Hablanian. *High-Vacuum Technology: A Practical Guide, Second Edition*. Mechanical Engineering. Taylor & Francis, 1997.

[116] S. Schwarz, G. Bollen, D. Lawton, et al. A second-generation ion beam buncher and cooler. *Nucl. Instrum. Meth. B*, 204:474 – 477, 2003. 14th International Conference on Electromagnetic Isotope Separators and Techniques Related to their Applications.

[117] J. C. Gutiérrez-Vega, R. M. Rodríguez-Dagnino, M. A. Meneses-Nava, and S. Chávez-Cerda. Mathieu functions, a visual approach. *Am. J. Phys.*, 71(3):233–242, 2003.

[118] V.I. Baranov. Analytical approach for description of ion motion in quadrupole mass spectrometer. *J. Am. Soc. Mass Spectrom.*, 14(8):818 – 824, 2003.

Appendix A

The Mathieu Equations and their Solutions

To derive the equations of motion for an ion in the radio frequency quadrupole field, we begin with the definition of the transverse quadrupole potential (in this case, there is no ion confinement on the longitudinal z axis) [90],

$$\Phi = \frac{\Phi_0}{2r_0^2}\left(x^2 - y^2\right) \tag{A.1}$$

where $2r_0$ is the distance between opposite RF rods and Φ_0 is the potential between opposite rods. Using Newton's Second Law,

$$m\ddot{\boldsymbol{r}} = -e\,\nabla\Phi \tag{A.2}$$

where m is the mass and e is the charge, the equations of motion can be written as,

$$\ddot{x} + \frac{e\Phi_0}{mr_0^2}x = 0 \tag{A.3}$$

$$\ddot{y} - \frac{e\Phi_0}{mr_0^2}y = 0. \tag{A.4}$$

Conventionally the potential between rods is written as [90],

$$\Phi_0 = U - V\cos(\omega_{\mathrm{RF}}t) \tag{A.5}$$

because it is possible to layer a DC potential (U) with the oscillating RF potential ($V\cos(\omega_{\mathrm{RF}}t)$) in order to create a mass filter. We will follow this convention in the next few equations, for the sake of completeness, even though for our case there is no DC potential. Using this potential and making the substitution $\xi = \omega_{\mathrm{RF}}t/2$, the equations of motion can be written as,

$$\frac{d^2x}{d\xi^2} + \frac{4e}{mr_0^2\omega_{\mathrm{RF}}^2}\left(U - V\cos(2\xi)\right)x = 0 \tag{A.6}$$

$$\frac{d^2y}{d\xi^2} - \frac{4e}{mr_0^2\omega_{\mathrm{RF}}^2}\left(U - V\cos(2\xi)\right)y = 0 \tag{A.7}$$

and if we make another set of substitutions,

$$a = \frac{4eU}{mr_0^2\omega_{\mathrm{RF}}^2}, \quad q = \frac{2eV}{mr_0^2\omega_{\mathrm{RF}}^2} \tag{A.8}$$

then the equations of motion can be written in the format of the Mathieu equation [117], using u as either x or y and the two Mathieu parameters a and q,

$$\frac{d^2u}{d\xi^2} + \left(a - 2q\cos(2\xi)\right)u = 0. \tag{A.9}$$

The solution to this equation is written as [90],

$$u(\xi) = B_1e^{\mu\xi}\sum_{n=-\infty}^{\infty}C_{2n}e^{2in\xi} + B_2e^{-\mu\xi}\sum_{n=-\infty}^{\infty}C_{2n}e^{-2in\xi} \tag{A.10}$$

where B_1 and B_2 are constants of integration that depend on the initial conditions and C_{2n} and μ are factors that depend only on a and q. This implies that the stability of an ion's trajectory in the RFQCB is independent of the initial conditions and depends only on the machine parameters via a and q. The solutions for stable ion motion have $\mu = i\beta$ where β is real and not an integer. When β is an integer, the solutions to this equation are oscillatory but with increasing amplitude and they

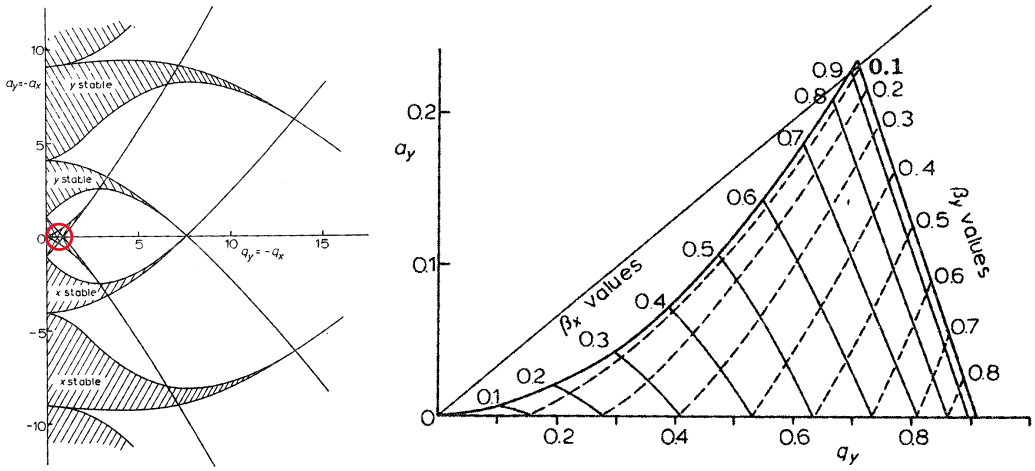

Figure A.1: The Mathieu stability diagrams. The left figure shows the positive portion of the a-q plane (solutions are symmetric around $a = 0$), with the regions of stable solutions for the x direction and y direction motion shown as shaded areas. Reasonable values to achieve for q are low, therefore we take the circled region, where the stable solutions for both x and y overlap. The right figure shows a zoom of this region (for $a, q > 0$ only), with values of β_x and β_y marked. Both figures taken from [90].

define the boundaries between the stable solutions and the unstable solutions. These solutions can be visualized as a stability diagram by plotting a against q, as shown in Fig. A.1.

Plugging $\mu = i\beta$ into Eq. A.10, using the Euler formula and rearranging gives,

$$u(\xi) = (B_1 + B_2) \sum_{n=-\infty}^{\infty} C_{2n} \cos(\xi(2n + \beta)) + i(B_1 - B_2) \sum_{n=-\infty}^{\infty} C_{2n} \sin(\xi(2n + \beta)) \quad \text{(A.11)}$$

and from this it can be seen that the solutions are a superposition of oscillatory

motion with various frequencies following,

$$\omega = \frac{\omega_{\mathrm{RF}}}{2}(2n + \beta). \tag{A.12}$$

By considering realistic experimental conditions, we can simplify these results. First, we can set $a = 0$ since ISCOOL is not a mass filter and the addition of a DC field U is not required. Second, we can assume $q \ll 1$, which is true under normal operating conditions. With these assumptions we can approximate the solutions u as a superposition of two frequencies - the macromotion which corresponds to the fundamental frequency ($n = 0$ in Eq. A.12) and a micromotion which corresponds to the higher order frequencies in Eq. A.12. We can then write the solution as,

$$u = u_{\mathrm{macro}} + u_{\mathrm{micro}}. \tag{A.13}$$

To make use of this simplification, we note that since the micromotion is a small-amplitude, fast oscillation and the macromotion is a large-amplitude, slower oscillation, the approximations,

$$u_{\mathrm{macro}} \gg u_{\mathrm{micro}}, \quad \frac{du_{\mathrm{macro}}}{dt} \ll \frac{du_{\mathrm{micro}}}{dt} \tag{A.14}$$

can be used to write Eq. A.9 (with $a = 0$) as,

$$\frac{d^2u_{\mathrm{micro}}}{d\xi^2} = 2q\, u_{\mathrm{macro}}\, \cos(2\xi). \tag{A.15}$$

Integrating twice this gives,

$$u_{\mathrm{micro}} = -\frac{q}{2}\, u_{\mathrm{macro}}\, \cos(2\xi) \tag{A.16}$$

therefore,

$$u = u_{\mathrm{macro}} - \frac{q}{2}\, u_{\mathrm{macro}}\, \cos(2\xi) \tag{A.17}$$

is the solution to Eq. A.9. The combination of macromotion and micromotion is shown in Fig. A.2.

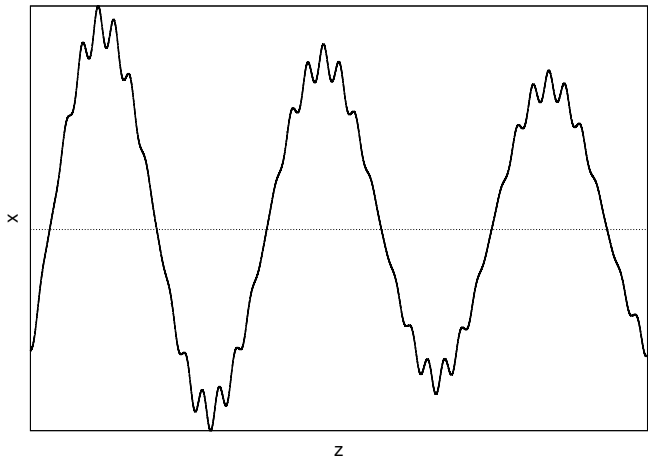

Figure A.2: The motion of one ion in the quadrupole field, showing the contributions of the large amplitude and small amplitude motions to the overall trajectory. Note the total amplitude is decreasing in this case due to interactions with the buffer gas, as explained in Sec. 5.3.3.

Appendix B

Transfer Matrix Method for Ion Motion

The first step in constructing the simulation described in Sec. 5.4 is to define the formalism required to track the motion of ions in the RF field. If we consider a perfect quadrupolar field in which the motions along the x, y and z axes are decoupled, a matrix can be constructed which describes the motion of an ion in one direction through the field of some electrostatic element, for example a dipole field, a quadrupole field, or an area with no field. We can write this as,

$$\begin{bmatrix} x \\ \dot{x} \end{bmatrix} = \boldsymbol{M} \begin{bmatrix} x \\ \dot{x} \end{bmatrix}_0 \tag{B.1}$$

where x is the position of the ion along the x axis, $\dot{x}$ is the angular divergence from the x axis and $\boldsymbol{M}$ is the matrix defining the motion. The subscript indicates the initial values, thus we multiply the initial coordinates by some matrix $\boldsymbol{M}$ to find the final coordinates. The same process can be done for the y direction. The method used here is to model the sinusoidal behaviour of the RF as a series of very short static

quadrupoles of differing strengths, and to follow the motion of an ion through this series of short quadrupoles in order to find its final position after several cycles of the RF. To do this, it must be noted that several electrostatic elements, represented by matrices $\boldsymbol{M_i}$, can be modelled together by multiplying the matrices associated with each one. For instance three quadrupoles in a row can be treated as,

$$\boldsymbol{M}_{\mathbf{Total}} = \boldsymbol{M}_{\mathbf{QP3}} \times \boldsymbol{M}_{\mathbf{QP2}} \times \boldsymbol{M}_{\mathbf{QP1}}. \tag{B.2}$$

Therefore, if we can construct a matrix to represent the effect of a quadrupole of some strength h, we can simulate the effect of a radio frequency quadrupole field by multiplying together a series of these matrices with sinusoidally varying strengths.

The first step in deriving the format of the quadrupole transfer matrix is to write the general equation of motion of an ion in a static quadrupole as [90],

$$\frac{d^2u}{d\xi^2} + h^2u = 0, \tag{B.3}$$

where u is again either x or y, and ξ is defined as before, $\xi = \omega_{\mathrm{RF}}t/2$ with ω_{RF} as the RF frequency. Here, h is a variable that represents the strength of the field. Writing $\dot{u} = du/d\xi$ we can solve this equation by integrating between the phase 0 and some phase θ. We can then write down the solution in terms of a two-by-two matrix as [90],

$$\begin{bmatrix} u \\ \dot{u} \end{bmatrix} = \begin{bmatrix} \cos(h\theta) & \frac{1}{h}\sin(h\theta) \\ -h\,\sin(h\theta) & \cos(h\theta) \end{bmatrix} \begin{bmatrix} u_0 \\ \dot{u}_0 \end{bmatrix}. \tag{B.4}$$

This matrix represents a focussing quadrupole; for a defocussing quadrupole $h^2 < 0$ and the matrix equation becomes,

$$\begin{bmatrix} u \\ \dot{u} \end{bmatrix} = \begin{bmatrix} \cosh(h\theta) & \frac{1}{h}\sinh(h\theta) \\ h\,\sinh(h\theta) & \cosh(h\theta) \end{bmatrix} \begin{bmatrix} u_0 \\ \dot{u}_0 \end{bmatrix}. \tag{B.5}$$

To determine the value of h, we compare Eq. B.3 to the Mathieu equation with $a = 0$,

$$\frac{d^2u}{d\xi^2} - 2q\cos(2(\xi - \xi_0))u = 0 \tag{B.6}$$

where we have written the argument of the cosine in terms of an initial phase, ξ_0. Then,

$$h = \sqrt{\mp 2q\cos(2(\xi - \xi_0))}. \tag{B.7}$$

In order to make analysis simpler, we would like to write this matrix in terms of the Twiss parameters α_{T}, β_{T} and γ_{T} which allow straight-forward calculations in phase space. These parameters were introduced in Sec. 5.1 and Eq. 5.2, and can be related to the solutions of the Mathieu equation. We can write the transfer matrix for a focussing quadrupole derived above (Eq. B.4) as [90],

$$\boldsymbol{M} = \begin{bmatrix} \cos(\pi\beta) + \alpha_{\mathrm{T}}\sin(\pi\beta) & \beta_{\mathrm{T}}\sin(\pi\beta) \\ -\gamma_{\mathrm{T}}\sin(\pi\beta) & \cos(\pi\beta) - \alpha_{\mathrm{T}}\sin(\pi\beta) \end{bmatrix}. \tag{B.8}$$

Here, the unsubscripted β is the same as that encountered in the solution to the Mathieu equation, appearing in the term $e^{i\beta\xi}$ and depending only a and q. There are many approximate ways of calculating β but we can use matrix methods to write it as,

$$\beta = \frac{1}{\pi}\arccos\left(\frac{m_{11} + m_{22}}{2}\right) \tag{B.9}$$

where m_{11} and m_{22} are the elements of the matrix from Eq. B.4. Comparison of the two matrices yields the relationships between the Twiss parameters and the variables

in the equation of motion [118],

$$\beta_{\mathrm{T}} = m_{12}/\sin(\pi\beta) \tag{B.10}$$

$$\gamma_{\mathrm{T}} = -m_{21}/\sin(\pi\beta) \tag{B.11}$$

$$\alpha_{\mathrm{T}} = (m_{11} - \cos(\pi\beta))/\sin(\pi\beta). \tag{B.12}$$

It has been outlined above how the quadrupole field is approximated by very short, static quadrupoles whose effect is represented by matrices that allow the position and velocity of the ion to be calculated at the exit of each of these quadrupoles. The accuracy of this method is determined by the "length" of the static quadrupoles. Practically this is implemented in terms of the RF phase - the simulation determines the strength of the RF field by the position of the phase within one RF period, assigns that strength to a static quadrupole whose length corresponds to a pre-defined step size and then advances the phase by that step size for the next iteration. The step size used here was normally $\pi/200$.

Appendix C

Publications Related to this Work

C. Babcock and T. Giles. Upgrade of the radio frequency quadrupole cooler and buncher for the HIE-ISOLDE project. Nucl. Instrum. Meth. B, 317(0):484 487, 2013. XVIth International Conference on ElectroMagnetic Isotope Separators and Techniques Related to their Applications, December 27, 2012 at Matsue, Japan.

C. Babcock, H. Heylen, J. Billowes, et al. Evidence for increased neutron and proton excitations between $^{51-63}$Mn. Phys. Lett. B, 750:176 - 180, 2015.

H. Heylen, C. Babcock, J. Billowes, et al. Spins and magnetic moments of ^{58,60,62,64}Mn ground states and isomers. Phys. Rev. C, 92:044311, Oct 2015.

C. Babcock, H. Heylen, M. Bissell, et al. Quadrupole Moments in Mn and the Onset of Collectivity towards $N = 40$. In preparation.